Ultrafast Broadband Spectroscopy on Correlated Materials

THÈSE N^O 6671 (2015)

PAR

Andreas Helmut Christian MANN

EPFL

ÉCOLE POLYTECHNIQUE
FÉDÉRALE DE LAUSANNE

Suisse
2015

Abstract

This thesis deals with femtosecond broadband spectroscopy in the visible regime, which is used to study strongly correlated electron systems. The materials that were studied are high-temperature cuprate superconductors of various dopings and the charge-density wave material tantalum disulfide. Central results comprise the coherent excitation and the detection of a charge fluctuation of the superconducting condensate in optimally doped lanthanum strontium cuprate, the quantification of the electron-phonon coupling in lanthanum cuprate, including the description of a method to directly extract matrix elements from the time-resolved experiments, the observation of spectroscopic evidence for paired electrons far above the superconducting transition temperature in neodymium barium cuprate, and a detailed study of coherent phonons associated with the charge ordering in tantalum disulfide.

Key words: femtosecond broadband spectroscopy, correlated electron systems, high-temperature cuprate superconductors, charge density waves

Zusammenfassung

Thema dieser Arbeit ist die Untersuchung stark korrelierter Elektronensysteme mittels Femtosekunden-Breitbandspektroskopie im sichtbaren Spektralbereich. Bei den untersuchten Materialien handelt es sich um Kuprate verschiedener Dotierungen sowie das Ladungsdichtewellenmaterial Tantaldisulfid. Die zentralen Ergebnisse der Arbeit sind die Anregung und Beobachtung einer kohärenten Fluktuation des supraleitenden Kondensates in Lanthan-Strontium-Kupferoxid optimaler Dotierung, die Quantifizierung der Elektron-Phonon-Kopplung in Lanthan-Kupferoxid inklusive der Entwicklung einer Methode zur direkten Bestimmung von Phonon-Matrixelementen anhand der zeitaufgelösten Messungen, der spektroskopische Nachweis gepaarter Elektronen weit oberhalb der kritischen Temperatur in Neodymium-Barium-Kupferoxid und eine umfassende Untersuchung der mit der Ladungsdichtewelle assoziierten kohärenten Phononen in Tantaldisulfid.

Stichwörter: Femtosekunden-Breitbandspektroskopie, korrelierte Elektronensysteme, Kuprat-Hochtemperatursupraleiter, Ladungsdichtewellen

Contents

Contents

List of Figures

1 Introduction

The use of light in the study of nature has a long-standing history. Next to the obvious choice of direct observation through imaging, the concept of optical *spectroscopy*, the study of the interaction of an object with light of a well-defined energy, has become a highly important scientific tool. The term literally describes the possibility to see the "essence" of an object, rather than just observing the object itself. The ability to study materials in a contact-free, non-destructive manner has become an indispensable tool in many fields of modern physics. In solid state physics, the ready availability of femtosecond light pulses made possible by the development of passively mode-locked Ti:sapphire lasers three decades ago [Martinez et al., 1984] has been a major step forward. It is now possible to study coherent and incoherent electronic and bosonic excitations in solids on their inherent timescale, and to disentangle them based on the separation of their relaxation times. The experimental implementation of this is realized in the form of pump-probe experiments, in which a train of intense pump pulses excites a sample, while a second train of much weaker probe pulses that have a well-defined time delay with respect to the pump pulses investigates the changes of the sample. The time interval between two pump pulses is chosen large enough for the sample to relax to its original state, and care is taken that none of its properties are permanently altered by the pulses. A complete time evolution of the sample response is obtained by repeating the experiment at all designated time delays. This measurement technique is conceptually very similar to modern high-speed photography, which overcomes the limitations of mechanical shutter times by keeping the object in a dark environment, and illuminating it in a stroboscopic manner by a short light pulse. Using time-resolved experiments, physicists have learned a great deal about the microscopic processes in complex solid state systems like superconducting or magnetic materials. However, the vast majority of these experiments have been performed using a single laser energy, often simply the 1.55 eV that are produced by the mode-locked Ti:sapphire laser. A logical step forward is the combination of measurements on the ultrafast timescale with

the abundance of information provided by spectroscopy, made possible by the generation of broadband laser pulses spanning a wide range of energies.

An important aspect throughout this thesis is the use of a comprehensive approach to optical experiments. The mentioned broadband experiments, conducted over a probe range in the visible, will be used to study incoherent particle excitations, and to gain access to optical constants and quantities like the transient spectral weight by exploiting the spectroscopic nature of the experiments. Supporting time-resolved experiments by static data, preferably ellipsometry measurements, allows to establish a proper model of the studied system. It will be shown that the possibility to trigger coherent fluctuations can be used as a tool to obtain further information on the physics of a material, by studying its response to the coherent low-energy excitation. This gives access to the resonant behavior of a material, which can be exploited in further experiments, for example in order to achieve transient control of a material. Another interesting option is the possibility to combine the broadband data with higher resolution single-wavelength experiments in an energy region of interest, or to combine reflectivity and magnetic measurements. Altogether, this provides a powerful set of tools to study solid state systems.

The samples studied in this thesis all belong to the class of strongly correlated electron systems. Their physics is governed by the strong interactions of their electrons, leading to a variety of truly fascinating and equally complex phenomena. Prime examples of manifestations of strong correlations are superconductivity, charge ordering, and magnetism. Although all these phenomena have been intensely studied over the past decades, their understanding is mostly limited to very simple models, and even those are often not analytically solvable. Correlated systems therefore seem like a rewarding field of study for the experimental tools provided by ultrafast broadband spectroscopy. The notion of strongly correlated materials is in itself a bit curious, because it implies the existence of materials in which electrons can be described as independent. While there will be no time to expand on this, it should be noted that the reason for this lies in the tremendous success of the description of simpler materials like metals in such a framework of independent electrons. The concept behind this is the description in terms of quasiparticles within the Landau Fermi liquid theory [Landau et al., 1980]. In short, the Pauli principle leads to a scenario that can be described by a renormalization of the materials' carriers in terms of objects that behave as if they were independent particles, named quasiparticles. This concept will be used extensively in the discussion of results on cuprate superconductors that takes up a large part of the thesis.

The thesis is structured as follows: Chapter 2 gives an overview of the theoretical concepts and conventions used throughout the thesis. Chapter 3 provides a detailed explanation of the experiments and their analysis. The experimental results taken on cuprate superconductors and on the charge-ordered tantalum disulfide are presented and discussed in chapters 4 and 5, respectively. Chapter 6 concludes with a summary and some remarks on possible future works.

2 Theoretical Considerations

This chapter provides an overview of the theoretical concepts used throughout this thesis. Some of the topics that are mentioned could fill a whole thesis all by themselves, so the discussion is limited to the core concepts, and references for further reading are given.

2.1 Optical constants

Before going through the various concepts used within this thesis, it is necessary to mention a few definitions. Most of the conventions that are used in the following are taken from the book by Dressel and Grüner [Dressel and Grüner, 2002].

As known from Maxwell's equations, applying an electric field E to a solid causes a displacement (field) D of the form

$$D = \varepsilon \cdot E = (1 + 4\pi\chi) \cdot E = E + 4\pi \cdot P. \tag{2.1}$$

Here, $\varepsilon = \varepsilon_1 + i\varepsilon_2$ is the complex *permittivity*, χ is the (dielectric) *susceptibility*, and P is the *polarization density*. Throughout this thesis, ε is treated as completely interchangeable with the *conductivity* σ known from the microscopic form of Ohm's law,

$$j = \sigma \cdot E,$$

the relation between them being

$$\varepsilon = 1 + \frac{4\pi i}{\omega} \cdot \sigma. \tag{2.2}$$

Optical techniques are immensely powerful in the study of solid state physics, because they allow to determine physical quantities like ε (or σ) of almost any material in a non-invasive manner and with high precision. However, many techniques only measure either the real or imaginary part of ε or σ. Since these functions are analytic, it is possible to obtain their other part via a *Kramers-Kronig* (KK) transformation [Dressel and Grüner, 2002]. It should be noted

that this procedure is only reliable inside the frequency range of the experiment.

Extensive discussions of the bountiful applications of optical spectroscopy to solids exist elsewhere [Grüninger, 1999, Carbone, 2007, Devereaux and Hackl, 2007], so the discussion here will be limited to one concept that will be of importance later on in this thesis, the *spectral weight SW*. This quantity is defined as the integral over the real part $\sigma_1(\omega)$ of the conductivity. When integrating over the whole frequency range, the integral is proportional to the number N of optically excited electrons, divided by their effective mass m^*:

$$SW = \int\limits_0^\infty d\omega' \sigma_1(\omega') = \frac{\pi e^2}{2m^*} \cdot N \equiv \frac{\omega_p^2}{8} \tag{2.3}$$

This integral is called the *f-sum-rule* in optics, and the quantity

$$\omega_p = \sqrt{\frac{4\pi N e^2}{m^*}}$$

is the *plasma frequency*, below which the optical response of a material is dominated by the screening effect of the free electrons, as introduced in Drude theory [Dressel and Grüner, 2002]. Intuitively, if the integral is instead performed over a finite frequency range $[\omega_1, \omega_2]$, the integral is proportional to the effective number N_{eff} of carriers taking part in transitions in the measured frequency interval:

$$SW(\omega_1, \omega_2) = \int\limits_{\omega_1}^{\omega_2} d\omega' \sigma_1(\omega') = \frac{\pi e^2}{2m^*} \cdot N_{\text{eff}} \tag{2.4}$$

Since the latter form matches a typical experimental scenario, where conductivity data is acquired over a limited spectral range, Eq. (2.4) proves very useful in tracking the energy shift of electronic occupancy as a function of experimental parameters, e.g. temperature or pressure. A special application for superconductors is the so-called *Tinkham-Ferrell sum rule* [Ferrell and Glover, 1958], which states that in a superconductor the total value of SW is given by the sum of the contribution of paired electrons at $\omega = 0$ and that of any unpaired electrons,

$$SW = \int\limits_0^\infty d\omega' \left(\sigma_1^{(SC)}(\omega') + \sigma_1^{(n)}(\omega') \right). \tag{2.5}$$

2.2 Time-resolved spectroscopy

Spectroscopy offers a great deal of information, because the electromagnetic nature of light allows interaction with the electronic and magnetic degrees of freedom of a sample. It has found widespread use in research, because it offers a non-invasive tool of analysis that is

applicable to virtually any material whose properties are not permanently altered by the interaction with light. In general, the interaction of light with a sample can be classified according to the power of the electric field strength E present in the interaction. The most common techniques rely on first order, dipole-allowed transitions like simple absorption, or second order effects like Raman processes. Steady-state spectroscopy has been discussed in detail in literature [Cardona and Güntherodt, 1982, Devereaux and Hackl, 2007, Grüninger, 1999, Carbone, 2007], and there is no room here to go into details. Instead, this thesis focuses on ultrafast time-resolved experiments. The main difference between static and time-resolved experiments is that the latter are typically performed in a *pump-probe scheme*, where a light pulse is used to trigger dynamics in the sample under study, whereas a second, weaker pulse is used to probe the sample response after a variable time delay. If the sample returns to its original, unperturbed state between the arrival of two pump pulses, it is possible to repeat the experiment for different time delays and thus reconstruct the sample response as a function of time. The details of this technique are explained in chapter 3.3.

Time-resolved experiments have attracted a lot of interest in solid state physics with the ready availability of sub-picosecond (ps) laser pulses from mode-locked lasers [Martinez et al., 1984]. Current commercial laser systems provide stable sources of ultrafast laser pulses of about 50 femtosecond (fs) duration, which can be further reduced with additional experimental effort. The fs timescale is of significance, because it is the range of typical relaxation times of electrons in solid state samples, allowing for the observation of electronic phenomena. Time-resolved spectroscopic techniques offer several advantages over static spectroscopy, the most important being the possibility to separate physical phenomena occurring on different characteristic time scales, the possibility of coherent excitation, and the availability of phase information. Conceptually, time-resolved spectroscopy is very similar to static techniques. As a rule of thumb, any phenomenon that is observable in static spectroscopy is also accessible in a time-resolved experiment, simply by averaging the data over a large time interval. An example of this is the possibility to compare the Fourier transform of time-resolved reflectivity data to static Raman data, which will be applied extensively in chapters 4 and 5. Conversely, a phenomenon that has a very short life time will often be averaged out in a static experiment. An example for the latter is the observation of short-lived electronic states that are not detectable in static experiments. If the pump excitation of a gapped material occurs below the gap energy, the response is naturally dominated by virtual, second-order interactions like the Raman processes discussed in chapter 2.3. For above-gap excitations, the response comprises first-order and second-order processes, and the interpretation of the signal is more involved. Another important classification of experiments can be done in terms of the *fluence* of the experiment, i.e. the energy per unit area of the pump beam. Generally speaking, there are three regimes available in a pump-probe experiment: For low fluence, the experiment is suitable to study electron-hole dynamics, Cooper pair and quasiparticle formation and relaxation, and the generation of coherent phonons. This is the regime for the experiments presented in this thesis. At higher fluence, anharmonic effects can be studied, or a metastable state can be induced in the material. The control experiments that have recently been discussed

(e.g. [Fausti et al., 2011, Stojchevska et al., 2014]) fall into this category. For very high fluence, the material can be permanently altered, as done in laser ablation or shock compression (e.g. [Acocella et al., 2010]).

An important step to understand the time-separation of physical phenomena mentioned above is the interpretation of electronic excitations in terms of the two-temperature model [Allen, 1987]. It is a simplified, semiclassical model developed to describe the equilibration dynamics in metals in a pump-probe experiment. The electrons and the lattice are treated as independent subsystems that behave like thermodynamic heat reservoirs. The photons of the pump pulse are absorbed by a subset of electrons, which gain a very high kinetic energy. These excited electrons scatter off the other electrons, leading to an internal relaxation of the electronic system. In metals, typical electron-electron scattering times are on the order of $5-50$ fs for excitation energies of $1-2$ eV [Knorren et al., 2000], shorter than or comparable to the duration of the laser pulse, so the process can often be neglected. The parameters described by the model are the electronic temperature T_e after the initial equilibration, and the lattice (i.e. phonon) temperature T_l. The two-temperature-model assumes a simple linear coupling constant γ caused by electron-phonon processes, leading to the rate equation

$$\frac{dT_e}{dt} = -\gamma \cdot (T_e - T_l), \quad \gamma > 0, \tag{2.6}$$

and an equivalent expression for the lattice temperature T_l. From this equation it is evident that the response to a δ-like excitation will follow an exponential decay for the electronic temperature and a rise for the lattice temperature. The coupling constant γ is proportional to the Eliashberg constant $\lambda\langle\omega\rangle$ in superconductivity [Poole Jr et al., 2007, ch. 7]. Similar rate equations can be used for insulating systems if the excitation occurs above the gap. In anisotropic systems it might be necessary to split the lattice system into a subsystem of preferentially coupled phonons and a second system representing the remaining phonons [Mansart et al., 2012]. In magnetic systems, the spins can be treated as a subsystem as well, and the model is applicable to magnetization dynamics experiments [Koopmans, 2003]. While the two- or three-temperature-models are not used within this thesis, they provide a simple argument for the assumption that any observed relaxation dynamics can be fitted with a combination of exponential decays governed by specific time constants. Also, it is important to note that the different time constants of the relaxation dynamics give a temporal order to processes observed in the experiments, and thus a means of separating different effects. As mentioned, electronic processes occur very fast, and are typically completed after 100 fs. The electron-phonon relaxation dynamics are often on the order of few ps [Allen, 1987]. Thermal relaxation by diffusion, on the other hand, occurs with typical time constants of nanoseconds (ns), longer than the time scale considered in this thesis. The experimental dynamics sometimes deviate from the characterization of these basic phenomena due to bottleneck effects or contributions by trapped carriers (cf. e.g. [Koopmans et al., 2010]), in which case the interpretation requires additional input.

2.3 Raman Scattering, ISRS and DECP

Raman scattering is the inelastic scattering of a photon by a crystal lattice or molecule vibration [Cardona and Güntherodt, 1982].[1] Considering the polarization density $P = \chi E$ of the scattering medium, it is a reasonable assumption that the susceptibility χ depends on a number of intrinsic variables ξ. To first order in ξ, χ can be expanded as

$$\chi = \chi_0 + \frac{\partial \chi}{\partial \xi} \xi + \frac{\partial \chi}{\partial \xi^*} \xi^*. \tag{2.7}$$

A simple example for such a variable ξ is the displacement of an ion within the crystal's unit cell, which can be dynamically altered by exciting a coherent phonon. In this case, $\xi(t) = \xi e^{-i\omega_{ph}t}$. The time-dependent polarization response $P(t)$ to an electric field of the form $E(t) = E_0 e^{-i\omega_0 t}$ is given by

$$P(t) = E_0 \cdot \left(\chi_0 e^{-i\omega_0 t} + \frac{\partial \chi}{\partial \xi} \xi e^{-i(\omega_0 + \omega_{ph})t} + \frac{\partial \chi}{\partial \xi^*} \xi^* e^{-i(\omega_0 - \omega_{ph})t} \right). \tag{2.8}$$

Here, the zero-order term describes elastic (Rayleigh) scattering, while the first order terms are for inelastic (Raman) scattering. The exponents $\omega_0 + \omega_{ph}$ and $\omega_0 - \omega_{ph}$ are the Stokes and anti-Stokes contributions, signifying absorption and emission of a photon, respectively. The quantity $\frac{\partial \chi}{\partial \xi}$ is called the *Raman tensor*, and will be of interest for both excitation and detection of the oscillation. Note that in the following discussion contributions of higher order will be neglected. These are relevant to hyper-Raman (third order in E) or wave-mixing experiments.

A special case of Raman scattering is *Impulsive Stimulated Raman Scattering* (ISRS) [Li et al., 2013, Lorenzana et al., 2013, Stevens et al., 2002, Merlin, 1997]. Rewriting the dipole energy of the polarized medium in terms of the induced electrostrictive force $F(t)$, defined via $E_{\text{dip}} = \int P(t)dE \equiv -F(t) \cdot \xi$, the Hamiltonian

$$H = H_{ph} - \frac{1}{2}\chi_0 E^2 - F(t) \cdot \xi \tag{2.9}$$

is obtained, where the phonon term H_{ph} equals $\frac{1}{2}\Pi^2 + \frac{1}{2}\omega_{ph}{}^2\xi^2$, Π being the phonon's momentum. $F(t)$ is thus given by

$$F(t) = \frac{1}{2}E(t)\frac{\partial \chi(\omega_0)}{\partial \xi}E(t), \tag{2.10}$$

meaning that the electric field acts as the driving force of the phonon. The phonon dynamics fulfill the simple equations of motion for a harmonic oscillator,

$$\ddot{\xi} + \omega_{ph}{}^2\xi = F(t), \tag{2.11}$$

---

[1] It will be discussed in chapter 4.2 that scattering off any coherent bosonic excitation can be treated in this formalism.

and the phonon coordinate ξ can be expressed via its Green's function

$$\xi(t) = \int_{-\infty}^{t} F(t) \frac{\sin\left(\omega_{ph} \cdot (t - t')\right)}{\omega_{ph}} dt'.$$

The complete Raman scattering cross section follows from the Golden rule [Cardona and Güntherodt, 1982, Devereaux and Hackl, 2007], and is given by

$$\frac{d\sigma}{d\Omega d\omega} = \frac{(\omega_0 - \omega_{ph})^4 V^2}{(4\pi)^2 c^4} \left| \boldsymbol{e_i} \frac{\partial \chi(\omega_0)}{\partial \xi} \boldsymbol{e_f} \right|^2 \langle \xi^2 \rangle \cdot \delta(\omega - \omega_0), \tag{2.12}$$

where V is the sample volume and the $\boldsymbol{e_i}$ and $\boldsymbol{e_f}$ are the unit vectors indicating the polarization of the incoming and outgoing electric fields. Note that the latter are collinear for the case of ISRS, as can be seen from Eq. (2.10). This implies that using ISRS it is not possible to measure a response containing only the off-diagonal elements of the Raman tensor. Furthermore, the treatment of real materials will necessitate the introduction of damping terms in Eq. (2.11) to account for energy equilibration processes. For a truly impulsive force $F(t) = \delta(t - t_0)$, the resulting coherent phonon dynamics is described by a sine wave, as compared to a displacive (cosine-shaped) excitation for long-lived forces.

The induced oscillation can be observed in time-resolved optical experiments, because due to $\varepsilon = 1 + 4\pi\chi$ (cf. Eq. (2.1)) it modulates the optical properties like

$$\delta\boldsymbol{\varepsilon}(\omega, t) = -4\pi \sum_X \frac{\partial \boldsymbol{\chi}}{\partial \xi}(\omega)\xi(t). \tag{2.13}$$

It can be seen here that the same Raman tensor appears in the generation of the pulse by ISRS as well as the detection process. In practice, ISRS can be triggered for any Raman active excitation that possesses a non-zero matrix element at the excitation energy if the duration of the scattering light pulse is sufficiently short. An extensive discussion of these mechanisms is given in literature [Merlin, 1997, Stevens et al., 2002]. The situation is more complicated in opaque materials, or equivalently when exciting a material above the gap. There, the Raman tensor $\frac{\partial \boldsymbol{\chi}}{\partial \xi}$ has to be replaced in the generation process by a tensor $\frac{\partial \boldsymbol{\pi}}{\partial \xi}$ incorporating the finite-lifetime charge excitation allowed in this case [Riffe and Sabbah, 2007], as well as the virtual excitations already contained in $\frac{\partial \boldsymbol{\chi}}{\partial \xi}$. Note that the latter tensor also becomes sensitive to electronic correlations when the laser frequency is close to the resonance frequency of the phonon. The difference between the two tensors is elaborated in detail in literature [Li et al., 2013].

A third mechanism often discussed in this context is *Displacive Excitation of Coherent Phonons*, or DECP [Zeiger et al., 1992]. Technically, DECP is a non-Raman process in which it is assumed that a coherent phonon is triggered by a population of excited carriers $n(t)$. It is only possible to trigger fully symmetric modes this way, and the generated phonon can often be distinguished from one generated by ISRS in terms of its phase, since it follows a damped cosine function. It

has been argued that the DECP mechanism is actually contained in the two-tensor description of ISRS, which incorporates the effect of $n(t)$ [Garrett et al., 1996]. However, this is not quite correct: A better classification divides the phenomena into Raman processes describable by the ISRS formalism, for which the excitation can be impulsive or displacive, but is always nonlinear in E, and non-Raman processes. The excitation of a coherent phonon due to an out-of-equilibrium carrier population $n(t)$ excited by dipole-allowed transitions that is assumed in the DECP formalism falls into the latter category. In principle, this formalism can also account for impulsive generation of phonons, if $n(t)$ is sufficiently short-lived.

It should be noted that the validity of the description of phonon generation by the ISRS mechanism is well-understood in basic semiconductors [Roeser et al., 2003, Kudryashov et al., 2007]. The general applicability to strongly correlated systems is discussed within the scope of this thesis, as discussed in chapter 4.3. Also, it should be stressed again that the above treatment is valid to first order only, and nonlinear effects like the dependence of the Raman tensor on the excitation strength or the incoherent excitations typically present in pump-probe experiments will introduce subtle differences between the Raman tensors extracted from those experiments when compared to conventional static Raman spectroscopy.

2.4 Superconductivity

The phenomenon of superconductivity is discussed at length in literature, so this chapter serves only as a reminder and reference for the formulas used later on. The "type-I" form of superconductivity was discovered in 1911 [Kamerlingh Onnes, 1911], shortly after it was possible to liquefy Helium for the first time. This early date is remarkable in the light that superconductivity is a purely quantum mechanical effect, and quantum mechanics had yet to be developed in the decades to follow. Type-I superconductivity is characterized by three phenomena:

1. The complete absence of electrical resistivity. Any current generated in an (unperturbed) superconductor will last indefinitely.

2. The *Meissner effect* [Meissner and Ochsenfeld, 1933], or perfect diamagnetism. Any magnetic field is expelled from a superconductor. In return, fields above a critical field strength B_C will destroy the superconducting state.

3. Closely related to the previous point, superconductivity is destroyed as well if the super-conducting current exceeds a critical current density j_C.

Type-II superconductivity differs from this by showing an incomplete Meissner effect. The "conventional" form of superconductivity finds a beautiful explanation in the *Bardeen-Cooper-Schrieffer* (BCS) theory [Bardeen et al., 1957, Poole Jr et al., 2007]: The Fermi electron gas is unstable against the formation of *Cooper pairs* in the presence of any (weak) attractive interaction between the electrons. In conventional BCS systems, this interaction is mediated

by phonons. The Cooper pairs are *bosonic* quasiparticles, and thus are able to establish phase coherence and condense into a macroscopic quantum state, the superconducting condensate.[2] This state is protected against the breaking of a pair by the energy gap Δ. The assumption that the pairing is mediated by phonons was proven by experiments exploiting the isotope effect [Maxwell, 1950, Reynolds et al., 1950], i.e. the specific manipulation of phonon energies upon substitution of an element by one of its isotopes.

The (reduced) BCS Hamiltonian can be written as

$$H_{BCS} = \sum_{k,\sigma} \xi_k n_{\mathbf{k}\sigma} - \sum_k (\Delta c^{\dagger}_{-\mathbf{k}\downarrow} c^{\dagger}_{\mathbf{k}\uparrow} + h.c.), \tag{2.14}$$

where $\xi_k = \epsilon_k - \mu$ is the band energy measured from the Fermi level, Δ is the gap energy, and the operator $c^{\dagger}_{\mathbf{k}\sigma}$ creates an electron with spin σ and wavevector $\mathbf{k}$. The resulting BCS wave function can be written as

$$|\Psi\rangle = \prod_k (u_{\mathbf{k}} + v_{\mathbf{k}} c^{\dagger}_{\mathbf{k}\uparrow} c^{\dagger}_{-\mathbf{k}\downarrow}) |0\rangle, \tag{2.15}$$

where $|0\rangle$ represents the vacuum state. For each pair of states ($\mathbf{k}\uparrow$, $-\mathbf{k}\downarrow$) the wave function is a quantum mixture of the pair being empty (with amplitude $u_{\mathbf{k}}$) and being fully occupied (with amplitude $v_{\mathbf{k}}$). Note that the BCS problem is solved using a Bogoliubov transformation [Bogoliubov et al., 1959]. If a pair is broken, the resulting quasiparticle is a mixture of an electron and a hole, and is called *Bogoliubov quasiparticle.* This term will persistently appear in the discussion of the results on cuprates in chapter 4. It should further be noted that Eq. (2.14) describes a potential with full rotational symmetry, called an *s*-wave potential, whereas the cuprate superconductors discussed in chapter 4 are *d*-wave systems, i.e. the gap symmetry follows that of a *d*-orbital. Cuprate superconductors are type-II superconductors [Poole Jr et al., 2007], and fundamentally different from BCS systems, because they are highly anisotropic layered materials: Conductivity is high in the layers, but strongly reduced for transport across layers. In the superconducting state, Cooper pairs can can travel between layers by Josephson tunneling, and the associated plasma resonance is called the *Josephson plasmon* [Orenstein, 2006]. Coming back to the general BCS case, the theory of superconductivity bears an inherent structural similarity to the description of magnetism, which was exploited by Anderson [Anderson, 1958] to rewrite Eq. (2.14) in terms of so-called *pseudospins*. This analogy will be explained and applied in the discussion of the generation of coherent oscillations of the superconducting condensate in chapter 4.2.
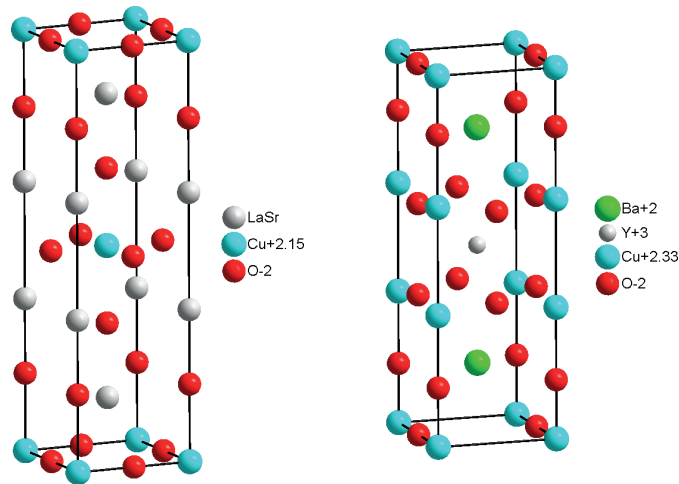
Figure 2.1 – Crystal structure of $La_{2-x}Sr_xCuO_4$ (left) and $YBa_2Cu_3O_{7-\delta}$ (right), being examples of the 214 (perovskite) structure and the 123 structure, respectively. The Cu atom in the Cu-O layer is surrounded by six O atoms in tetragonal configuration in the perovskite structure, while for the 123 compound the unit cell contains two Cu-O layers in which the Cu atom is surrounded by five O atoms in a pyramidal configuration.

2.5 Electronic structure of cuprates

Most of the data presented in this thesis deal with cuprate superconductors. Therefore, it is helpful to have a look at the electronic structure of cuprates in general, which is well studied. A lot about it can be deduced from the crystal structure common to all cuprates. Cuprates are layered, quasi-two-dimensional materials, i.e. they generally show strong anisotropy. The unit cell of all cuprates comprises one or more CuO_2 planes that are fundamental to the physics of the material class. Three prototypical systems are *Lanthanum Strontium Cuprate* ($La_{2-x}Sr_xCuO_4$, or LaSCO), *Yttrium Barium Cuprate* ($YBa_2Cu_3O_{7-\delta}$, or YBCO), and Bismuth Strontium Calcium Cuprate ($Bi_2Sr_2CaCu_2O_{8+\delta}$, or BiSCCO). They are often designated as belonging to the 214-, 123- and 2212-family, respectively, based on the ratio of elements in their empirical formula. Figure 2.1 shows the two structures relevant for this thesis, represented by LaSCO and YBCO. The Cu atom in the Cu-O layer is surrounded by six O atoms in tetragonal configuration in the 214 (perovskite) structure, while for the 123 compound the unit cell contains two Cu-O layers in which the Cu atom is surrounded by five O atoms in a pyramidal configuration. It should be noted that the crystal structures depicted in Fig. 2.1 correspond to the high-temperature phase. At low temperatures, the system undergoes an orthorhombic phase distortion that leads to a difference in lattice parameters *a* and *b* and a tilting of the coordination polyhedron of the in-plane Cu atom, quadrupling the size of the unit cell (see e.g. [Sugai, 1989]).

---

[2] Note that in light of the results discussed in chapter 4.4, the term 'Cooper pairs' is used to denote bosonic quasiparticles comprised of two interacting electrons, even if there is no macroscopic phase coherence between them, and thus, no superconductivity.
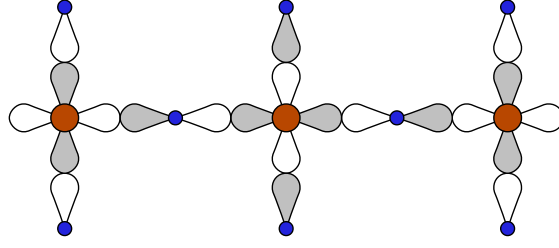
Figure 2.2 – Schematic representation of the relevant orbitals in a Cu-O plane. Shown are the Cu atoms (large, red) with the $3d_{x^2-y^2}$ orbitals, and the O atoms (small, blue) with the $2p_x$ and $2p_y$ orbitals. Shading of the orbitals indicates the phase of their wave function.

The physics of cuprates can be understood in a simplified approach as being caused by the interplay of two effects: the electronic correlations in the Cu-O planes, which are determined by the hybridization of the copper $3d$ orbitals and the oxygen $2p$ orbitals, and the effect of the out-of-plane structure that can vastly influence the properties of the Cu-O planes [Röhler, 1996]. To zeroth order, the effect of the out-of-plane structure can be understood as a doping of the Cu-O plane. Note that the cuprates discussed in this thesis are hole-doped, i.e. the number of carriers in the Cu-O plane is increased by substitution of (highly polarizable) elements in the apical structure and/or an increase of the oxygen content of the sample. The out-of-plane structure of cuprates shows strong electron-phonon coupling to the Cu-O planes [Reedyk and Timusk, 1992], even though phonons do not seem to play a significant role in the emergence of superconductivity in cuprates, as discussed in chapter 4.1. It is also important to note that doped holes preferably occupy the oxygen $2p_{x,y}$ orbitals in the Cu-O layers, as was shown by x-ray absorption spectroscopy [Chen et al., 1992]. The exact effects of doping, however, turn out to be quite complicated. The following overview is limited to the very basic concepts necessary to understand the ongoing discussion of cuprate physics. A good starting point is the electronic structure of the undoped Cu-O plane, illustrated in Fig. 2.2. The relevant orbitals for the bonding of the Cu-O layer are the $3d_{x^2-y^2}$ orbital for copper and the $2p_{x,y}$ orbital for oxygen. The electronic clouds are sketched in between the atoms, and the shading of the orbitals indicates the phase of the wave function. Note that the $3d_{x^2-y^2}$ orbitals experience a strong tetragonal (D_{4h}) crystal field splitting. The electronic character of the Cu-O plane is determined by two energies, the Coulomb repulsion U, which is strongly screened [van den Brink et al., 1995, van den Brink and Sawatzky, 2000], and the transfer integral ("hopping parameter") t_{ij} signifying the energy cost of transferring an electron from site i to site j.

A basic description of the physics arising from the interplay of t and U is given by the *Hubbard model*

$$H = -t \sum_{\substack{<ij> \\ \sigma}} \left(C_{i\sigma}^\dagger C_{j\sigma} + h.c. \right) + U \sum_i n_{i\uparrow} n_{i\downarrow} \tag{2.16}$$

that was proposed to adequately describe the common properties of cuprates [Anderson, 1958]. Here, $C_{i\sigma}^\dagger$ and $C_{j\sigma}$ are the creation and annihilation operators for a hole. The first

term describes the energy gain by electron hopping; the sum $< i j >$ runs over pairs of nearest neighbors only. Notice that this term favors the antiferromagnetic order seen in the cuprate parent compounds: The energy gain is largest if every electron's nearest neighbors all have the opposite spin, which allows the electron to hop to their site. The Coulomb repulsion embodied by the second term instead favors single occupancy. Note that U has a strictly local (on-site) character, assuming strong screening as proposed by Mott [Mott, 1968]. A common approximation of the Hubbard model is the t-J *model* [Spalek, 2007]. In the limit of strong coupling, $U \gg t$, the expansion of the Hubbard model regarding only nearest-neighbor interaction yields

$$H = -t \sum_{\substack{<ij> \\ \sigma}} \left(B_{i\sigma}^{\dagger} B_{j\sigma} + h.c. \right) + J \sum_{<ij>} \left(S_i \cdot S_j - \frac{n_i n_j}{4} \right). \tag{2.17}$$

Here, the operator $B_{i\sigma}^{(\dagger)} = C_{i\sigma}^{(\dagger)}(1 - n_{i\sigma})$ projects out the doubly-occupied sites that are excluded in the model, and $S_i = C_{i\alpha}^{\dagger} \sigma_{\alpha\beta} C_{i\beta}$ is the spin operator defined using the Pauli matrix $\sigma_{\alpha\beta}$. The strength of the *exchange coupling* J is given by $J = 4t^2/U$. A more detailed treatment of the exchange coupling leads to the *Goodenough-Kanamori-Anderson* rules (see e.g. [Zaanen and Sawatzky, 1987]).

The real situation in cuprates is described much more accurately by the *three-band Hubbard model* [Emery, 1987]. It takes into account the strong hybridization between the Cu $d_{x^2-y^2}$ and O $2p_{x,y}$ orbitals that are depicted in Fig. 2.2. The full model reads

$$\begin{aligned} H = & \varepsilon_d \sum_{i,\sigma} n_{i,\sigma}^d + \varepsilon_p \sum_{j,\sigma} n_{i,\sigma}^p + \sum_{\substack{<ij> \\ \sigma}} t_{ij}^{pd} \left(D_{i\sigma}^{\dagger} P_{j\sigma} + h.c. \right) + \sum_{\substack{<jj'> \\ \sigma}} t_{jj'}^{pp} \left(P_{j\sigma}^{\dagger} P_{j'\sigma} + h.c. \right) \\ & + U_d \sum_i n_{i\uparrow}^d n_{i\downarrow}^d + U_p \sum_j n_{j\uparrow}^p n_{j\downarrow}^p + U_{pd} \sum_{\substack{<ij> \\ \sigma,\sigma'}} n_{i\sigma}^d n_{j\sigma'}^p. \end{aligned} \tag{2.18}$$

Structurally, the model is very similar to the Hubbard model from Eq. (2.16): The operators $D_{i\sigma}^{(\dagger)}$ and $P_{j\sigma}^{(\dagger)}$ annihilate (create) holes in the copper $3d$ and oxygen $2p$ orbitals and the hopping parameter t takes on different values for hopping from p to d sites and p to p sites. Also, the Coulomb repulsion is different for on-site (U_p, U_d) and intersite (U_{pd}) repulsion. Note that the energy of the *charge-transfer* (CT) from Cu to O is given by

$$\Delta = \varepsilon_{Cu} - \varepsilon_O = \varepsilon_d - \varepsilon_p. \tag{2.19}$$

This equation will be used in the discussion of the parent compound lanthanum cuprate in chapter 4.3.

Depending on the relative strength of Coulomb repulsion and hopping strength, several scenarios can be realized in cuprates, illustrated by the *Zaanen-Sawatzky-Allen scheme* [Zaanen et al., 1985; 1986, Damascelli et al., 2003] shown in Fig. 2.3: As mentioned, hybridization plays a strong effect. When completely neglecting correlations (i.e. $|U| \ll 1$), it would split up the Cu
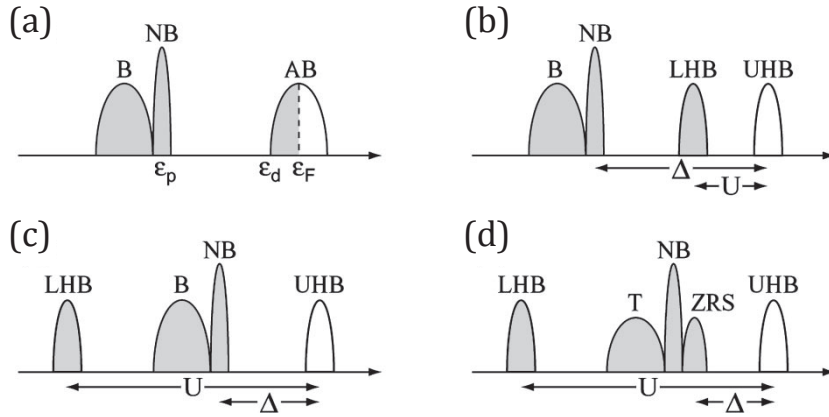
Figure 2.3 – *Adapted from [Damascelli et al., 2003, Fig. 13]*. Density of states for cuprates in the Zaanen-Sawatzky-Allen scheme. (a) bonding (B), antibonding (AB) and non-bonding (NB) states in a square lattice for negligible correlations, $|U| \ll 1$, (b) Mott insulator, $\Delta > U > W$, (c) CT insulator, $U > \Delta > W$, (d) appearance of triplet and Zhang-Rice singlet in the CT insulator due to hybridization. Shaded areas indicate occupied states.

$3d_{x^2-y^2}$-O $2p_{x,y}$ hybrid orbital into bonding, non-bonding and antibonding orbitals (panel (a)). The material would be conducting due to the partial filling of the antibonding orbital. The effect of U is to split the antibonding orbital into the *Upper* and *Lower Hubbard Bands* (UHB/LHB). If U is smaller than the CT energy Δ, but larger than the width W of the Hubbard bands, the material becomes a Mott insulator (panel (b)). Instead, if U becomes larger than Δ, the LHB is pushed below the states originating from the oxygen $2p$-orbitals, the system turns insulating with a band gap determined by the CT energy Δ, and is thus called a *charge-transfer insulator* (panel (c)). This is the case in cuprates, and the parent compound LCO discussed in chapter 4.3 is indeed a CT insulator. Lastly, the bonding band was long thought to be split into a singlet state at E_F and lower-lying triplet states (panel (d)) due to hybridization with the UHB. The role of the so-called *Zhang-Rice singlet* and the validity of the one-band model it is derived from are still debated in literature [Lau et al., 2011, Ebrahimnejad et al., 2014]. It should be noted that Fig. 2.3 is more of an artist's impression than a realistic scenario. In reality the different bands drawn in the figure are not separated, but overlap. The d-bands in particular easily spread out over several eV [Eskes and Sawatzky, 1988].

The above models have all been derived starting from the undoped Cu-O plane, and succeed in describing the general characteristics of cuprates. However, the situation becomes more complex upon increasing the doping. Figure 2.4 displays experimental and computational results for the in-plane conductivity $\sigma_{\perp c}$ of the prototypical $La_{2-x}Sr_xCuO_4$ system in the normal state. The undoped parent compound is an antiferromagnetic (AFM) CT insulator with the CT peak around 2.1 eV. Upon doping, the system becomes increasingly metallic, and the CT peak is significantly broadened. In addition to the Drude peak, a mid-IR feature, which is attributed to charge ordering, appears around 1 eV. The description becomes more involved when considering both the temperature- and doping dependence, leading to the full phase diagram in Fig. 2.5, as discussed in literature [Varma, 2010]. The schematic phase diagram
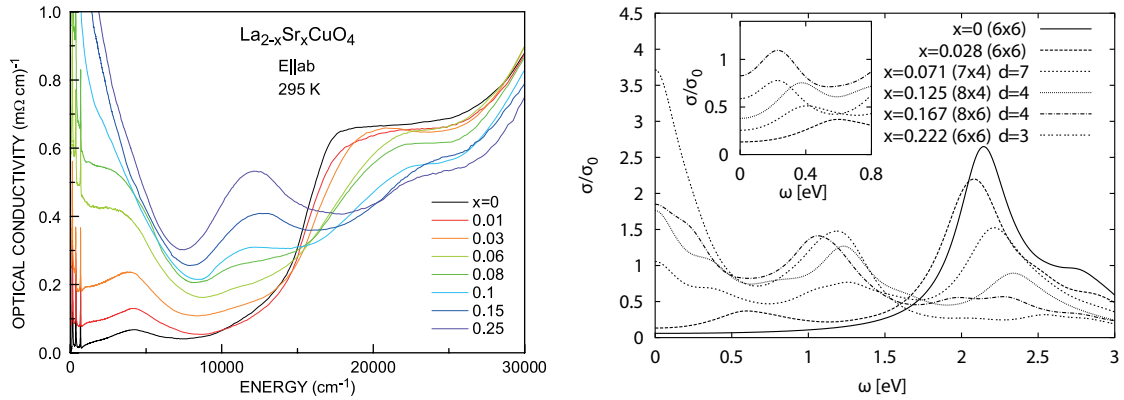
Figure 2.4 – (a) *Adapted from [Sugai et al., 2013]*. In-plane optical conductivity $\sigma_{\perp c}$ of La$_{2-x}$Sr$_x$CuO$_4$ as a function of doping, obtained from reflectivity data via Kramers-Kronig transformation. (b) *Adapted from [Lorenzana and Seibold, 2003]*. Cluster calculation of $\sigma_{\perp c}$ as a function of doping, assuming charge-ordering in the form of stripes. The cluster size and (where applicable) inter-stripe distance are given in the labels.

shown here only contains the most important phases, and the exact features are still heavily debated. The antiferromagnetic CT insulating state shows its maximum Néel temperature T_N^0 for zero doping. T_N^0 is typically above room temperature; for lanthanum cuprate the maximum value is 340 K [Kastner et al., 1998]. The AFM state is extremely susceptible to doping, and vanishes already for low values of $x = 0.02$. It is thus a suitable measure for low doping concentrations. For larger dopings, a dome-shaped superconducting state emerges, with the maximum transition temperature T_C^0 lying just below $x = 0.16$. For La$_{2-x}$Sr$_x$CuO$_4$, this maximum temperature is about 39 K, but much higher temperatures can be achieved. The first T_C value above 77 K, the nitrogen boiling point, was reported for YBa$_2$Cu$_3$O$_{7-\delta}$ with a transition temperature of $T_C \approx 97$ K [Wu et al., 1987]. A striking feature of the superconducting phase of cuprates is the fact that, in contrast to the classical BCS systems described in chapter 2.4, the superconducting order parameter shows a d-wave symmetry [Scalapino, 1995, Damascelli et al., 2003], i.e. the gap has a fourfold symmetry in k-space. An interesting region is the doping regime below the optimum doping. The cuprates in general exhibit a charge-density wave state in this region, assumed to be one-dimensional, i.e. stripe-like [Lorenzana and Seibold, 2003]. Notice that there is a "dent" in the dome on the underdoped side. This is most likely an effect of competition between charge ordering and superconductivity. In the same underdoped region, but at a temperature T^* much closer to room temperature, the material enters a *pseudogap* (PG) phase [Marshall et al., 1996]. This state is a seemingly normal metallic state that exhibits a gap across parts of the Fermi surface. Note that the pseudogap is clearly distinct from the superconducting gap, and it was discussed whether the two can coexist, or do compete [Damascelli et al., 2003]. The nature of the pseudogap is debated, and will be discussed in the context of the experiments on slightly underdoped NdBa$_2$Cu$_3$O$_{7-\delta}$ in chapter 4.4. On the overdoped side of the superconducting dome, the material is in a "strange metallic" (non-Fermi liquid) state for higher temperatures / lower doping, while at
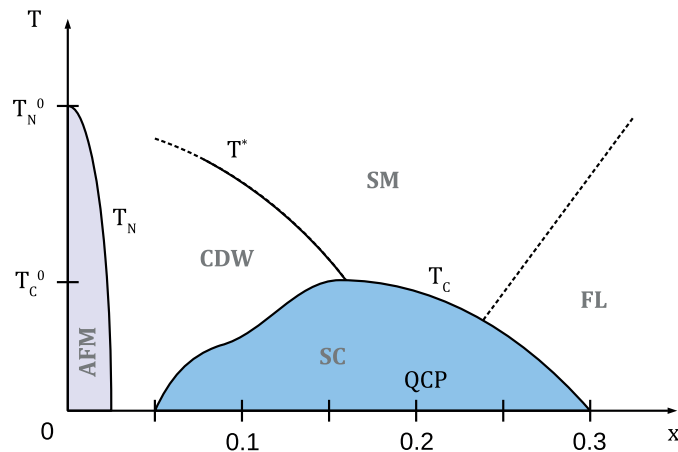
Figure 2.5 – A simplified generic phase diagram for cuprates as discussed in literature (e.g. [Varma, 2010]). Undoped cuprates are antiferromagnetic (AFM) CT insulators with a maximum Néel temperature T_N^0 for zero doping. As the doping hole concentration x increases, T_N decreases rapidly and reaches zero around $x = 0.02$ [Kastner et al., 1998]. For larger dopings, a superconducting (SC) dome develops, reaching the maximum T_C^0 just below $x = 0.16$. Notice the "dent" in the dome on the underdoped side, where there is a competition between the SC state and a charge-density wave (CDW). Also, above T_C but below T^*, cuprates exhibit a pseudogap phase, whereas for higher temperatures, they show "strange metallic" (SM), i.e. non-Fermi liquid behavior. The SM phase shows a crossover to Fermi liquid (FL) behavior. At the conceived meeting point of T^* and the SM-FL crossover lines, a quantum critical point (QCP) is thought to exist, roughly at $x = 0.2$. Notice the some aspects of the phase diagram are heavily debated, and not all regions are fully explored.

lower temperatures / higher doping the system enters a Fermi liquid state. Notice that at the point where the extensions of the pseudogap transition line and the Fermi liquid-strange metal transition line would meet inside the superconducting dome, a *quantum critical point* is thought to exist around $x = 0.2$ [Damascelli et al., 2003].

3 Methods

This chapter gives an overview of all relevant experimental details, and explores the possible applications of the pump-probe setup used in this thesis for future experiments. It also serves as a reference for anyone interested in the specifics, and contains all information needed to obtain the data presented in the following chapters. Any reader familiar with ultrafast optical experiments can safely skip reading this chapter, and come back later for details.

There are three important steps to each experiment. The first step is obtaining a suitable sample with an optical grade surface, as well as proper static data on the surface to be studied. A general description of the sample growth is given in chapter 3.1; the parameters specific to each sample are discussed in the chapters presenting the results. A crucial ingredient for a successful time-resolved experiment is the availability of static data on the sample under study. While extensive literature data are usually available for many systems, each sample is unique in some way and can show features that differ from literature. Therefore, whenever possible, static data should be taken before the time-resolved experiment. The method of choice is spectroscopic ellipsometry, discussed in chapter 3.2, because it provides access to the full complex optical permittivity ε. The second step, performing the actual time-resolved experiment, is presented in chapter 3.3. The pump-probe setup used to acquire the data is discussed in terms of the optical setup, the detection electronics, and the cryogenic system. In broadband optical spectroscopy, short laser pulses trigger dynamics on the timescale relevant for electronic and phononic processes, allowing to disentangle processes occurring on different time scales that would be averaged over in static measurements. In addition, the time-resolved experiment is phase-sensitive. The spectroscopic information allows to translate any observed dynamics to physical observables, and it avoids the pitfall of over-interpreting dynamics at a single energy, which is always a challenge when using monochromatic (single- or double-wavelength) techniques. The latter offer no possibility to distinguish between intrinsic physical behavior and an effect that is happening at the observed wavelength only, such as a non-linear spectroscopic dependence, or is present simply because of cross-correlation effects due to the choice of the laser energy. Lastly, as a general feature of pump-probe experiments, the polarization control of the laser beams grants access to Raman-sensitive processes on

the meV scale in addition to the observed eV scale, with the possibility of exploring their symmetry. Chapter 3.3 also discusses the best achievable results with the used setup, and further applications that may prove fruitful in new experiments. Finally, chapters 3.4 and 3.5 describe the analysis procedures that are used in this thesis.

3.1 Sample preparation

A large effort is typically invested in the preparation of samples for optical studies. All experiments have to be performed on surfaces of correct crystallographic orientation and sufficient smoothness. In general, the preparation comprises three phases: the growth of the crystal, its orientation by means of Laue diffraction, and the cutting and polishing of a sample with an oriented surface. The prepared surfaces are typically a few mm in diameter, which allows to scan the significantly smaller laser spots to a clean area of the surface even if the polishing is not homogeneous. Note that the minimum surface required for the experiment is about 200 μm in diameter, making measurements on very small samples possible. All samples are attached to a sample mount using fast-drying silver paint, i.e. a solution of Ag in methyl isobutyl ketone.

The cuprate samples discussed in chapter 4 were all prepared in a similar manner: First, polycrystalline samples are prepared from a set of precursor materials through a solid state reaction at high temperatures, with several intermediate grindings. The doping is adjusted via the composition of the precursors. The resulting powder is then pressed into a rod and sintered. A homogeneous crystal is grown from the rod using a floating zone process. The rod is treated in an optical floating zone furnace, which uses mirrors to focus light from high-power light sources onto the rod, melting the area in the focus. This heating zone is then slowly moved across the crystal, leaving behind a mostly defect- and grain-free region. The crystal structure is seeded by the oriented part below the heating zone. The orientation of the rod is determined in a Laue diffractometer. The diffraction pattern is fitted with a simulated pattern of the known space group using an appropriate software.[1] The oriented rod is then cut parallel to the desired surface using a diamond wire saw. Polishing is usually done from the backside, gluing the cut surface to a mount and removing material on the opposite side of the crystal. The surface is polished with a series of silicon carbide discs of decreasing roughness, and later on with diamond paste or diamond sand paper. For experiments in the visible range, a final polishing grain size between 0.25 and 1 μm is sufficient, depending on the sample material.

The TaS$_2$ samples used in the experiments of chapter 5 were instead grown by means of *chemical vapor transport* (CVT). This procedure produces flakes of few mm in diameter and some 100 μm thickness. Since TaS$_2$ is a layered material, the flake surfaces are parallel to the layers of the crystal structure. The surfaces are not suited for polishing as described above, but are typically of optical quality and can be used as-grown. If instead a fresh surface is desired, a flake can be glued to a substrate and a few layers of material can be removed by placing and

---

[1] I recommend the software CLIP [Schumann, 2009] for fitting the pattern.
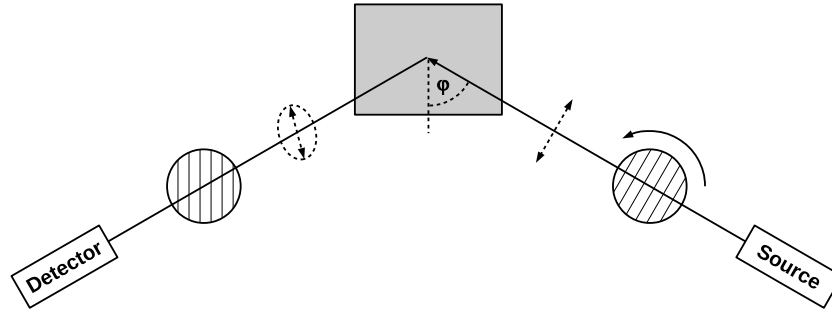
Figure 3.1 – Ellipsometry measurement scheme in fixed polarizer configuration.

removing a piece of adhesive tape, a process commonly known as "scotch taping". Before the experiment, the in-plane orientation of the crystal axis can again be identified by means of the Laue diffraction pattern.

3.2 Ellipsometry

Ellipsometry is an optical technique that allows to recover the full complex permittivity ε (or conductivity σ) by measuring the complex ratio ρ of parallel to perpendicular reflectivity of a material,

$$\rho := \frac{r_p}{r_s} \equiv \tan(\Psi) \cdot e^{i\Delta}. \tag{3.1}$$

As usual, the indices p and s refer to polarizations parallel and perpendicular to the plane of incidence. Since according to Fresnel's formulas r_p and r_s differ even in an isotropic material for non-normal incidence angles ϕ, the polarization of a linearly polarized beam reflected from the sample surface will undergo an elliptical distortion. Ellipsometry measures the amplitude Ψ and phase Δ of ρ, from which the optical constants can be calculated. As discussed in literature [Dressel and Grüner, 2002], the permittivity can be expressed as

$$\varepsilon_1 = \sin^2(\phi) \cdot \left(1 + \frac{\tan^2(\phi)\left(\cos^2(2\Psi) - \sin^2(\Delta)\sin^2(2\Psi)\right)}{(1 + \sin(2\Psi)\cos(\Delta))^2} \right) \tag{3.2}$$

and

$$\varepsilon_2 = \sin^2(\phi) \cdot \frac{\tan^2(\phi)\sin(4\Psi)\sin(\Delta)}{(1 + \sin(2\Psi)\cos(\Delta))^2}. \tag{3.3}$$

It can be seen from these equations that small errors in ϕ will have a huge impact on the results, making the calibration of an ellipsometry setup very challenging.

A standard scheme for performing ellipsometry measurements is the fixed polarizer configuration illustrated in Fig. 3.1. The beam of a light source, typically a gas lamp, is polarized using a rotating polarizer. Upon reflection from the sample surface, the polarization undergoes the
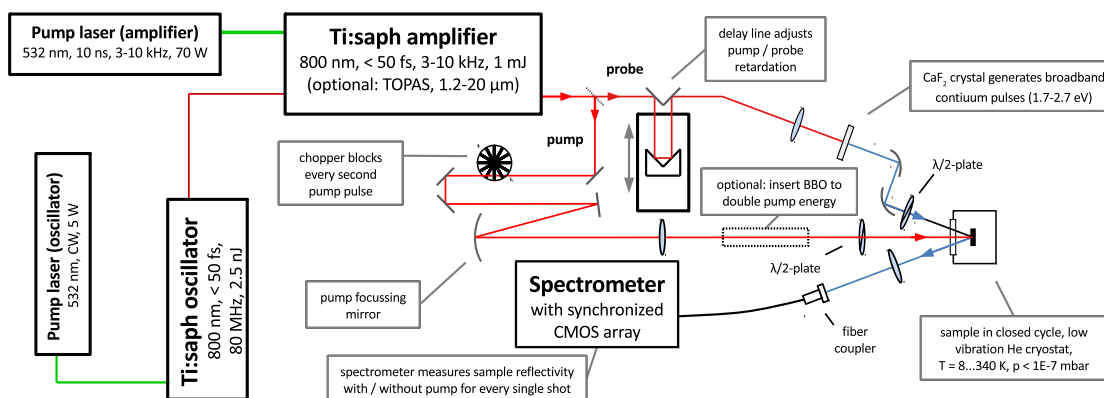
Figure 3.2 – A diagram of the experiment, detailing the laser system and pump-probe setup.

above-mentioned elliptical distortion. The beam passes through an analyzer kept at a fixed angle and arrives at the detector. The measurement of the quantity ρ is performed by rotating the polarizer angle as well as repeating the experiment for various angles of incidence ϕ. Since the quality of the measurement critically depends on the precision with which ϕ is determined, the beam arms are mounted on a goniometer whose exact angle is determined by measuring the ellipsometric response for a well-characterized reference surface, typically a gold film. Apart from precise determination of the angles in the experiment geometry, ellipsometric measurements also need an incident beam that is polarized to a high degree. In and close to the visible range, crystalline polarizers of high extinction ratios on the order of $1:10^6$ are readily available, so it is sufficient to use a simple lamp as a light source. In the far infrared (FIR), strongly polarized light of high brightness is provided by the THz emission of a synchrotron.

3.3 Optical Pump-Probe Setup

The ultrafast broadband reflectivity setup that was used to obtain the time-resolved optical data is laid out in a standard pump-probe configuration. An overview of the setup and its laser system is given in Fig. 3.2. The output of a pulsed laser is split in two parts: The major portion, called pump beam, is used to excite the sample under investigation in order to trigger dynamics. The sample response is then investigated using the probe beam that is reflected from the sample and collected into a detector. Time-resolved information is obtained by varying the delay between pump and probe beam using a retroreflector mounted on a mechanical delay stage. The power of the probe beam is set to a fraction of that of the pump beam to ensure that the observed phenomena are caused by the pump excitation alone.

In the setup used for this thesis, a titanium-doped sapphire (Ti:saph) amplified laser system (model Wyvern-1000 from KM Labs, seeded by a Griffin oscillator) provides sub-50 fs pulses at 1.55 eV (800 nm) with a repetition rate of 3-10 kHz at a pulse energy of up to 3 mJ. In a basic configuration, a few μJ of the laser output are used for the pump beam when exciting a sample at 1.55 eV. Optionally, the pump output is frequency-doubled to 3.1 eV using a

Figure 3.3 – A diagram of the synchronization electronics.

β-barium borate (BBO) crystal, or can be tuned between 1.2 and 20 μm using an optical parametric amplifier (model TOPAS-C, with NDFG stage, from Light Conversion). The white light pulse serving as the probe beam is generated by focusing pulses with an energy of about a μJ into a calcium fluoride (CaF$_2$) crystal of 3 mm thickness using a combination of a lens with short focal distance and an iris to limit the numerical aperture of the incoming beam. The generated continuum ranges from 1.7 to 2.7 eV and is peaked around 2.2 eV. The CaF$_2$ crystal is mechanically oscillated to slow down degradation by spatial hole-burning caused by the high laser intensity. The residual component of the generating beam at 1.55 eV is eliminated using a low-pass colored glass filter, and the divergent white light beam is collimated and focused onto the sample in a dispersion-free manner using a pair of off-axis parabolic mirrors, impinging onto the sample surface at an angle of 15-20°. The spot sizes of the pump and probe beams at the sample surface are measured by a CCD-based beam profiler. Typical full width/ half maximum (FWHM) dimensions of the near-Gaussian profiles are 150 x 150 μm^2 for the pump beam and 50 x 50 μm^2 for the probe beam. The polarizations of the pump and probe beams are adjusted using half-wave retardation plates.

The specular reflection of the probe beam is collimated into an optical fiber using an achromatic lens. The fiber couples the beam into a $4f$-spectrometer that is using a linear complementary metal oxide semiconductor (CMOS) array as a detector. The electronic shutter of the CMOS detector is synchronized to the incoming laser pulses through a series of electronic circuits, based on phase-locked loops (PLLs), sketched in Fig. 3.3. The core piece is a 16-bit analog-to-digital converter (ADC) that produces a master clock pulse train at 11 MHz, fast enough to read out all 1024 detector pixels from pulse-to-pulse at the maximum laser repetition rate of 10 kHz. The master clock is synchronized to a trigger signal from the amplifier pump laser, and ultimately paces the readout operations of the CMOS array. The same trigger signal is halved in frequency and sent to the chopper controller, which synchronizes the rotation of the mechanical chopper blade to the incoming laser pulses. The chopper runs at a quarter of the laser repetition rate, blocking and letting pass pulses in pairs of two. This is done to average out excessive laser noise at half the repetition rate caused by alternating

21

over- and undersaturation of the amplifier pump laser's gain medium, a behavior colloquially known as "ding-donging". A gate signal is created using the reference output of the chopper controller, and then combined with the trigger signal. This gated trigger is finally used to start the data acquisition process of the CMOS array. Along the way, several extra delays are added to compensate for cable lengths, beam propagation, and positioning of the various elements along the beam path. Using this process, it is ensured that 1. the electronic shutter of the CMOS array is opened in a time window around the arrival of the laser pulses, 2. the shutter is closed between the arrival of pulses to reduce background noise, and 3. all detector pixels are read out in the period between pulses. The synchronization of the detector is further explained in [Ham, 2011].

The differential reflectivity change $\Delta R/R$ is extracted from the data by calculating the quantity

$$\frac{\Delta R}{R}(\omega, t) := \frac{R^{\text{odd}}(\omega, t) - R^{\text{even}}(\omega, t)}{R^{\text{odd}}(\omega, t) + R^{\text{even}}(\omega, t)} - R^{\text{dark}}(\omega) \tag{3.4}$$

where R^{odd} and R^{even} are the two arrays containing the sums over the spectra received from the ADC. The offset spectrum $R^{\text{dark}}(\omega)$ is acquired before every scan by measuring the light entering the fiber when the probe beam is blocked, eliminating scattered pump light as well as any ambient light from the acquired spectra. It is important to note that the sign of the right-hand side of Eq. (3.4) depends on the electronic phase offset of the chopper as well as its position along the beam path, which have to be adjusted properly to obtain the physical reflectivity change of the sample. Finally, the dataset $\Delta R/R(\omega, t)$ containing the reflectivity change at every time delay for every probe energy is retrieved in the form of a rectangular matrix. In a typical experiment, the acquisition of each matrix is repeated multiple times to improve the statistics of the measurement. The experiment therefore strongly relies on the repeatability of scans, meaning the samples have to be stable under laser light for hours. Acquiring a dataset for one set of experimental parameters (fluence, polarization, sample temperature) typically takes between a few hours and a day, depending on the signal level and the desired signal-to-noise ratio.

Before the data are analyzed, the reflectivity spectra have to be corrected for the *Group Velocity Dispersion* (GVD) of the probe beam. Since the probe beam is not dispersion-compensated after generation of the white light, the probe pulses arrive at the sample stretched to a duration of few ps. This is beneficial for the experiment, because it significantly reduces the momentary probe light intensity in the sample and thus, the pump-to-probe power ratio. It is noteworthy that the probe beam dispersion is not a limiting factor for the time-resolution of the setup, which is given on the detection side by the much smaller effective pulse duration per detector pixel. The correction of the GVD is done numerically by defining values for time-zero (i.e. pump-probe overlap) for a number of probe energies across the spectrum by looking at the time traces $\Delta R/R(t)$. Typically, the onset of the signal can be used as point of overlap. The final result depends a lot on the exact method used to define time-zero given a certain slope, but consistent results can easily be achieved due to the fact that the GVD can be represented as a

Taylor series with sizable contributions only up to third order. While the time traces can be understood in terms of the sample response to a δ-like excitation convolved with the Gaussian shape of the pump pulse, it is in general not necessary to deconvolve the traces to obtain the true pump-probe overlap in time. It should be noted, however, that the GVD correction has an intrinsic uncertainty that can not be pushed very far below half the pump pulse duration. The raw data are corrected for GVD by shifting each time trace by its assigned time-zero value, as well as subtracting any possible offsets caused by noise in the offset spectrum from Eq. (3.4). The matrix is then trimmed around the edges to eliminate missing data points.

Integrating over a typical value of 1000 laser shots per acquisition, the setup has an intrinsic noise level of about 0.1 % RMS. The main noise sources are the amplifier output noise, which is strongly increased by the nonlinear white light generation process, the electronic noise of the CMOS array and the noise due to AD conversion. The signal-to-noise ratio is improved statistically by repeating each measurement many times, typically up to 100 scans per matrix. In addition, the output of several detector pixels is binned, averaging in energy. In this way, relative reflectivity changes below 10^{-4} can be observed. The earlier implementation of the setup used a reference beam geometry, where a portion of the white light was split off before reflection of the sample and coupled into a second spectrometer identical to the first one in use. The reflectivity change was corrected for a "fake" contribution calculated from the reference signal, which was caused by the strong shot-to-shot noise of the white light in the old setup. Since the new system has a significantly reduced noise level, but is limited in resolution by the low probe light intensity arriving at the detection array, the reference beam was eliminated.

The cryostat assembly used for optical experiments, shown in Fig. 3.4, is based on a closed-cycle liquid helium cold head (model DE-204 from Advanced Research Systems, Inc.) with a vibration-reducing gas interface. The cryostat expander is mounted to the laboratory ceiling, while the cold head and cryostat shroud are supported from the optical table, completely isolating the latter from the strong vibrations of the expander. The cold head allows for experiment temperatures between 8 K and 340 K. Samples are mounted using fast-drying silver paint on a small copper plate attached to a copper wire of 2 mm thickness descended from the cold head. The sample shroud is a custom design made of aluminium, allowing for the application of an external magnetic field, and is fitted to a standard CF flange using a soft, annealed copper gasket. Optical access is provided via a 1" window port at the front. The window material chosen according to the pump and probe energies of the experiment. For experiments in the visible/NIR range, CaF_2 is used. A turbo pump, backed up by an oil pump, is attached to the back of the shroud, the proximity to the sample significantly improving the vacuum. The vacuum pressure is measured by a sensor attached to the cold head shroud. Typical pressures range from 10^{-7} mbar at room temperature to 10^{-8} mbar at 10 K. Usually, the vacuum is improved after closing the cryostat by heating up to the maximum temperature over night. Since most sample surfaces, especially cuprates, suffer from adsorption of carbon-oxide compounds at low temperatures, samples have to be warmed up above ~230 K after about 2 hours at low temperatures to restore the reflectivity of their surface.
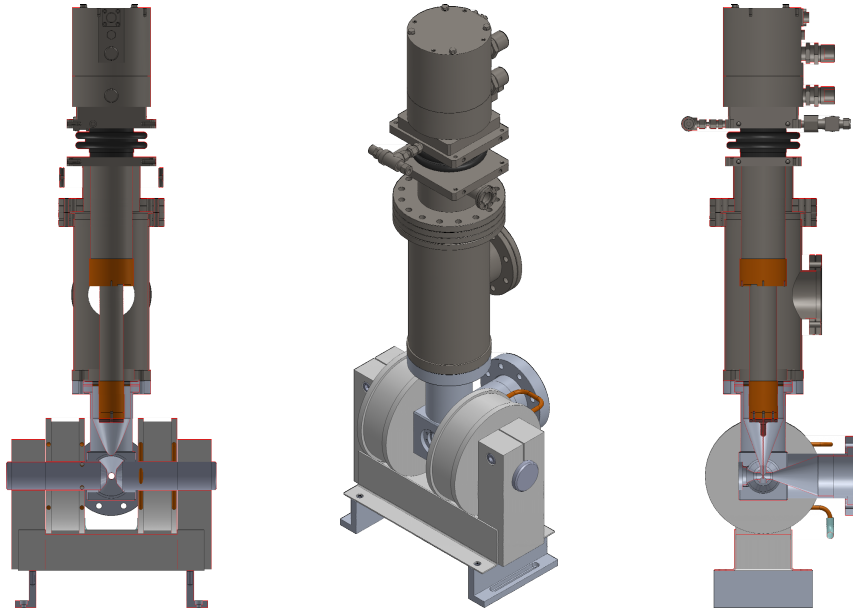
Figure 3.4 – The cryostat assembly with the magnet in position. From top to bottom, the assembly comprises the expander (dark gray), the gas interface (black), the cold head shroud (dark gray), and the aluminium sample shroud (light gray).

Apart from standard transient reflectivity measurements, the cryostat can also be used in high-resolution single-wavelength pump-probe measurements, transient magneto-optic Kerr effect (MOKE) measurements, and ellipsometric measurements. The sample shroud depicted in Fig. 3.4 is optimized for normal-incidence reflectivity and MOKE measurements. The small cubic sample space of about 1 cm edge length allows bringing the poles of the electromagnet used for MOKE measurements (model 3470 by GMW associates) close enough to the sample to achieve in-plane fields of up to 1 T. Since ellipsometric measurements are typically performed at incident angles around 70°, a different shroud with three windows was designed for these experiments. It features probe entrance and exit windows under 70° with respect to the pump entrance window.

3.4   Data analysis

The analysis of the broadband reflectivity data is performed using either a global fit procedure, or a singular value decomposition (SVD) algorithm. For a global fit, the reflectivity data from Eq. (3.4) are binned into horizontal (energy-averaged) slices, and each slice is fitted with the same fit function. Certain fit parameters (e.g. time constants, oscillation frequencies) are shared between all or some traces, while others (e.g. amplitudes) are left to vary from trace to trace. As mentioned in chapters 2.2 and 2.3, the chosen fit function is typically a combination of exponential decays and damped oscillations.

The alternative method, SVD, utilizes the fact that any rectangular matrix $\mathbf{M} \in \mathbb{R}(m, n)$ can be

uniquely decomposed into a sum of tensorial vector products [Trefethen and Bau, 1997] of the form

$$\mathbf{M}(m, n) = \sum_{i=1}^{N} \lambda_i u_i'(x) \otimes v_i(y) = \sum_{i=1}^{N} u_i(x) \otimes v_i(y). \tag{3.5}$$

The $\lambda_i \in \mathbb{R}$ are the sorted singular values, $\lambda_1 \geq \lambda_2 \geq \lambda_3 \geq \ldots$, the "$\otimes$" denotes the outer product, N is called the rank of the matrix $\mathbf{M}$ and $u_i(x) \in \mathbb{R}(m)$ and $v_i(n) \in \mathbb{R}(y)$ are called canonical traces. In the second form, the singular value is absorbed in the definition of the canonical trace u_i. By construction, the canonical traces are orthogonal, $v_i \cdot v_j = \delta_{ij}$ and $u_i \cdot u_j = \lambda_i^2 \delta_{ij}$. SVD is often used as a noise reduction technique. This is because the singular values λ_i typically decay very fast with increasing i, and then level off at a certain rank, when the contribution of the tensor products falls below the overall noise level of the measurements. It is usually safe to reconstruct the data using only pairs up to this critical rank, which significantly reduces noise in the data while still reproducing all significant features. SVD is easily applied to the transient reflectivity data from Eq. (3.4). The data come in the form of a rectangular matrix with m time points and n energy values. The decomposition yields the canonical time traces $u_i(t)$ and canonical energy vectors $v_i(t)$. These traces can then be fitted in a similar manner to the global fit procedure, using the same fit functions.

It should be noted here that the canonical traces in general do not have any physical meaning. They are chosen by the SVD algorithm to be orthogonal, whereas the contributions to the reflectivity from different physical processes in general are not. In order to obtain a physically meaningful decomposition, one can make an argument based on the large separation of energy (resp. time) scales of the phenomena observed in real time, which is on the order of $\hbar\omega \sim 10$ meV for phonons and comparable excitations, and the energy range of the probe spectrum, $E > 1.5$ eV. In the spirit of the Born–Oppenheimer approximation it can be assumed that the differential reflectivity at high energies can be taken as a parametric function of a set of "slow" variables $\xi_\nu(t)$ describing the out-of-equilibrium state produced by the pump. Here, the time t is measured relative to the arrival of the pump pulse. Examples of slow variables ξ_ν are ionic displacements and "slow" charge and magnetic fluctuations, either coherent or incoherent. "Fast" fluctuations produced by the pump are either relaxed after the pump passage (~ 50 fs) or not resolved. Thus, it is possible to expand the differential reflectivity as a function of the "high" probe energy E and time delay t as

$$\left(\frac{\Delta R}{R}\right)(t, E) = \sum_{i=1}^{N_p} \left(\frac{\partial \ln\{R\}}{\partial \xi_i}\right)(E) \; \xi_i(t). \tag{3.6}$$

Typically, the sum can be restricted to a small number N_p of physical processes which contribute significantly. In particular, the sum can be partitioned into an oscillatory part $\left(\frac{\Delta R}{R}\right)^{\text{osc}}(t, E)$ and a relaxational part $\left(\frac{\Delta R}{R}\right)^{\text{rel}}(t, E)$. Eq. (3.6) allows to represent the full two-dimensional data in terms of a few time dependencies of the excitation coordinates $\xi_i(t)$ and their associated energy dependencies $\left(\frac{\partial \ln\{R\}}{\partial \xi_i}\right)(E)$. It is therefore helpful to fit the canonical traces with a model function that resembles the physical contributions identified in the

spectrum, and perform a linear transformation

$$u_i(t) = \sum_{j=1}^{N_p} a_{ij} U_j(t) \qquad \text{and} \qquad V_j(E) = \sum_{i=1}^{N_c} v_i(E) a_{ij},$$ (3.7)

yielding the physical time and energy traces $U_i(t) \propto \xi_i(t)$ and $V_j(E) \propto \left(\frac{\partial \ln\{R\}}{\partial \xi_i} \right)(E)$. Note that $\sum_{i=1}^{N_c} a_{ij}{}^2 = 1$ and $V_i{}^2 = 1$. The decomposition into physical traces is used in chapter 4.3 for the analysis of the coherent phonon generated in lanthanum cuprate.

Both the global fit and SVD procedures have advantages and disadvantages, and care has to be taken when deciding which one is more suited for a dataset. It is noteworthy that a global fit is often a highly unstable procedure, because a typical number of 10 or 20 fitted slices easily requires 100 independent fit parameters. It is therefore necessary to provide adequate starting values for the fit. SVD on the other hand is easy to perform and leads to a small set of traces with little noise, but has trouble capturing certain features. This is especially true if the data contain nonlinear features, e.g. a peak that gradually shifts in frequency as time evolves. This evolution can only be captured by a very large number of tensorial products, eliminating the main advantage of using the SVD algorithm. As a consequence, SVD also reacts badly to improper GVD correction, which is a problem if the reflectivity data contain regions of low signal intensity, or a crossover region close to the edge of the measured spectrum.

3.5 Drude-Lorentz modeling

In the treatment of the time-resolved data, it can prove useful to analyze the dynamics in terms of transient permittivity or conductivity rather than reflectivity. It is possible to calculate the full complex $\varepsilon = \varepsilon_1 + i\varepsilon_2$ (or $\sigma = \sigma_1 + i\sigma_2$) from the reflectivity change $\Delta R/R$ with good accuracy using static ellipsometry measurements discussed in section 3.2. The transient complex quantities can instead be obtained from the reflectivity data using a Drude-Lorentz (DL) model [Dressel and Grüner, 2002]. The DL model describes the response of a material as a set of damped harmonic oscillators, which are characterized by their (natural) frequency ω_0, plasma frequency ω_p, and linewidth γ. The first oscillator, at zero frequency, is called Drude peak and models the response of the material's conduction carriers. It should be noted that this peak is always present in real (non-superconducting) materials, even in insulators, because they always possess a finite resistance. Peaks at higher frequencies are associated with interband transitions or optically active bosonic excitations like phonons. The total, complex permittivity is given by

$$\varepsilon(\omega) = \varepsilon_\infty + \sum_i \frac{\omega_p^{(i)2}}{\omega_0^{(i)2} - \omega^2 - i\gamma^{(i)}\omega},$$ (3.8)

where the constant ε_∞ absorbs contributions from high-frequency oscillators. The fit was performed using the software RefFit [Kuzmenko, 2014], provided by Dr. A. Kuzmenko of the
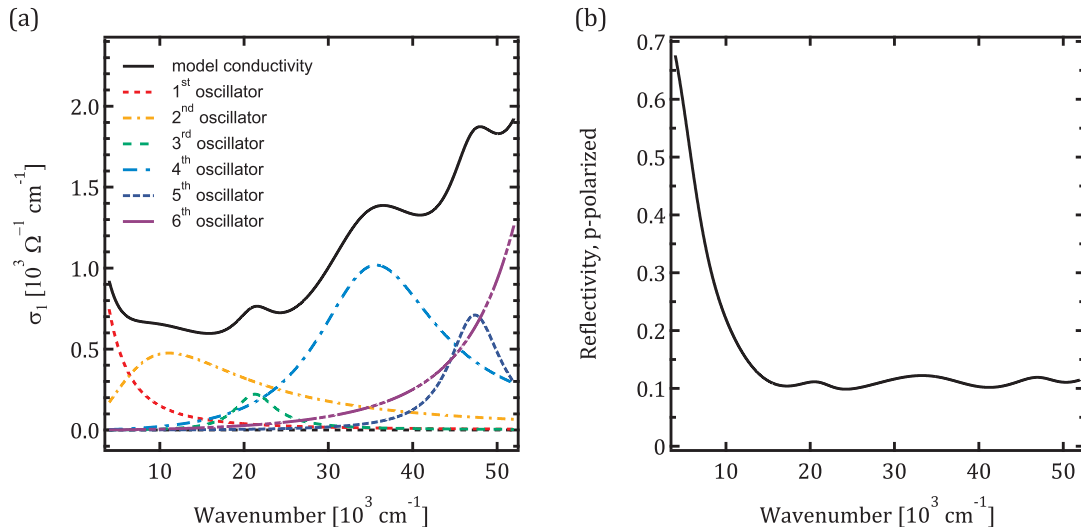
Figure 3.5 – Example of a Drude-Lorentz model: (a) model for the real part of the static conductivity σ_1, fitted to data calculated from ellipsometry, comprising six oscillators. (b) reflectivity R_p corresponding to the static conductivity

University of Geneva. The software is used to fit a model comprising a suitable number of oscillators to static optical data of the material under study. Reliable results are only achieved if static ellipsometry data are available, preferably taken on the same sample surface used in the time-resolved experiments. An example of such a model is shown in Fig. 3.5, for data on NBCO (cf. chapter 4.4) taken at 15 K: The static conductivity was calculated from spectroscopic ellipsometry, and a model comprising six oscillators is fitted to σ_1. Here, the first oscillator at zero energy is not a real Drude peak, but represents all contributions below the measured range, including the superconducting peak at zero energy present in the material at the temperature of the measurement. The figure also shows the reflectivity calculated from the model.

The model from Fig. 3.5 can be used to calculate the transient permittivity (or conductivity) from the time-resolved reflectivity data. To this end, the time-resolved data from Eq. (3.4) are cut into differential reflectivity spectra $\Delta R/R(\omega; t)$ at each time delay t. The total reflectivity $R(\omega; t)$ can be calculated by multiplication with the static reflectivity determined from the Drude-Lorentz model. These data are imported to RefFit, and for each time point a new model is fitted simultaneously to the time-resolved and static data, using the static model as a basis. For this step, the static data are only limited to the spectral range where no time-resolved data are present, with a gap left to avoid numerical artifacts at the boundaries caused by spectral weight shifting into or out of the range of the time-resolved measurement. It is advisable to limit the fit parameters of the model to oscillators that have significant weight in the spectral range of the time-resolved experiment. It is helpful to first perform a fit using variational dielectric functions (VDFs, see [Kuzmenko, 2014, ch. 2.2.4.]), even though this often suffers from numerical problems at the edges of the data range. A realistic result is then obtained
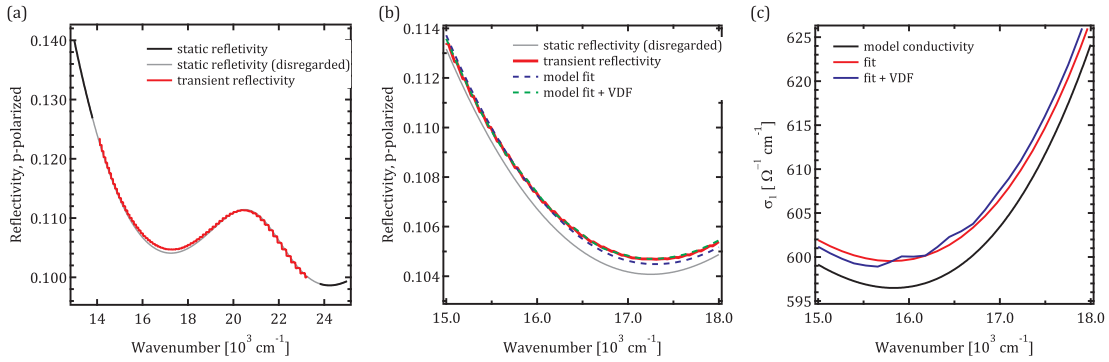
Figure 3.6 – Time-resolved fit of a Drude-Lorentz model: (a) static reflectivity from the model shown in Fig. 3.5, with the central portion replaced by the transient reflecitvity spectrum. (b) fit curves for the transient spectrum in the spectral region of the biggest change with and without VDF, as explained in the text. (c) original model conductivity, and fit of the transient conductivity with and without VDF in the same region.

by repeating the fit without the use of VDFs, leaving a sufficient number of fit parameters free to obtain a similar result. The fit procedure is illustrated in Fig. 3.6: Panel (a) shows the reflectivity data used for fitting the model. The central part of the static reflectivity data is replaced by the transient reflectivity spectrum. Note that the change in reflectivity is very small, typically not above few percent. Panel (b) shows the fit to the transient data in the region of the biggest change. Only the third oscillator from Fig. 3.5 (a) that is centered in the region where transient data were taken was left completely free, while the oscillators one, two and four that have significant contributions in the probe range were allowed to change their plasma frequency, i.e. effectively their amplitude. Also shown is a fit using a VDF. Panel (c) shows the resulting change in the model conductivity in the same region as panel (b), again with and without the VDF. Notice that the fit including the VDF curve matches the transient spectrum in panel (b) perfectly, but, as mentioned, the VDF procedure introduces artifacts in the conductivity in panel (c).

Once the Drude-Lorentz models for every time delay are obtained, the optical conductivity σ is directly available from RefFit. The full differential conductivity $\Delta\sigma/\sigma(\omega, t)$ is calculated by dividing the model results by the static conductivity, and reconstructing the matrix from the spectra at fixed time delays. As mentioned, the analysis of time-resolved conductivity data is easier than that of the reflectivity data, since it contains direct information on the dynamical change of interband transitions and the shift of spectral weight.

4 Experiments on cuprate super-conductors

In this chapter, I will sum up the optical experiments on cuprate superconductors that I performed or took part in during my PhD.

The experiments on cuprates presented in the following treat three different scenarios, all of which illustrate different aspects of cuprates: After a brief review of previous experiments on cuprates in chapter 4.1, a study of a coherent excitation of the superconducting condensate in optimally doped LaSCO is presented in chapter 4.2. It is shown that the condensate can be excited by an ISRS process, and what information can be obtained by studying the material's spectroscopic response to the charge fluctuation. This technique is accordingly named *Coherent Charge Fluctuation Spectroscopy* (CCFS). The elegance of the CCFS approach lies in the specificity of the excitation, because unpaired electrons are not excited by ISRS. Thus, the experiment provides a kind of inverse approach compared to the isotope effect, in the sense that the coupling of the SC condensate to any excitations on the eV energy scale is investigated to obtain information on the pairing mechanism. The experiment on LaSCO is a prime example of how the generation a coherent oscillation on the meV scale influences the optical properties of a correlated material in the visible regime. Extending on this, a more in-depth treatment of the same ISRS-based technique is presented for the generation of a coherent phonon in the (nearly) undoped parent compound LCO in chapter 4.3. The main objective of the experiment is to explore whether one can extract reliable numbers for microscopic variables from the study of the response of the correlated system to the coherent excitation. Indeed, it is demonstrated that the electron-phonon (el-ph) coupling can be extracted in good agreement with theoretical considerations, and this process is applicable to virtually any correlated material where coherent phonons can be generated. In analogy to CCFS, this technique is named *Coherent Lattice Fluctuation Spectroscopy* (CLFS). Lastly, chapter 4.4 presents experiments on NBCO in the slightly underdoped regime. This study focuses on the quasiparticle (QP) dynamics and their evolution with temperature in order to shed light on the superconducting pairing mechanism. Over the past decade, a multitude of ultrafast studies have been performed on 123-family cuprates in order to unravel the nature of the pseudogap phase. The experiments on NBCO are highly interesting, because they not
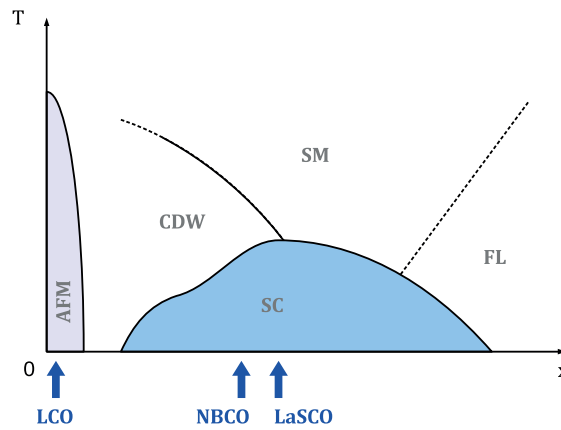
Figure 4.1 – The three different dopings for cuprates discussed in this thesis in the generic phase diagram from Fig. 2.5: optimally doped LaSCO (right arrow), (nearly) undoped LCO (left arrow), and slightly underdoped NBCO (middle arrow).

only allow to trace all these results in a single experiment, but also provide evidence for the existence of preformed Cooper pairs lacking phase coherence throughout almost the entire pseudogap phase. The three different scenarios are marked in the general cuprate phase diagram in Fig. 4.1.

4.1 A quick overview of previous studies on cuprates

Since the discovery of high-temperature superconductivity in cuprates [Bednorz and Müller, 1986], the family of cuprates has undergone an enormous amount of scrutiny. Many questions have been solved, and many more remain unanswered, or suffer from a highly controversial debate. It is by far beyond the scope of this thesis to review all important studies and results, so the discussion will be limited to those immediately relevant to the experiments performed for this thesis. The interested reader is invited to explore one of the many good summaries given in literature [Damascelli et al., 2003, Devereaux and Hackl, 2007, Carbone, 2007, Grüninger, 1999, Mansart et al., 2013].

As mentioned in chapter 2.4, superconductivity requires that electrons form Cooper pairs and condense collectively in a macroscopic quantum state, and that by means of the isotope effect it was shown that phonons act as the glue promoting the pairing. This scenario breaks down in cuprates, where the observation of an analogous fingerprint of the glue involved in the pairing mechanism – if any exists at all – has been lacking. In consequence, the correct framework to understand superconductivity in cuprates is still a subject of an intense debate [Anderson, 2007, Maier et al., 2008, Zaanen, 2011]. One possibility is that the role of phonons in the traditional mechanism is replaced by a different low energy bosonic excitation like damped magnons which act as a glue allowing the pairing of electrons [Scalapino, 1995, Pines, 1997]. In this scenario, superconductivity can be understood in the traditional framework [Eliashberg, 1960] where retardation plays an important role. Anderson has argued that there is no such

low energy glue and that proximity to the Mott phase is an essential ingredient [Anderson, 2007]. The relevant time scale of the interactions inducing the pairing is the inverse of the (renormalized) Hubbard energy $U \geq 2$ eV. In this case, the interaction can be considered instantaneous for practical purposes. In trying to answer the question which scenario is real, pump-probe spectroscopy has proven to be of great value [Orenstein, 2012]. Most of the time-resolved studies on cuprates dealt with the investigation of dipole-allowed excitations. In general, the out-of-equilibrium distribution of particle-hole excitations created by the pump excitation decays to states within a few hundreds of meV of the chemical potential [Perfetti et al., 2007] on the time scale of the pulse duration. At this energy, phase space restrictions slow down the dynamics [Howell et al., 2004], so that the subsequent evolution can be studied using a probe pulse on the fs scale. The temporal resolution of the fs probe is comparable to the time scale of relevant processes in the material, like pair breaking, pair recombination, or the el-ph coupling time.

For a number of cuprates, the photoinduced quenching of the superconducting order parameter and its subsequent recovery could be traced by recording the temporal evolution of the gap amplitude in the optical spectrum [Kaindl et al., 2000, Stojchevska et al., 2011, Pashkin et al., 2010, Beck et al., 2011]. Remarkably, it was found that the energy needed to suppress the superconducting state in these materials is several times larger than the condensation energy [Stojchevska et al., 2011, Pashkin et al., 2010], in contrast to what happens in conventional superconductors where it is of the same order [Stojchevska et al., 2011, Beck et al., 2011]. Optical studies also provided insights on the relaxation dynamics of the excited quasiparticles [Beck et al., 2011, Gedik et al., 2004; 2005, Kabanov et al., 2005], and on the optical spectral weight transfers associated with the carriers' kinetic energy changes across the photoinduced phase transition [Giannetti et al., 2011]. Femtosecond Angle-Resolved PhotoEmission Spectroscopy (ARPES) showed that the decay of photoexcited carriers is dominated by the recombination of Cooper pairs at the antinodes, i.e. the copper-oxygen bond direction in real space [Cortés et al., 2011]. Similar experiments yielded an estimate of the el-ph coupling strength being in the intermediate regime [Perfetti et al., 2007], similar to what was found by fs-electron diffraction, which in turn was able to identify its anisotropy [Carbone et al., 2008; 2010]. Prior to the experiments reported in [Mansart et al., 2013], no optical experiments measuring a matrix element directly were performed in a correlated system, in spite of the fact that the optical generation of such excitations had already been reported [Albrecht et al., 1992, Misochko et al., 2002]. However, it was demonstrated that the same phonon matrix elements can be calculated from high-resolution EELS data when sufficiently precise numerical models are available [Qin et al., 2010].

Finally, a new type of experiments has emerged that is performed in the strong pumping regime with the aim of achieving coherent control of cuprate superconductors. Considerable progress towards this goal has been achieved by tailoring the optical excitation to be resonant with a selected collective mode in the mid- or far-infrared range. One of the most remarkable results is the establishment of a highly coherent state in a number of underdoped high-temperature cuprate superconductors upon resonantly driving a specific lattice vibration

using an intense mid-IR pump pulse [Fausti et al., 2011, Hu et al., 2014, Kaiser et al., 2014]. Characteristics of this transient state resemble the properties of the superconducting phase and are found to persist up to room temperature in underdoped $YBa_2Cu_3O_{7-\delta}$. A complete microscopic explanation for such an effect is still a topic of debate [Armitage, 2014]. The common point of these experiments is that they all rely on suppressing the charge order present in the underdoped regime, and that the SC-like state they induce exists within the pseudogap (PG) regime. While the latter point seems important, the nature of the PG remains elusive, despite extensive research. Several theories have been proposed to explain the emergence of this phenomenon. Typical scenarios described by so-called intrinsic theories involve phase fluctuation models [Emery and Kivelson, 1995], where the PG phase is interpreted as an SC state lacking macroscopic phase coherence. Precursor pairing models [Kosztin et al., 2000] suggest that the pair formation occurs at much higher temperature than the condensation and the resonant valence bond state [Anderson et al., 2004]. On the other hand, extrinsic theories suggest the existence of an incipient charge- or spin- density wave order competing with superconductivity [Chubukov and Schmalian, 1998]. Experimental evidence for all of these effects have been provided throughout the years [Vershinin et al., 2004, Yang et al., 2008, Kanigel et al., 2008, Hashimoto et al., 2015], indicating that the PG may well be the result of some complex mixture of these phenomena.

In this regard, special attention has been directed towards the transient optical response of the 123-family of high-temperature cuprate superconductors. High-energy ($\sim$ eV) in-plane interband transitions have been shown to offer insights into the low-energy ($\sim$ meV) QP dynamics at the antinodes of the Fermi surface [Han et al., 1990, Stevens et al., 1997, Gedik et al., 2004]. This observation has been corroborated by analyzing in detail the 123-compounds' electronic structure, revealing that such interband transitions promote carriers from the Lower Hubbard Band (LHB) to the Fermi energy E_F [Stevens et al., 1997, Fausti et al., 2014]. So far, the main limitation of such studies was the lack of combined spectral and temperature information, which does offer a novel perspective on the QP dynamics in a wide energy range. Broadband THz pulses were used to disentangle the QP and infrared-active phonon dynamics in the direct proximity of the gap [Pashkin et al., 2010], and the use of a broad visible probe revealed the impact of QP and coherent Raman-active excitations on the typical energy scale of Mott-Hubbard physics [Giannetti et al., 2011, Fausti et al., 2014, Mansart et al., 2013]. Furthermore, in yttrium barium cuprate (YBCO), an anomaly of the coherent out-of-plane Ba breathing mode was observed at the superconducting phase transition, and has been shown to be caused by the abrupt change in Bogoliubov QP density [Albrecht et al., 1992, Fausti et al., 2014], with the amplitude of the mode being proportional to the number of broken Cooper pairs. The case of YBCO is important, because a considerable number of time-resolved experiments has been performed using pump and probe photon energies in the optical range on a variety of samples spanning the whole phase diagram [Stevens et al., 1997, Thomas et al., 1996, Mihailovic et al., 1998; 2000]. These experiments identified three distinct time scales for the QP relaxation dynamics in pump-probe experiments, which will be of importance and discussed in detail in chapter 4.4.

4.2   Optimally doped Lanthanum Strontium Cuprate

In this chapter the technique of Coherent Charge Fluctuation Spectroscopy (CCFS) is presented in detail. This chapter has been adapted in large parts from [Mansart et al., 2013] and [Lorenzana et al., 2013]. CCFS takes advantage of the fact that the paired electrons in a cuprate SC are Raman active, as will be elucidated below. In the experiment, coherent charge fluctuations are generated in a superconductor by laser excitation through a stimulated Raman process using the physics discussed in chapter 2.3. These coherent excitations are subsequently monitored by the fs broadband probe pulse, allowing to observe the real-time oscillations of the Cooper pair condensate and their impact on high-energy excitations. The experiment has a strong analogy to the coherent control of spins with NMR or ESR techniques. Furthermore, the experiment can be interpreted in terms of the Anderson-Higgs mechanism: The induced charge fluctuations are basically oscillations of the SC gap (i.e., the amplitude mode) that are coupled to phase oscillations because the SC pair density and phase are conjugate variables.[1] It is beyond the scope of the present discussion to elaborate this view on the experimental results, but for the interested reader a number of good summaries of the topic is available, e.g. [Varma, 2001, van der Marel, 2004].

To understand the analogy between superconductivity and magnetism, it is useful to employ Anderson's pseudospin formalism [Anderson, 1958, Warner and Leggett, 2005]. This formalism is based on the fact that, despite their obvious physical difference, the two phenomena are closely linked from a mathematical (or purely formal) point of view. Anderson's idea was to map the occupation of states in a superconductor to three double-site states representing respectively a doubly-occupied state, an empty double state, and a state occupied by a Cooper pair. The operators $\sigma_{\mathbf{k}}^x$, $\sigma_{\mathbf{k}}^y$, and $\sigma_{\mathbf{k}}^z$ representing these states behave like spin-1/2 operators, so they are called *pseudospins*. They are defined as

$$\sigma_{\mathbf{k}}^x = (c_{\mathbf{k}\uparrow} c_{-\mathbf{k}\downarrow} + h.c.), \qquad i\sigma_{\mathbf{k}}^y = (c_{\mathbf{k}\uparrow} c_{-\mathbf{k}\downarrow} - h.c.), \quad \text{and} \quad \sigma_{\mathbf{k}}^z = 1 - n_{\mathbf{k}\uparrow} - n_{-\mathbf{k}\downarrow}, \tag{4.1}$$

where $n_{\mathbf{k}\sigma} = c_{\mathbf{k}\sigma}^\dagger c_{\mathbf{k}\sigma}$. The electron creation and destruction operators $c_{\mathbf{k}\sigma}^\dagger$ and $c_{\mathbf{k}\sigma}$ following the convention from Eq. (2.14).

Anderson's idea is illustrated pictorially in Fig. 4.2: The fully occupied pair ($\mathbf{k}\uparrow$, $\mathbf{-k}\downarrow$) is represented by a down pseudospin in momentum space (A), the state in which the pair is empty by an up pseudospin (B), and the Cooper pair by a sideways pseudospin (C). The representation of normal and SC states of an *s*-wave system in this formalism are shown for $T = 0$ in Fig. 4.2 (D) and (E): In the normal state $u_{\mathbf{k}} = 0$ (cf. Eq. (2.15)), and $v_{\mathbf{k}}$ is different from zero only for states inside the Fermi surface, which corresponds to empty pairs above the chemical potential (up pseudospins) and fully occupied pairs below the chemical potential (down pseudospins), leading to the pseudospin texture shown in Fig. 4.2 (D), with a sharp interface at the Fermi surface. In the superconducting state, mixing of empty and fully occupied pairs,

---

[1] Recently, an experiment that was heavily inspired by the results presented here has been performed in a BCS superconductor [Matsunaga et al., 2014].
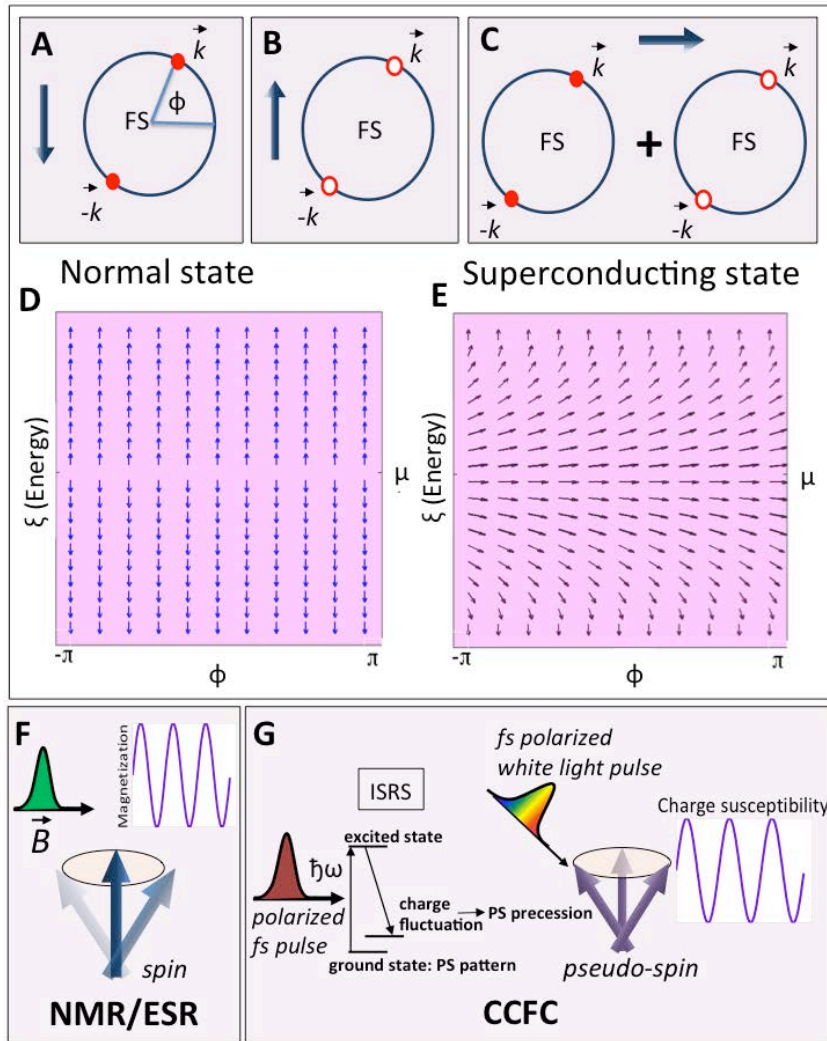
Figure 4.2 – *Adapted from [Mansart et al., 2013].* Pseudospin description of the Coherent Charge Fluctuation Spectroscopy experiment. Panel (*A*) defines the angle ϕ along the Fermi surface (FS). The three upper panels define the pseudospin operators in momentum space: A pseudospin down corresponds to the pair of states (**k** ↑, **-k** ↓) being fully occupied (*A*), a pseudospin up to the pair (**k** ↑, **-k** ↓) being empty (*B*), and a sideway pseudospin to a quantum superposition of the previous two (*C*). Panel (*D*) and (*E*) show the pseudospin pattern in the normal state and in the case of an *s*-wave superconductor respectively. Rather than plotting the pseudospins as a function of momentum **k**, a change of coordinates is made and the energy distance ξ of the state **k** from the chemical potential μ is plotted as a function of the Fermi surface angle ϕ. (*F*) Schematic view of an NMR/ESR experiment in which the spins precess, inducing a magnetization oscillation, and (*G*) corresponding view for a CCFS experiment, in which the pseudospins precess upon ultrafast excitation and generation of the coherent charge fluctuation.

which becomes maximum at the chemical potential, blurs the Fermi surface, leading to the texture shown in panel (E).

Using a properly tuned light pulse, coherent control of the pseudospins in a superconductor can be achieved through an ISRS process, which triggers the precession of the pseudospins around their equilibrium axis, as discussed in more detail below. This is analogous to NMR and ESR experiments in which magnetic field pulses induce a precession of real spins [Slichter, 1996]. The analogy between the two types of experiments is depicted in Fig. 4.2 (F) and (G). The polarized infrared fs pump pulse couples to charge fluctuations in a superconductor according to Raman selection rules. It impulsively perturbs the system and induces the pseudospin precession, i.e. the oscillations of the Cooper pair condensate. The optical spectra of the system are then monitored in real time at different energies, revealing the optical transitions that respond to the oscillating condensate; this allows to single out those excitations that can potentially mediate electron-electron interactions impacting the formation of Cooper pairs. Such an experiment is of pivotal importance for cuprates, since, as mentioned in chapter 4.1, the applicability of conventional pairing theories [Eliashberg, 1960], based on retarded interactions between electrons mediated by low energy glue bosons, has been doubted [Anderson, 2007, Zaanen, 2011] and a completely different framework has been proposed involving non-retarded interactions associated with electronic high-energy scales [Anderson, 1987].

For the experiment, an optimally doped LaSCO crystal was prepared following the procedure described in chapter 3.1: First, polycrystalline $La_{2-x}Sr_xCuO_4$ samples were prepared by a solid state reaction using the starting materials La_2O_3, $SrCO_3$ and CuO with 99.99% purity. The materials were mixed and ground followed by a heat treatment in air at 900-1050° C for more than 70 hours with several intermediate grindings. The phase purity of the resulting compound was checked with a conventional x-ray diffractometer. The resulting powder was hydrostatically pressed into rods of 7 mm in diameter and subsequently sintered at 1150° C for 20 hours. The crystal growth was carried out using an optical floating zone furnace (FZ-T-10000-H-IV-VP-PC, Crystal System Corp., Japan) with four 300 W halogen lamps as heat sources. The growth conditions were as follows: The growth rate was 1 mm/h, the feeding and seeding rods were rotated at about 15 rpm in opposite directions to ensure the liquid's homogeneity, and an oxygen and argon mixture at 3 bar pressure was applied during growth. The as-grown crystals were post-annealed at 850° C in order to release internal stress and to adjust the oxygen content. Two samples were prepared from one of the resulting single crystals, at optimal doping, by cutting, polishing and orienting the single crystal to obtain two surfaces containing the *ab* and the *ac* planes, respectively. The pump-probe experiments were performed as described in chapter 3.3. The setup used was the older 1 kHz system that included a reference for the probe beam; this version of the setup is described in detail in [Mansart et al., 2012]. All measurements were taken at an absorbed fluence of about 300 $\mu J/cm^2$ unless otherwise stated. The pulse duration of $\sim$ 45 fs puts a lower limit to the frequency of the excitations that can be excited via ISRS, $\omega > 1/(45 \text{ fs})$ [Merlin, 1997].

The broadband reflectivity dynamics are displayed in Fig. 4.3 (A)-(C). The crucial point of the
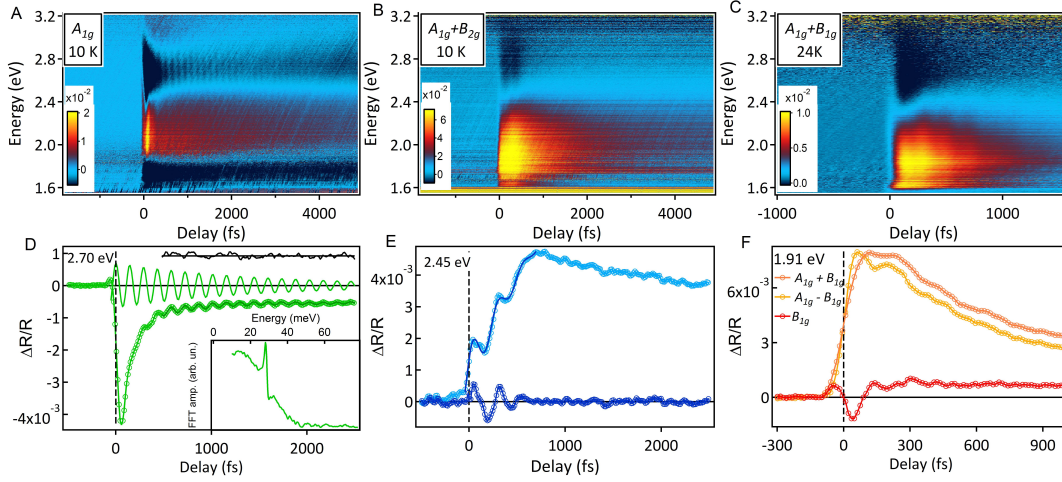
Figure 4.3 – *Adapted from [Mansart et al., 2013].* Transient broad-band reflectivity data at 10 K in A_{1g} (pump $\parallel$ [100], probe $\parallel$ [001], (A, D)), $A_{1g} + B_{2g}$ (pump $\parallel$ [110], probe $\parallel$ [110], (B, E)) and, at 24 K, $A_{1g} + B_{1g}$ (pump $\parallel$ [100], probe $\parallel$ [100], (C, F)) geometries. All geometries are specified in tetragonal axes. The extracted profiles are shown in panels (D–F) for selected probe energies. The inset in panel (D) shows the FFT of the extracted A_{1g} phonon oscillation. Panel (E) presents the B_{2g} reflectivity oscillations obtained by subtracting the background from the profile, and in panel (F) the difference between the $A_{1g} + B_{1g}$ and $A_{1g} - B_{1g}$ profiles is shown, which is proportional to the B_{1g} signal. The absorbed pump fluence is 300 μJ/cm^2.

experiment is the use of different experimental geometries for exploiting the Raman selection rules for excitation and detection discussed further below to obtain information on final states of different symmetry. In the first geometry (panel (A)), the electric field of the pump is parallel to the Cu-O bond, giving access to Raman excitations with $A_{1g} + B_{1g}$ symmetry, while the probe beam is polarized along the c-axis, allowing to detect only the fully symmetric A_{1g} excitations. Next, the pump and probe fields are polarized along the diagonal direction, giving access to $A_{1g} + B_{2g}$ Raman excitations. Panel (B) shows the response when pumping along the diagonal ([110]) direction. Probing parallel or perpendicular to the pump beam along the [110] and [1$\bar{1}$0] directions gives access to $A_{1g} + B_{2g}$ and $A_{1g} - B_{2g}$ Raman excitations, respectively. The B_{2g} signal can be extracted by taking the difference between the two spectra. Similarly, the $A_{1g} + B_{1g}$ and $A_{1g} - B_{1g}$ excitations can be accessed when pumping along the [100] direction and probing along [100] and [010], respectively. The $A_{1g} + B_{1g}$ spectrum is shown in panel (C). All three spectra are dominated by a large abrupt amplitude change followed by an exponential relaxation. This is a consequence of high-energy particle-hole (p-h) excitations produced by the dipole-allowed absorption of the pump photons, as discussed in chapter 2.2. For all polarization configurations the transient reflectivity changes sign throughout the spectra in correspondence to specific electronic transitions. These changes reflect the transfer of spectral weight among the different absorption bands produced by the p-h excitations [Giannetti et al., 2011]. The number of p-h excitations involved is estimated to be less than 10^{-2} per Cu atom (see the discussion of Fig. 4.7).

All geometries show coherent oscillations of Raman excitations on top of the dipole *p-h* excitations' relaxation, as shown in the time traces in Fig. 4.3 (D-F), taken at selected energies where the oscillation amplitude is the largest. These profiles are representative of the full data sets for a given geometry as far as the oscillation phase and frequency are concerned.[2] In A_{1g} symmetry, an oscillation with a period of 145 fs and a long coherence time of ~ 1.45 ps is visible at all wavelengths (Fig. 4.3 (A) and (D)). The Fourier transform of the A_{1g} symmetry data is presented as an inset in Fig. 4.3 (D). A sharp peak at 28 meV (226 cm^{-1}) is visible, corresponding to the out-of-plane La A_{1g} breathing mode of LaSCO seen in static Raman scattering [Sugai et al., 2003]. In this mode, the apical oxygen atoms move in antiphase with the La atoms. The excitation of such coherent fully symmetric modes has already been observed in high-T_c superconductors [Albrecht et al., 1992, Mazin et al., 1994]. Instead, for both $A_{1g} + B_{2g}$ and B_{1g} symmetries (Fig. 4.3 (E) and (F); note the difference signal in the latter), slower and strongly damped oscillations of ~ 300 fs coherence time are clearly observed below T_c. The Fourier analysis of these time-resolved profiles is presented in Fig. 4.4 (A-B). In $A_{1g} + B_{2g}$ symmetry, at a probe energy of 2.45 eV, the temperature dependence of the Fourier-transform signal shows an obvious peak at 18 meV that vanishes above T_c (Fig. 4.4 (B)). In B_{1g} symmetry, the broad peak appears at energies around 24 meV when the sample temperature is lower than T_c. Increasing the pump fluence to 2 mJ/cm^2, no such peak could be observed below T_c (Fig. 4.4 (A)). This is a clear indication that an absorbed fluence of 300 μJ/cm^2 does not completely evaporate the SC condensate in the probed sample volume, whereas a much stronger pump beam is able to do so. Fig. 4.4 (C-D) displays the THz spectra obtained in the superconducting state, and compares them to the spontaneous Raman response (data taken from [Sugai et al., 2003]), which is well understood in terms of the excitation of two Bogoliubov quasiparticles [Devereaux and Hackl, 2007]. The good agreement between them allows to identify the strongly temperature-dependent part of the oscillations as Raman charge fluctuations of the SC condensate. This agreement is expected if one extends the theoretical considerations on ISRS to the electronic case, as is done in detail further below. The experiment detects remnants of superconductivity at fluences of the same order but larger than previously reported [Pashkin et al., 2010, Cortés et al., 2011]. This can be attributed to the bulk character and the much higher sensitivity to superconductivity of the pump-probe experiment. Presumably, superconductivity is indeed quenched on the first layers of the sample and becomes invisible to surface-sensitive probes like photoemission spectroscopy [Cortés et al., 2011].

The temporal evolution of the coherent phonon oscillation in the A_{1g} channel is presented in Fig. 4.3 (D), with its extrapolation down to zero-time delay (as defined in [Mansart et al., 2012]), establishing its cosine waveform, which is typical of a displacive (resonant) mechanism of excitation, as discussed in chapter 2.3. The electronic transitions induced by 1.55-eV-photons occur between the ground state of the material and higher energy electronic states. At this energy, a peak in the optical absorption is observed in LaSCO, which has been attributed to

---

[2]Note that the oscillation phase is constant across the spectrum, in accordance with the generation by ISRS discussed in chapter 2.3.
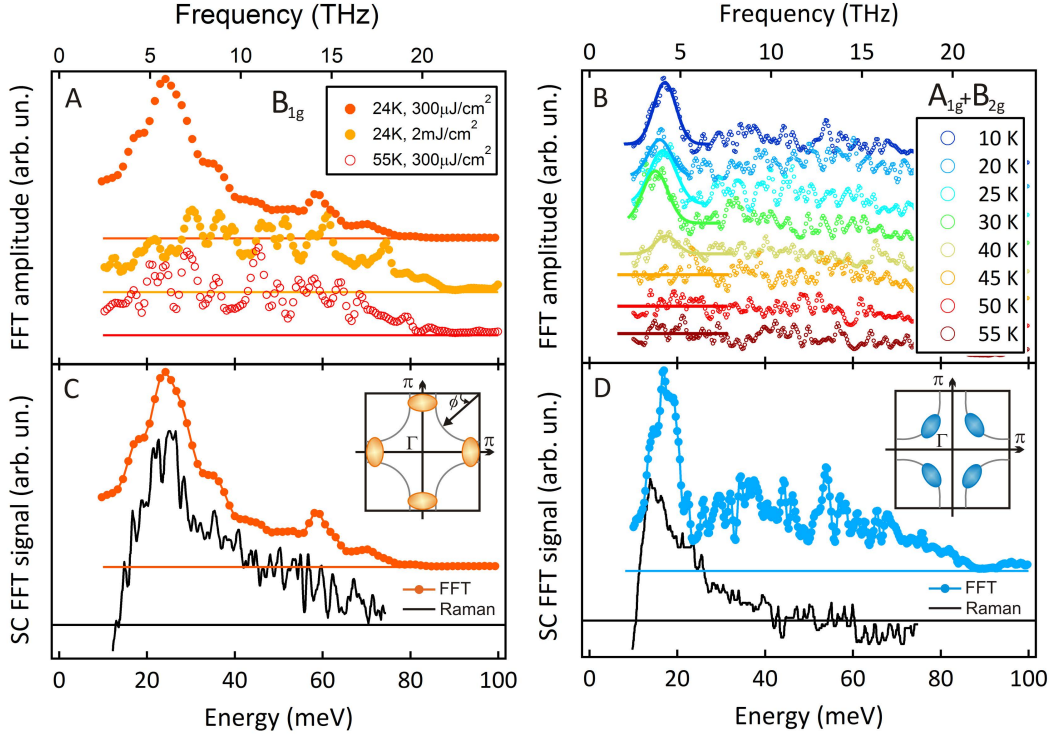
Figure 4.4 – *Adapted from [Mansart et al., 2013].* Fourier transform spectra obtained at different temperatures and pump fluences in B_{1g} (panel (A), 1.91 eV probe energy) and $A_{1g} + B_{2g}$ (panel (B), 2.45 eV probe energy) geometries. Panels (C) and (D) show the comparison between transient reflectivity data and Raman measurements, in the superconducting phase. The spontaneous Raman spectra are the difference between superconducting and normal phases, showing only the charge fluctuation peaks. The insets schematically show the angle ϕ along the Fermi surface and the regions in momentum space excited in (C) B_{1g} symmetry and (D) B_{2g} symmetry.

charge ordering in the form of stripes (cf. Fig. 2.4). It is clearly distinct from the remnant of the Cu-O CT peak [Uchida et al., 1991]. The cosine wave form indicates that, not unexpectedly, the charge modulations are strongly coupled to the A_{1g} La phonon. In the A_{1g} geometry, the presence of the strong coherent phonon disturbs the real-time observation of any possible coherent contribution of the SC condensate. Instead, in both $A_{1g} + B_{2g}$ and B_{1g} symmetries (Fig. 4.3 (E-F)), fluctuations of the SC quasiparticles starting at zero time delay are clearly visible, allowing the determination of a sine waveform. This indicates that, contrary to the A_{1g} phonon case, the triggering mechanism is ISRS as discussed in chapter 2.3, meaning that the *p-h* excitations at the energy of the pump pulse are not directly coupled to the SC quasiparticles. It is shown below that an analysis of the probe energy dependence leads to the same conclusion.

In order to understand the origin of the coherent charge fluctuations seen in the experiment, it is necessary to take a closer look at their generation mechanism. It is shown in the following

that the fluctuations are generated by an electronic analogon of the phonon ISRS mechanism discussed in chapter 2.3 in which the electrostrictive force $F(t)$ from Eq. (2.10) is generated by charge fluctuations that couple to the pump photons. Within a one-band description of electrons close to the Fermi surface, uniform (i.e. zero-momentum) charge fluctuations are described by the operator N_X [Devereaux and Hackl, 2007] that is defined as

$$N_X = \sum_{\mathbf{k}\sigma} f_{\mathbf{k}}^X n_{\mathbf{k}\sigma}, \tag{4.2}$$

where $n_{\mathbf{k}\sigma} = c_{\mathbf{k}\sigma}^\dagger c_{\mathbf{k}\sigma}$ again is the occupation operator for the state with wave vector $\mathbf{k}$ and spin σ, and $c_{\mathbf{k}\sigma}^\dagger$ and $c_{\mathbf{k}\sigma}$ are the creation and annihilation operators for electrons. The upper index of the symmetry factor $f_{\mathbf{k}}^X$ indicates the Raman symmetry, and the sum runs over all possible symmetries. In the present experiment, these are:

$$
\begin{aligned}
A_{1g}: \quad & f_{\mathbf{k}}^{A_{1g}} = [\cos(k_x a) + \cos(k_y a)]/2 \\
B_{1g}: \quad & f_{\mathbf{k}}^{B_{1g}} = [\cos(k_x a) - \cos(k_y a)]/2 \\
B_{2g}: \quad & f_{\mathbf{k}}^{B_{2g}} = \sin(k_x a)\sin(k_y a)
\end{aligned}
\tag{4.3}
$$

Generalizing the arguments for lattice ISRS in chapter 2.3 to electronic ISRS, the Hamiltonian of the system in the presence of the pump pulse can be written in analogy to Eq. (2.9) as

$$H = H_{BCS} + H_R,$$

where

$$H_{BCS} = \sum_k \xi_k n_{\mathbf{k}\sigma} - \sum_k (\Delta_k^* c_{-k\downarrow}^\dagger c_{k\uparrow}^\dagger + h.c.) \tag{4.4}$$

is the BCS reduced Hamiltonian from Eq. (2.14), with the gap replaced by the d-wave SC order parameter Δ_k, and

$$H_R = \sum_X v^X(t) N_X$$

is the perturbation due to the pump laser. Invoking again the Born-Oppenheimer argument that ω_L is much larger than the frequency of the fluctuations, the equivalent of the electrostrictive force $v_X(t)$ is given by

$$v_X(t) = -\frac{1}{2}\mathbf{E}(t) \cdot \frac{\partial \boldsymbol{\chi}(\omega_L)}{\partial \langle N_X \rangle} \cdot \mathbf{E}(t), \tag{4.5}$$

in direct analogy with Eq. (2.10). Here, $\boldsymbol{\chi}$ is the charge susceptibility, $\partial \boldsymbol{\chi}(\omega_L)/\partial \langle N_X \rangle$ is the conventional second-rank Raman tensor for electronic scattering with symmetry X and incident frequency ω_L [Cardona and Güntherodt, 1982], and $\mathbf{E}$ is the time-dependent electric field of the pump pulse.

To explain the observations from Fig. 4.3, it is necessary to look at the selection rules that apply to the generation of the coherent charge fluctuations. Since the driving force in Eq. (4.5) involves the Raman tensor, the selection rules have the same structure as in conventional Raman scattering. Disregarding orthorhombicity and using the D_{4h} group symmetry properties of the Raman tensor for a pump pulse polarized in the a-b-plane in LaSCO [Devereaux and Hackl, 2007], the Raman operator reads

$$
\begin{aligned}
H_R \;=\; & -\frac{E(t)^2}{2}\left[\frac{\partial \chi_{xx}}{\partial \langle N_{A_{1g}}\rangle}[(\hat{e}_x)^2 + (\hat{e}_y)^2]N_{A_{1g}} \right. \\
& \left. + \frac{\partial \chi_{xx}}{\partial \langle N_{B_{1g}}\rangle}(\hat{e}_x^2 - \hat{e}_y^2)N_{B_{1g}} + \frac{\partial \chi_{xy}}{\partial \langle N_{B_{2g}}\rangle}2\hat{e}_x\hat{e}_y N_{B_{2g}}\right],
\end{aligned}
\tag{4.6}
$$

with $\hat{\mathbf{e}}$ being a unit vector in the direction of the electric field ($\mathbf{E} = E\hat{\mathbf{e}}$) and the x-axis parallel to the Cu-O bond direction. It can be seen from Eq. (4.6) that for a pulse in the [100] direction, the $A_{1g} + B_{1g}$ symmetries are excited, as is displayed in Fig. 4.3 (A) and (C), while for an electric field aligned along [110], the $A_{1g} + B_{2g}$ symmetries are excited, as displayed in Fig. 4.3 (B). Selection rules for the detection can be derived analogously from Eq. (2.13), as shown below (cf. Eq. (4.14)). In the case of Fig. 4.3 (A) the probe field is in the [001] direction and only the A_{1g} component of the $A_{1g} + B_{1g}$ fluctuation can be seen. Using linear response for symmetry X, the fluctuations at zero temperature can be obtained via their Green's function as

$$
\langle N_X\rangle(t) = -\int_{-\infty}^{t}dt'\sum_{\nu}\sin[\omega_\nu(t-t')]|\langle 0|N_X|\nu\rangle|^2 v^X(t'),
\tag{4.7}
$$

with the sum running over a complete set of states. Here, $|0\rangle$ is the ground state before excitation and $|\nu\rangle$ the excited state in which the charge fluctuations N_X are present. If the pump pulse of width τ and amplitude E is approximated by a Dirac delta function ($v_X(t) = \delta(t)\tau E$), Eq. (4.7) yields a sinusoidal wave form with a shape determined by the Fourier transform of the conventional Raman scattering line shape for symmetry X [Devereaux and Hackl, 2007].

In the following, it is discussed how the charge fluctuations created by the force in Eq. (4.5) induced by the pump pulse affect the SC condensate. As mentioned above, this effect can be described using the pseudospin formalism. The reduced BCS Hamiltonian in the presence of a time-dependent potential acquires a simple form when written in term of the pseudospin operators $\boldsymbol{\sigma}_{\mathbf{k}}$ defined in Eq. (4.1),

$$
H_{BCS} = -\sum_{\mathbf{k}}\mathbf{b}_{\mathbf{k}}\cdot\boldsymbol{\sigma}_{\mathbf{k}},
\tag{4.8}
$$

where $\boldsymbol{\sigma}_{\mathbf{k}}$ is a Pauli matrix representing the pseudospin associated with the pair of states ($\mathbf{k}\uparrow$, $-\mathbf{k}\downarrow$) and $\mathbf{b}_{\mathbf{k}}$ is a fictitious *pseudomagnetic field*. At equilibrium, the pseudospins orient parallel

to the ground state pseudomagnetic field

$$\mathbf{b}_{\mathbf{k}}^0 = (\Delta_{\mathbf{k}}, 0, \xi_{\mathbf{k}}), \tag{4.9}$$

where $\Delta_{\mathbf{k}}$ is the SC order parameter and $\xi_{\mathbf{k}} = \epsilon_{\mathbf{k}} - \mu$ is the quasiparticle band energy from Eq. (2.14). Thus, the Hamiltonian in Eq. (4.8) expresses the familiar fact that the ground state wave function is determined by the mean-field order parameter $\Delta_{\mathbf{k}}$, which in turn can be expressed in terms of the pseudospins.

In the absence of superconductivity, $\Delta_{\mathbf{k}} = 0$, and the pseudomagnetic field points in the z direction and changes sign at the chemical potential, leading to the equilibrium texture of Fig. 4.2 (D). In the superconducting state, $\Delta_{\mathbf{k}} \neq 0$, and the pseudomagnetic field acquires a horizontal component, so that in the case of an s-wave superconductor the pseudospins display the texture shown in Fig. 4.2 (E). For a d-wave superconductor, the horizontal component of the pseudomagnetic field cancels along the nodal directions due to the gap anisotropy, leading to the texture of Fig. 4.5 (A) that has no sideways pseudospins along the nodal direction. According to Eq. (4.5), the Raman coupling of the pump pulse to the charge fluctuations, represented by the z-component of the pseudospins, can be described by a time-dependent potential $v_{\mathbf{k}}^X(t)$. The potential's shape in momentum space depends on the symmetry $X = A_{1g}$, B_{1g}, B_{2g} determined by the polarization of the pump pulse, Eqs. (4.2) and (4.3). Thus, the pseudomagnetic field becomes time-dependent:

$$\mathbf{b}_{\mathbf{k}}(t) = \mathbf{b}_{\mathbf{k}}^0 + \delta\mathbf{b}_{\mathbf{k}}(t), \qquad \text{with} \qquad \delta\mathbf{b}_{\mathbf{k}}(t) = \left(0, 0, v_{\mathbf{k}}^X(t)\right).$$

The pseudospins obey the usual equation of motion for magnetic moments in a time-dependent magnetic field [Anderson, 1958],

$$\hbar\frac{\partial\boldsymbol{\sigma}_{\mathbf{k}}}{\partial t} = -2\left[\mathbf{b}_{\mathbf{k}}^0 + \delta\mathbf{b}_{\mathbf{k}}(t)\right] \times \boldsymbol{\sigma}_{\mathbf{k}}. \tag{4.10}$$

This equation can be solved to first order by linearizing it in terms of the time-dependent fluctuations $\delta\boldsymbol{\sigma}_{\mathbf{k}}(t) \equiv \boldsymbol{\sigma}_{\mathbf{k}}(t) - \boldsymbol{\sigma}_{\mathbf{k}}^0$ [Parmenter, 1965]. Here, $\boldsymbol{\sigma}_{\mathbf{k}}^0$ is the equilibrium pseudospin texture shown in Fig. 4.5 (A). The linearized equation reads

$$\frac{\partial(\delta\boldsymbol{\sigma}_{\mathbf{k}})}{\partial t} = -2\mathbf{b}_{\mathbf{k}}^0 \times \delta\boldsymbol{\sigma}_{\mathbf{k}} - 2\delta\mathbf{b}_{\mathbf{k}} \times \boldsymbol{\sigma}_{\mathbf{k}}^0.$$

It is helpful to decompose the fluctuations as

$$\delta\boldsymbol{\sigma}_{\mathbf{k}} = \delta\sigma_{\mathbf{k}}^y\hat{\mathbf{y}} + \delta\sigma_{\mathbf{k}}^\perp\hat{\mathbf{e}}_\perp,$$

where the unit vector $\hat{\mathbf{e}}_\perp$ points in the direction perpendicular to $\mathbf{b}_{\mathbf{k}}^0$ and the y-axis. The axes are marked in Figs. 4.5 (B) and 4.6. For simplicity, the temperature is set to zero and collective effects as well as Coulomb interactions are neglected. The latter can be easily incorporated in the random phase approximation [Anderson, 1958, Devereaux and Hackl, 2007].
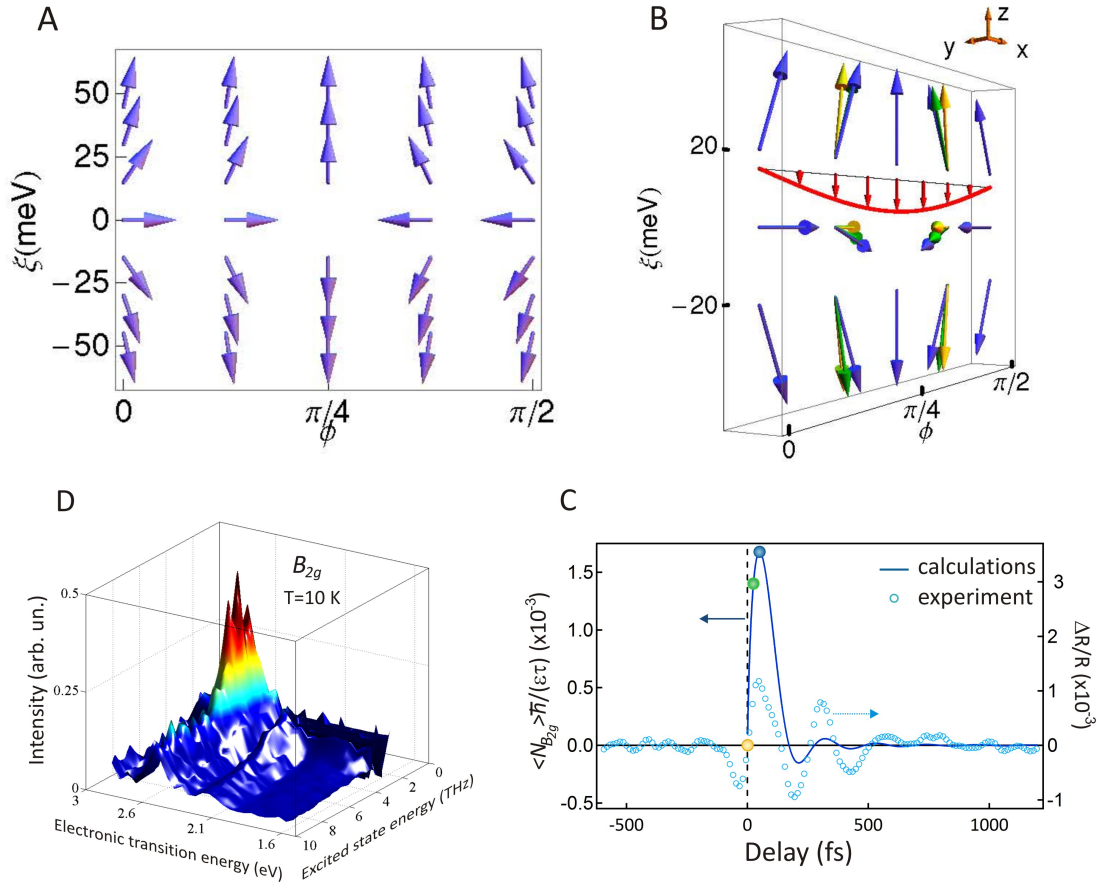
Figure 4.5 – *Adapted from [Mansart et al., 2013].* Pseudospin textures coding the BCS wave function in momentum space. (A) Ground state texture: pseudospins are labeled by the distance in energy from the Fermi level $\xi \equiv \xi_{\mathbf{k}}$ and the angle ϕ along the Fermi surface (inset of Fig. 4.3 (C). (B) Small red arrows: amplitude of the impulsive field $\delta \mathbf{b}_{\mathbf{k}}$ applied at $t = 0$ in B_{2g} symmetry. Long arrows: texture snapshots (amplitudes exaggerated for clarity) immediately after the excitation (yellow), at 25 fs (green) and at 50 fs (blue). (C) Theoretical charge fluctuation: Solid dots correspond to the snapshots of panel (B). The open dots are the experimental change in reflectivity after the high energy p-h background has been subtracted. The signal has been inverted and offset horizontally for clarity. (D) Probe energy dependence of the Fourier transformed $A_{1g} + B_{2g}$ fluctuation.

Solving the pseudospin equation of motion for a time-dependent impulsive potential applied at $t = 0$, $v_{\mathbf{k}}^{X}(t) = E\tau f_{\mathbf{k}}^{X} \delta(t)$, one obtains

$$
\begin{aligned}
\delta\sigma_{\mathbf{k}}^{y} &= 2\cos(\omega_{CF}) \frac{\Delta_{\mathbf{k}}}{E_{\mathbf{k}}} E\tau f_{\mathbf{k}}^{X}, \\
\delta\sigma_{\mathbf{k}}^{\perp} &= -2\sin(\omega_{CF}) \frac{\Delta_{\mathbf{k}}}{E_{\mathbf{k}}} E\tau f_{\mathbf{k}}^{X},
\end{aligned}
\tag{4.11}
$$

implying that after the passage of the pump pulse the pseudospins precess around the equilib-
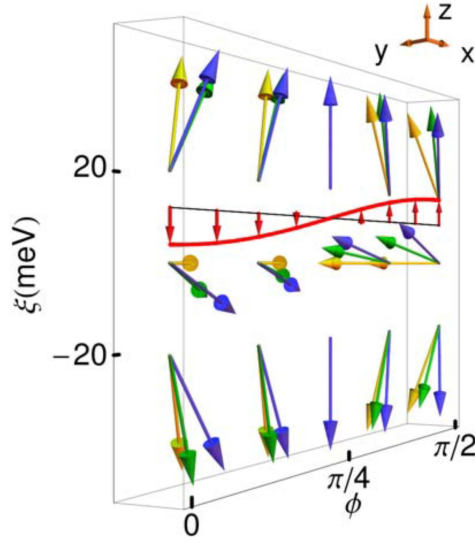
Figure 4.6 – *Adapted from [Mansart et al., 2013, SI].* Snapshots of the textures coding the BCS wave function in momentum space. Small red arrows: amplitude of the impulsive field $\delta\mathbf{b_k}$ applied at $t = 0$ in B_{1g} symmetry. Long arrows: texture snapshots (amplitudes exaggerated for clarity) immediately after the excitation (yellow), at 25 fs (green) and at 50 fs (blue).

rium direction with an angular frequency

$$\omega_{CF} = \left(\frac{2}{\hbar} E_{\boldsymbol{k}}\right) = \left(\frac{2}{\hbar} \left|\mathbf{b_k^0}\right|\right) \overset{(4.9)}{=} \left(\frac{2}{\hbar} \sqrt{\xi_\mathbf{k}^2 + \Delta_\mathbf{k}^2}\right), \tag{4.12}$$

$E_{\boldsymbol{k}} = |\mathbf{b_k^0}| = \sqrt{\xi_\mathbf{k}^2 + \Delta_\mathbf{k}^2}$ being the BCS quasiparticle energy. The precession of the pseudospin texture is depicted in Figs. 4.5 (B) and 4.6 for B_{2g} and B_{1g} symmetry, respectively. It is noteworthy that Eq. (4.10) is close to the equation of motion used in NMR/ESR formalisms [Slichter, 1996]. However, in NMR the static field $\mathbf{b}^0$ is provided by an external field, whereas here it is due to the interaction with the other pseudospins. The magnetic analogy is actually more complete with ESR in magnetically ordered materials where $\mathbf{b}^0$ can be viewed as completely due to the interaction with the other spins.

The most important advantage of CCFS over other spectroscopies on superconductors is its specificity. Since $\delta\mathbf{b_k}$ points in the z direction, only those pseudospins that have a significant equilibrium component in the x-y plane respond to the impulsive Raman field. This automatically selects the quasiparticles participating in the pairing, whereas unpaired electrons are not affected. The excitation is further constrained by the momentum-dependent form factors in $\nu_\mathbf{k}^X(t)$, as defined in Eqs. (4.2) and (4.3). Therefore, in B_{2g} symmetry only those pseudospins that are close to the Fermi level and are neither in the nodes nor in the antinodes display significant dynamics.

To further compare the theoretical coherent charge fluctuation to the experiment, it is nec-

essary to calculate its time-dependent component in the z direction. According to Eqs. (4.2) and (4.7),

$$\langle N_X \rangle(t) = 2 \sum_{\mathbf{k}} \sin(\omega_{CF}) \left(\frac{f_{\mathbf{k}}^X \Delta_{\mathbf{k}}}{E_{\mathbf{k}}} \right)^2 E\tau, \qquad t > 0. \tag{4.13}$$

The sum runs over all the Brillouin zone. The squared factor on the right-hand side of Eq. (4.13) contains the mentioned selectivity of the excitation. To compare the theory to the experimental results, Eq. (4.13) has been evaluated numerically using a d-wave gap function $\Delta_{\mathbf{k}} = \Delta_0[\cos(k_x a) - \cos(k_y a)]/2$ with gap energy $\Delta_0 = 20$ meV and a one-band parametrization of the electronic structure of LaSCO given in literature [Yoshida et al., 2006]. The result for B_{2g} symmetry is shown in Fig. 4.5 (C), together with the experimental charge fluctuations visible in B_{2g} geometry, taken from Fig. 4.3 (E). Note that the experimental data have been inverted and offset horizontally for comparison, and that the theoretical response was calculated for a δ-like excitation. The time-dependence of the charge fluctuation is linked to the dynamics of the pseudospin texture in Fig. 4.5 (B). At $t = 50$ fs (blue), corresponding to the first peak in the charge fluctuation, the pseudospins at $\xi = 0$ and close to $\phi = \pi/4 \pm \pi/8$ are close to their maximum negative amplitude in the z direction. There is a very good agreement between calculations and experiment; in particular, the oscillation frequency, which corresponds to the gap amplitude close to the nodal direction, is identical. Interestingly, the experiment shows a quite long coherence time compared to theory.

In direct analogy to Eq.(2.13), the transient optical properties of the system in the presence of a fluctuation of symmetry X are governed by the changes in the dielectric function tensor

$$\delta \boldsymbol{\epsilon}(\omega, t) = -4\pi \sum_X \frac{\partial \boldsymbol{\chi}}{\partial \langle N_X \rangle}(\omega) \langle N_X \rangle(t), \tag{4.14}$$

where $\partial \boldsymbol{\chi}/\partial \langle N_X \rangle$ is the conventional Raman tensor for electronic scattering from Eq.(4.5). Again, as in conventional phonon ISRS, the same Raman tensor appears in the generation of the pulse and in the subsequent probing process. In analogy with lattice ISRS, only excitations having an interaction matrix element with the fluctuating quasiparticles will contribute to $\partial \boldsymbol{\chi}/\langle N_X \rangle$, allowing to identify the excitations participating in the pairing. It should be pointed out that CCFS is not restricted to reflectivity measurements, and other techniques like time-resolved Raman scattering [Saichu et al., 2009] can be used as a probe. This allows for better control of the excitation symmetry, in particular for the measurement of off-diagonal elements of the Raman tensor that are difficult to isolate using ISRS.

As a final result, the coupling behavior of the coherent charge fluctuation is examined. The oscillation of the superconducting condensate is most clearly visible in the $A_{1g} + B_{2g}$ configuration. For this reason, a Fourier transform analysis is performed in this configuration. The probe-energy dependence of the $A_{1g} + B_{2g}$ fluctuation in the frequency domain is presented in Fig. 4.5 (D). The superconducting fluctuations clearly resonate at an energy of 2.6 eV, corresponding to remnant of the Cu-O charge transfer energy of the parent compound

which coincides with the (renormalized) Hubbard energy U in a one-band description [Anderson, 2007]. Remarkably, even though there is substantial absorption below the charge transfer band in the samples, the superconducting quasiparticles appear to be decoupled from the excitations in that energy region. This is fully consistent with the finding above that the $A_{1g} + B_{2g}$ fluctuations have a sine waveform when pumped at 1.55 eV, indicating non-resonant excitation.

A few remarks should be made about the incoherent background due to p-h excitations created by dipole-allowed excitations of the pump pulse. Within a mean-field picture, the permittivity $\boldsymbol{\sigma}$ (or susceptibility $\boldsymbol{\chi}$) of the sample can change due to the change of the initial state and final state occupation as well as the modification of the electronic structure caused by the out-of-equilibrium distribution. Since the optical properties of LaSCO in the visible range are dominated by the remnant of the CT feature around 2.6 eV, it is reasonable to assume that the main effect of the p-h excitations is to change the balance between the Cu (n_d) and O (n_p) hole occupation numbers. This will offset the CT hole density $n_{CT} \equiv 2n_p - n_d$. To take into account Cu $d_{x^2-y^2}$ and O $p_{x,y}$ orbitals, the system is described by a three-band Hubbard model [Lorenzana et al., 2013], as given in Eq. (2.18):

$$H = \sum_i \epsilon_i \hat{n}_i + \sum_{\substack{<ij>\\\sigma}} t_{ij}(C_{i\sigma}^\dagger C_{j\sigma} + h.c.) + \sum_i U_i \hat{n}_{i\uparrow}\hat{n}_{i\downarrow} + \sum_{<ij>} U_{ij}\hat{n}_i\hat{n}_j. \tag{4.15}$$

Here, $C_{i\sigma}^\dagger$ and $C_{i\sigma}$ are creation and annihilation operators for holes[3] on lattice site i with spin σ and the occupation number operators are defined as $\hat{n}_{i\sigma} = C_{i\sigma}^\dagger C_{i\sigma}$ with $\hat{n}_i = \hat{n}_{i\uparrow} + \hat{n}_{i\downarrow}$. The on-site energies are $\epsilon_i = \epsilon_p$ (ϵ_d) and the on-site repulsions are $U_i = U_p$ (U_d) for i in an O (Cu) site. The nearest-neighbor hopping matrix elements are $t_{ij} = \pm t_{pd}(\pm t_{pp})$ for Cu-O (O-O), with the sign depending on the relative phase of the Wannier orbitals involved. For the inter-site Coulomb repulsion, only the nearest-neighbor term $U_{ij} = U_{pd}$ between Cu and O is included. As mentioned in chapter 2.5, the CT gap is given by $\Delta \equiv \epsilon_p - \epsilon_d$. The parameters are taken from first principle calculations [Lorenzana and Seibold, 2003], except for $\Delta = 3$ eV. This ensures that the first maximum in the CT band in the optical conductivity of the parent compound is at 2.16 eV, in good agreement with static optics [Uchida et al., 1991]. To account for the strong correlations of the Cu electrons, the d orbital is treated using the Gutzwiller approximation, while the using the Hartree-Fock approximation for the other interactions . This leads to a single-particle Hamiltonian with renormalized energies, which at equilibrium depend self-consistently on the charge distribution. The strategy is to compute the optical conductivity at mean-field level in the ground state and in the presence of the out-of-equilibrium charge distribution. For simplicity, any asymmetry of this out-of-equilibrium distribution is neglected in the calculations; it is assumed that the out-of-equilibrium distribution has A_{1g} symmetry.

The primary effect of the out-of-equilibrium charge distribution is the renormalization of the effective energies at mean-field level. Since this effect depends on the total charge, i.e. the integral over the charge distribution, it will be rather insensitive to the actual shape of

---

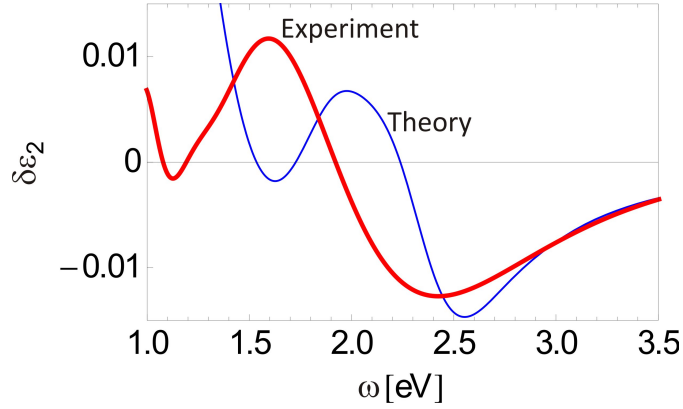[3]Note that electron creation operators are denoted by small letters.

Figure 4.7 – *Adapted from [Mansart et al., 2013, SI].* Comparison between the experimental (red thick line) and theoretical (blue thin line) transient imaginary part of the in-plane component of the dielectric function tensor ε_2 at 500 fs time delay for doping $x = 0.15$. For the theory, $\delta n_{CT}(500 fs) = 8 \cdot 10^{-3}$ is used, as well as three band parameters as specified in the text.

the charge density. In the model, the charge is put out-of-equilibrium by adding a constraint implemented through a Lagrange multiplier. Thereafter, the permittivity $\boldsymbol{\varepsilon}$ and susceptibility $\boldsymbol{\chi}$ are obtained at mean-field level, and the derivative with respect to the out-of-equilibrium charge is evaluated numerically. For the doped case, the ground-state is assumed to consist of stripes [Lorenzana and Seibold, 2003], which gives a good overall agreement with experiments for the optical conductivity.

Figure 4.7 shows the result of the computation for the imaginary part ε_2 of the in-plane dielectric function that was obtained as

$$\delta\boldsymbol{\varepsilon}_{xx}(\omega, t) = -4\pi \frac{\partial \chi_{xx}}{\partial n_{CT}}(\omega)\delta n_{CT}(t),$$

in analogy to Eqs. (2.13) and (4.14). Here, the time-dependent change of the CT hole density is $\delta n_{CT}(t) = n_{CT}(t) - n_{CT}^0$, n_{CT}^0 being the equilibrium CT density. This value is the only free parameter in the model, and is adjusted to $\delta n_{CT}(t = 500\ \text{fs}) = 8 \cdot 10^{-3}$ to fit the intensity of the experimental curve. This value gives the estimate of the number of transferred holes per Cu mentioned above in the discussion of the results. Considering this, together with the simplifications in the computation, a fair overall agreement with the experiment is obtained, where the shape is reproduced correctly, while the absolute energy values are off by about 300 meV.

The number of excited electrons per unit cell can be estimated independently from experimental parameters using the formula

$$n = 2AV \frac{\mathscr{F}}{l_s^2 \Delta E} \int_0^{l_s} e^{-z/l_s} dz,$$

where A is the absorption coefficient and l_s the penetration depth, both at the pumping wavelength, V the unit cell volume, $\mathscr{F}$ the pump fluence in J/m^2 and ΔE the transition energy. For a fluence $\mathscr{F} = 300\ \mu J/cm^2$, a value of $n = 4 \cdot 10^{-3}$ per Cu atom is obtained, in fair agreement with the theoretical calculation of excited electrons δn_{CT}. $\delta n_{CT}(t)$ is positive, which is consistent with the fact that in the ground state there are far more holes on Cu atoms than on O atoms, so the laser pulse will tend to decrease n_d and increase n_p. The transient dielectric function has a strong energy dependence due to transfer of spectral weight among the different absorption bands, which leads to regions of positive and negative transient reflectivity as shown in the spectra in Fig. 4.3. The profile of ϵ_2 can be understood as being caused by a softening of the CT edge due to a downward renormalization of the mean-field charge transfer energy $\langle \Delta \rangle$. The primary effect is due to the nearest neighbor repulsion $\langle \delta \Delta \rangle \sim -2U_{pd}\delta n_{CT}$. The structures appear at higher energy than in the experiment, probably because the mean-field approach underestimates the softening of the CT edge with doping. The same model approach can be used to compute the electronic Raman tensors involved in the ISRS mechanism, which will be discussed in detail in the treatment of the undoped parent compound in chapter 4.3.

Concluding the discussion are a few remarks on how to class the experiments on LaSCO with respect to other studies of cuprate superconductors. In light of the discussion whether or not there is a low-energy glue in high-T_C superconductors [Anderson, 2007], the results presented here constitute an important piece of the puzzle. In particular, the Fourier transform analysis of the charge fluctuation in Fig. 4.5 (D) is consistent with a coupling of the superconducting quasiparticles to excitations at 2.6 eV, in the manner of a clearly defined resonance. By following the inversion argument that a strong coupling of the excited SC condensate to certain excitations means that the latter play an important role in the formation of the condensate, it can be stated that the superconducting state exhibits a clear fingerprint of "Mottness". Of course, other electronic transitions like a d–d exciton can not be excluded. Systematic studies of this type of oscillations in different chemical compositions and energy ranges coupled to further theoretical work will allow deeper insights in the pair-mediating or pair-breaking nature of these excitations. Also, a negligible coupling in the rest of the measured energy window (1.6 eV < $\hbar\omega$ < 3.2 eV) is observed, and it cannot be excluded that other electronic excitations outside the probing range are also coupled to superconductivity, and are maybe even dominant. Numerical computations support a coupling to the Mott scale [Maier et al., 2008], although with a strong contribution from the low energy region.

The key feature of the isotope effect [Maxwell, 1950, Reynolds et al., 1950] in conventional superconductors was its high specificity, since only the frequency of one potential glue excitation was affected and its impact on superconductivity evaluated. CCFS has a high degree of specificity in a reverse form: Only paired electrons are affected, and their impact on different excitations assessed. Compared to previous ultrafast studies of superconductivity, the CCFS experiments provide a direct observable of the coherent Cooper pair dynamics. Moreover, because of the spectroscopic nature of the probing scheme, resonances between superconductivity and high-energy excitations can be detected. Also, because the condensate oscillations

are obtained in real time, their phase and its evolution throughout the probe energy range are accessible. The results presented here form a benchmark for time-resolved experiments in cuprates and shed new light on the nature of the pairing interactions. In a more general perspective the NMR/ESR analogy encoded in Eqs. (4.8) and (4.10) allows to borrow concepts like the relaxation times T_1 and T_2^* [Slichter, 1996]. T_2^* is defined by the decay of the charge fluctuations, which is dominated by the inhomogeneity of the pseudomagnetic field in momentum space. Therefore, the CCFS experiment opens appealing perspectives to typical NMR/ESR-like techniques such as coherent control of the superconducting wave-function by a sequence of pulses. These tools can be generally applied to different materials including heavy fermions and iron-based superconductors.

4.3 Undoped Lanthanum Cuprate

This chapter discusses the possibility to extend the CCFS mechanism detailed in chapter 4.2 into a more general tool to study a material's properties. The material presented in this chapter is currently being published as reference [Mann et al., 2015]. The generalization of CCFS, named *Coherent Fluctuation Spectroscopy* (CFS), can be used in any material where a suitable bosonic excitation can be coherently excited. For the case of phonons, a *Coherent Lattice Fluctuation Spectroscopy* (CLFS) is particularly suited to study the interplay of excitations on phononic energy scales (typically few tens of meV) and the Mott scale ($\sim$ eV). The principle is demonstrated in the undoped parent compound lanthanum cuprate (La_2CuO_4, or LCO), where it is shown that it is possible to compute an absolute Raman matrix element from a set of time-resolved reflectivity data [Mann et al., 2015]. Similar experiments have been performed in simple semiconductors [Roeser et al., 2003, Kudryashov et al., 2007], whose properties are well-studied, and the ISRS mechanism was found suitable to explain experimental results. In this chapter, it is demonstrated that CLFS allows to obtain reliable values for matrix elements in the much more complicated case of strongly correlated materials, where even complex models as those discussed in chapter 2.5 are either lacking, or capture only a limited number of the material's properties.

Undoped LCO is an antiferromagnetic insulator with a maximum Néel temperature $T_N = 320$ K. It is possible to coherently excite a breathing mode along the material's c-axis and study its effect on the in-plane charge-transfer (CT) peak around 2.1 eV, making it a good candidate to test the reliability of the extracted Raman matrix element. For the experiment, a rod of undoped LCO taken from the same batch as the LaSCO crystal in chapter 4.2 was oriented in a Laue diffractometer, cut along a plane containing the *a*- and *c*-axis and polished to optical quality. The Néel temperature was determined to be $T_N = 260$ K, which corresponds to a doping hole content of $6 \cdot 10^{-3}$ or an oxygen content of $\delta = 3 \cdot 10^{-3}$ according to literature data [Kastner et al., 1998].

The polished surface's optical properties were measured by spectroscopic ellipsometry in the lab of Prof. Dirk van der Marel at the University of Geneva. Static data between 0.5 eV
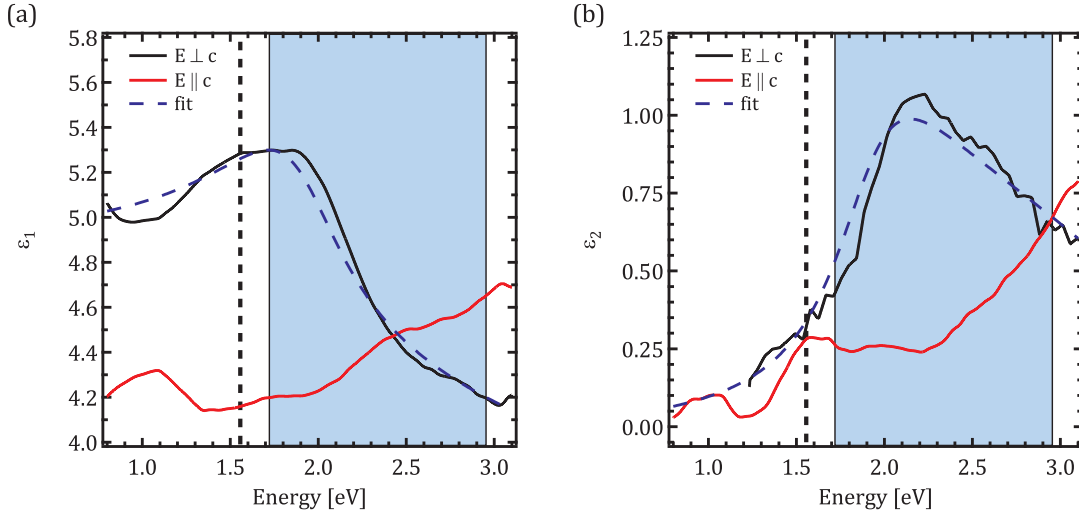
(a)

(b)

Figure 4.8 – *Adapted from [Mann et al., 2015].* (a) Real part and (b) imaginary part of the (pseudo-) dielectric function ε from spectroscopic ellipsometry measurements. The vertical line indicates the pump energy, the shaded area denotes the probe spectrum. The dashed blue lines are fits to the data with the interacting polaron model discussed in the text.

and 4 eV with a resolution of 40 meV were obtained at room temperature in a fixed polarizer geometry (cf. chapter 3.2) for 70° and 75° angles of incidence. Figure 4.8 shows the real and imaginary parts of the dielectric function ε of the LCO sample calculated from the ellipsometry data, revealing the strong optical anisotropy of the material.[4] The in-plane imaginary part ε_2 of the dielectric function is dominated by the oxygen $2p$ to copper $3d_{x^2-y^2}$ CT around 2.15 eV. Although not strictly of excitonic nature, Falck *et al.* have described the CT excitation as creating strongly interacting electrons and holes because of the reduced width of the CT peak [Falck et al., 1992]. The finite width of the peak and its shoulder around 1.6 eV reveal the presence of excess oxygen in the sample, the actual composition being $La_2CuO_{4+\delta}$. Comparing ε_2 to static data from literature [Uchida et al., 1991], it is found that the LCO sample has an effective doping of less than a percent, consistent with the Néel temperature estimate. In contrast to the in-plane behavior, ε_2 is rather featureless along the c-axis. As expected, the sample is not a good conductor in this direction. A small feature is visible at the energy of the pump beam, but this might be an artifact of the ellipsometry measurements. There are no specific transitions assigned to the c-axis spectrum at the pump energy, although the in-plane shoulder present at the same energy can be attributed to a *d–d* transition producing trapped carriers [Ellis et al., 2008]. However, it is a general feature of cuprate superconductors that excitation along the c-axis is an effective way of exciting phonons due to enhanced electron-phonon coupling in this configuration [Reedyk and Timusk, 1992]. In the following, it is presumed that the absorption at the pump energy can be neglected in the analysis of the coherent phonon appearing in the time-resolved experiments. At this point, this assumption

---

[4]Note that technically the figure shows a pseudo-dielectric function [Kuzmenko, 2014, ch. 4.7.3.], since the sample is anisotropic.
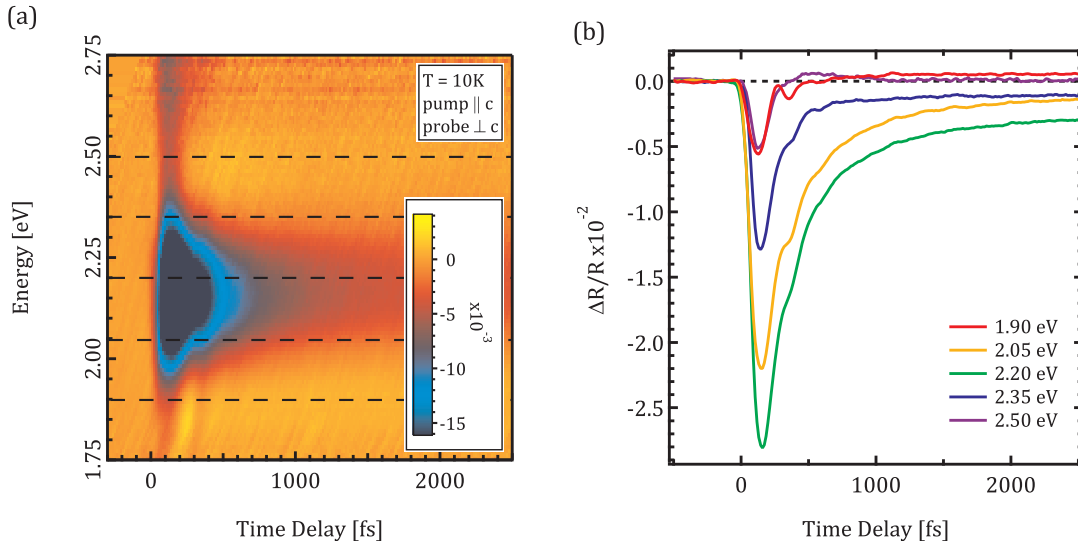
Figure 4.9 – *Adapted from [Mann et al., 2015]*. (a) In-plane reflectivity change of $La_2CuO_{4+\delta}$, shown in color-coding. (b) Time-dependent reflectivity change for selected probe energies. Traces are integrated over 0.15 eV wide slices centered on the horizontal lines in panel (a). The pump light is polarized parallel to the c-axis.

is only a working hypothesis, but it is confirmed a posteriori by the successful description of the data.

Time-resolved reflectivity measurements as described in chapter 3.3 were performed at 1.55 eV pump energy and a fluence of 7.8 mJ/cm^2 at a temperature of 10 K. The sample was excited along the c-axis while the in-plane response was measured. The sample response is shown in Fig. 4.13. The dominant feature is a strong negative peak around 2.15 eV probe energy that decays within ~ 0.5 ps, very similar to the dynamics observed by Novelli et al. [Novelli et al., 2014] in a comparable experiment. The energy maximum coincides with the maximum of ε_2 in Fig. 4.8 (b), but the line shape is much narrower, indicating that the CT feature is indeed superimposed by the shoulder-like feature around 1.6 eV unrelated to the CT. The incoherent part of the response is caused by the blocking of excitations across the CT peak due to the depletion of the initial state (population of the final state) by excitations along the c-axis to (from) the intragap states observed in the static data. The incoherent peak stretches into a short-lived tail towards higher probe energies (figure top), whereas towards lower energies two vertical lines indicate the presence of a coherent excitation. This excitation is the coherent La A_{1g} breathing mode. It is present over the whole probe spectrum, as can be seen from the time traces for fixed probe energy in Fig. 4.9 (b). The same phonon contribution was also observed at room temperature, but the reduced coherence makes the analysis more difficult in that case. The analysis is therefore carried out for the low-temperature data.

Since the oscillation amplitude is rather low compared to the noise level, the data are analyzed using SVD as described in chapter 3.4. The oscillation is present in the first two canonical
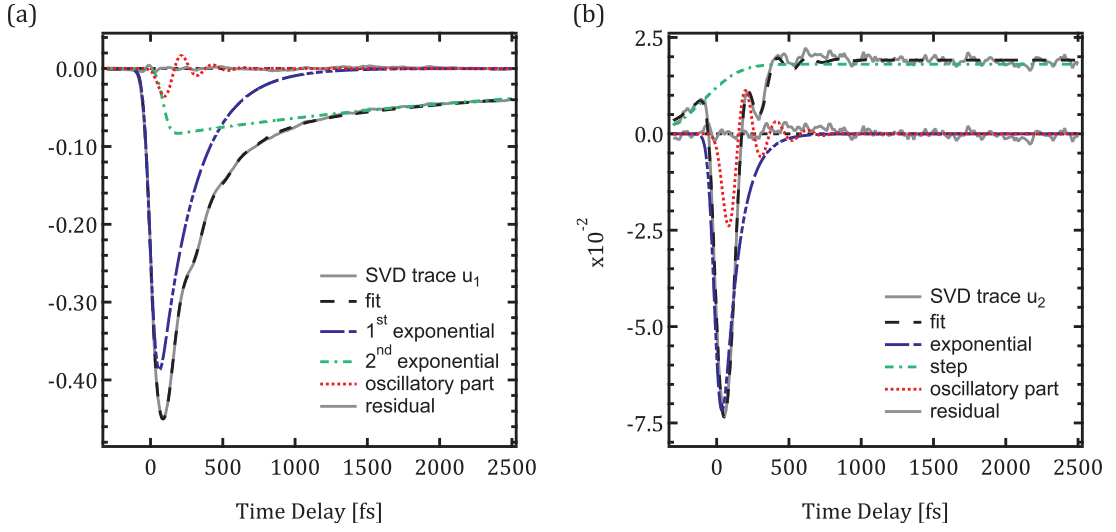
Figure 4.10 – *Adapted from [Mann et al., 2015].* Canonical time traces (a) $u_1(t)$ and (b) $u_2(t)$ obtained from the singular value decomposition. The traces have been fitted with as described in the text.

traces $u_1(t)$ and $u_2(t)$, so the SVD reconstruction is performed up to second rank. The first two canonical time traces $u_1(t)$ and $u_2(t)$ are shown in Fig. 4.10. Following the discussion in chapters 2.2 and 2.3, the traces are decomposed into contributions from incoherent charge relaxations and from the phonon oscillation, and are fitted accordingly. The background is modeled by two exponential decays for u_1 and an exponential decay and a step function for u_2, with a damped oscillation for both traces. The undamped eigenfrequency of the oscillation is about 4.8 THz for both traces. The fit results are used to transform the canonical traces $u_i(t)$, $v_i(E)$ into physical traces $U_i(t)$, $V_i(E)$ according to Eq. (3.7). The physical traces are shown in Fig. 4.11. The relaxation is contained in U_1 to U_4, whereas the oscillation is given by U_5. The energy dependence of the oscillation is contained in the trace V_5 in Fig. 4.11 (b). Note that the oscillatory contribution in the trace U_5 follows a damped sine function, as expected for an ISRS excitation mechanism (cf. chapter 2.3), even though the phase of the oscillation was left as an independent fit parameter.

The physical traces are used to separate the oscillation from the incoherent background, yielding the decomposition

$$\left(\frac{\Delta R}{R}\right)(t, E) = \left(\frac{\Delta R}{R}\right)^{\text{rel}}(t, E) + \left(\frac{\Delta R}{R}\right)^{\text{osc}}(t, E). \tag{4.16}$$

The reconstruction of the data from the SVD for $N_c = 2$ and its separation into relaxation and oscillatory components is shown in Fig. 4.12. The main features of the data are reconstructed even when limiting the SVD to second rank. The reconstructed damped oscillation at a fixed probe energy is shown in Fig. 4.13 (a). The natural frequency is $\omega_{ph} = 4.8$ THz, while the decay time is $\tau = 170$ fs, leading to a resonance frequency of 4.6 THz observed in the spectrum. The
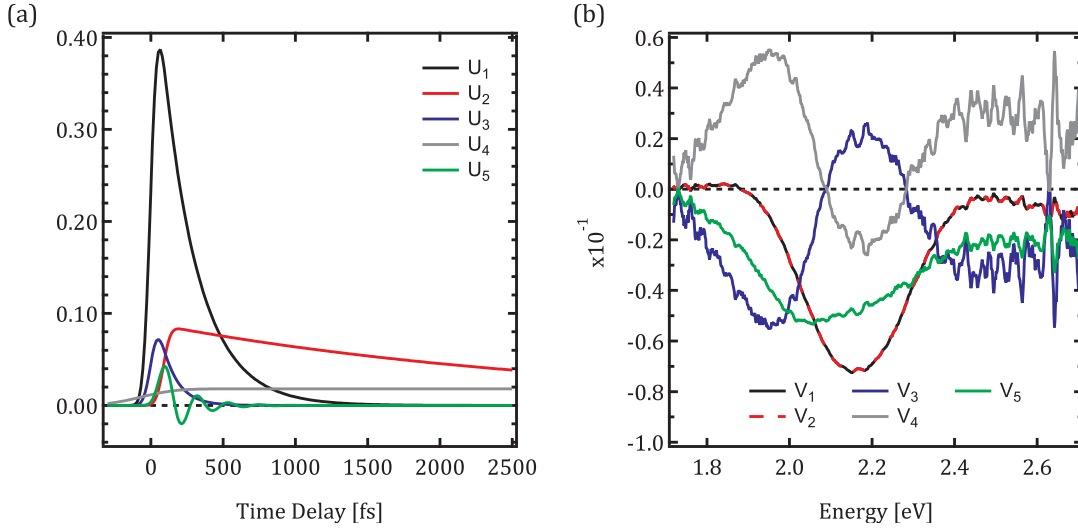
(a)

(b)

Figure 4.11 – *Adapted from [Mann et al., 2015].* (a),(b) Physical traces $U_i(t)$, $V_i(E)$ extracted from the singular value decomposition. The relaxation of the incoherent background is included in U_1 to U_4, while the oscillation is represented by U_5. The energy vectors V_i have been smoothed using a sliding average.

mode corresponds to a well-known A_{1g} phonon mode at 156 cm^{-1} present in static Raman data for the orthorhombic phase of LCO [Sugai, 1989]. Compared to the simpler and more commonly used method of directly using a FFT on the traces of Fig. 4.9 (b), the SVD is a lot more effective in subtracting the incoherent peak, reduces the noise level, and delivers the energy dependence of the oscillation with ease.

The treatment of the data in the scope of this chapter also requires knowledge of the eigenvector of the excited phonon phonon. Since there is no way of reliably extracting it from an optical experiment, one has to rely on calculations. The most reasonable approach to identify a phonon eigenvector is to use a computational model yielding phonon dispersion data that match the dispersion as measured by inelastic neutron scattering [Pintschovius and Braden, 1999]. Such a model, based on DFT+LDA, has been presented in literature [Falter and Schnetgöke, 2002], but calculations were performed in the tetragonal phase, and one has to consider the folding of the Brillouin zone when crossing the transition to the orthorhombic phase. Previous computations (Table V in [Mostoller et al., 1990]) show that the detected phonon mode, listed as 148 cm^{-1} at the Γ point in the orthorhombic phase, corresponds to an A_g mode of 135 cm^{-1} (4 THz) at the X point in the tetragonal phase of LCO. The eigenvector of the latter was calculated by DFT+LDA [Falter and Schnetgöke, 2002, Fig. 7], and is illustrated in Fig. 4.13 (b): It is a breathing mode of the La atoms along the c-axis, where the apical O atoms move in phase with the La atoms.[5] The minimal displacements of the in-plane O atoms indicated in the calculations will be neglected in the discussion. Even if the displacement of

---

[5]This mode thus differs from the coherently excited A_{1g} phonon in La$_{2-x}$Sr$_x$CuO$_4$ in chapter 4.2, in which the La and apical O atoms are breathing in antiphase.
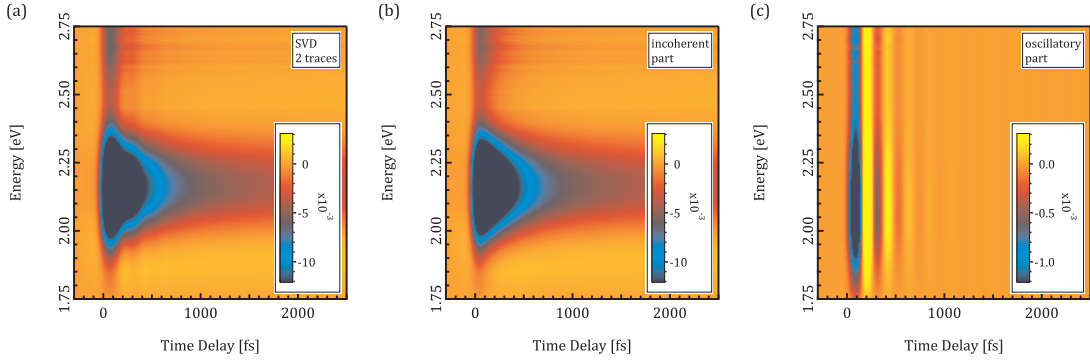
Figure 4.12 – *Adapted from [Mann et al., 2015].* Reconstruction of the data using the SVD results up to second rank: (a) Reconstructed data, compare to Fig. 4.9 (a). (b), (c) Relaxation and oscillatory contributions according to Eq. (4.16).

the O atom was of the same size as that of the La atom, the resulting correction would only change the result by about 10% because the O mass is much smaller than the La mass.

The energy profile of the oscillation extracted from the SVD is shown in Fig. 4.14 (a). It shows a resonance around 2.1 eV, which matches the CT feature seen in the static data in Fig. 4.8 (b). The energy profile for the same oscillation observed with the pump polarized in-plane is also shown. Due to the lower oscillation-to-background ratio, it can only be obtained at a few energy values, integrating over a wide energy range for each point. As discussed below, the absolute Raman profile can be obtained when pump and probe have the same polarization. However, the profile shape should only depend on the probe direction, as confirmed by the similarity of the curves for in-plane and out-of-plane excitation in Fig. 4.14 (a). Therefore, the profile for the case of pumping along the c-axis is rescaled to match the intensity of the profile for pumping in-plane. This will allow the full differential reflectivity profile to be obtained as if the pump was polarized in the plane, as seen below. The next step is to find the Raman profile $\Delta\varepsilon(E) \equiv \frac{\partial\varepsilon}{\partial z}(E)z_M$. While in principle this can be extracted from the differential reflectivity profile using KK transformations, it is more convenient to extract the information by fitting the data to a simple model. As a bonus, this allows the Raman profile to be related to the electron-phonon matrix elements.

The following treatment of the data makes use of the discussion of ISRS in chapter 2.3. The force term from Eq. (2.10) is adapted to the situation in LCO by assuming a single ion occupying the volume v_i and moving in a transparent medium, yielding a force $F(t)$ of the form

$$F(t) = v_i \frac{1}{16\pi} \mathscr{E}(t) \cdot \frac{\partial\boldsymbol{\varepsilon}}{\partial z}(E_L) \cdot \mathscr{E}^*(t), \tag{4.17}$$

where z is the ionic coordinate, $\boldsymbol{\varepsilon}$ is the dielectric tensor of LCO, and its derivative is taken at the pump-laser energy $E_L = 1.55$ eV. The quantity $\left|\boldsymbol{e} \cdot \frac{\partial\boldsymbol{\varepsilon}}{\partial z} \cdot \boldsymbol{e}^*\right|^2$ ($\boldsymbol{e}$ being a unit polarization vector) determines the cross section for spontaneous Raman scattering [Cardona and Güntherodt, 1982, Knoll and Ambrosch-Draxl, 1995]. The absolute magnitude has been determined only
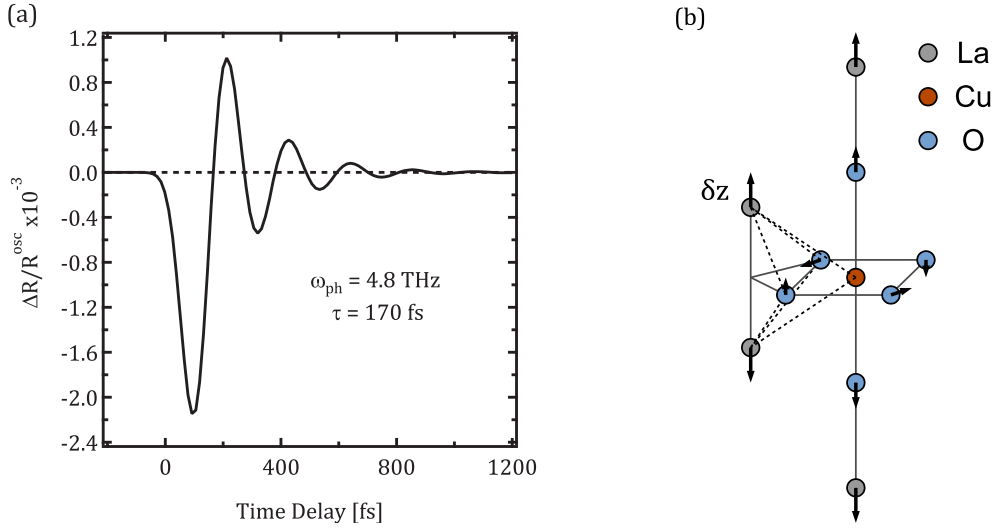
(a)

(b)

Figure 4.13 – *Adapted from [Mann et al., 2015].* (a) Oscillatory contribution $\left(\frac{\Delta R}{R}\right)^{\text{osc}}$ to the transient reflectivity data for E = 2.1 eV. (b) Eigenvector of the La A_{1g} phonon mode identified as the oscillation in the data, after [Falter and Schnetgöke, 2002]. The displacement δz of the La ion closest to the plane is marked by an arrow, and the shortest distances to the in-plane atoms are indicated by the dashed lines.

in few cases (see e.g. [Heyen et al., 1990]), with very demanding static Raman experiments at multiple laser frequencies. According to Eq. (2.11), the impulsive force from Eq. (4.17) will make the single ion of mass M oscillate at frequency ω_{ph}. The maximum displacement amplitude of the oscillation is given by

$$z_M = \frac{v_i \mathscr{F}}{2\omega_{ph}Mc} \left| \frac{\partial \varepsilon_{pu}}{\partial z}(E_L) \right|, \tag{4.18}$$

with the experimental fluence value $\mathscr{F}$ = 7.8 mJ/cm^2. The dielectric tensor $\varepsilon_{(pu)} = \boldsymbol{e} \cdot \boldsymbol{\varepsilon} \cdot \boldsymbol{e}^*$ in Eqs. (4.17) is projected according to the polarization of the pump. The ion movement produces the oscillatory part of the reflectivity signal in Eq. (4.16),

$$\left(\frac{\Delta R}{R}\right)^{\text{osc}}(t,E) = \frac{\partial \ln\{R\}}{\partial \varepsilon_{pr}} \cdot \frac{\partial \varepsilon_{pr}}{\partial z}(E) \cdot z(t), \tag{4.19}$$

where ε_{pr} is the dielectric tensor projected according to the polarization of the probe.

Now, it is important to consider three things:

1. The resonant Raman profile $\frac{\partial \boldsymbol{\varepsilon}}{\partial z}$ is phonon-specific. Since the same phonon is involved in the excitation and detection, $\frac{\partial \varepsilon_{pu}}{\partial z} = \frac{\partial \varepsilon_{pr}}{\partial z}$ if pump and probe have the same polarization and the material is (nearly) transparent.

2. The prefactor of Eq. (4.18) contains only experimental constants, while the factor $\frac{\partial \ln\{R\}}{\partial \varepsilon_{pr}}$
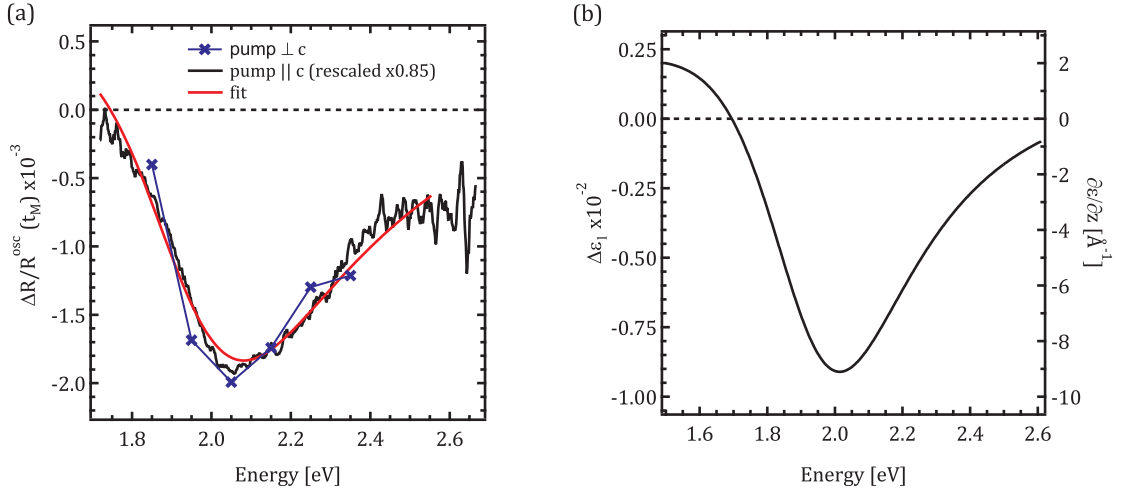
Figure 4.14 – *Adapted from [Mann et al., 2015].* (a) Differential reflectivity energy profile of the coherent oscillation at $t = t_M$ for out-of-plane and in-plane excitation, and fit. (b) Differential dielectric function $\Delta\varepsilon_1$ corresponding to in-plane pump and probe polarizations at $t = t_M$ (left scale). The absolute right scale was obtained as explained in the text.

in Eq. (4.19) is known from Fresnel's formulas.

3. Using $\varepsilon_{pr} = \varepsilon_{pu}$ and evaluating Eq. (4.19) at the time t_M of the maximum amplitude and at the energy E_L of the pump, the ion position $z(t_M) = z_M$ can be eliminated by substituting Eq. (4.18) into Eq. (4.19). Thus, an expression for the squared magnitude of $\frac{\partial\varepsilon_{pu}}{\partial z}(E_L)$ in terms of experimental quantities is obtained. Eq. (4.19) then gives access to the full resonant Raman profile.

This means that the resonant Raman profile $\frac{\partial\varepsilon}{\partial z}(E)$ of any phonon in any material can be directly determined over the probing range of a broadband reflectivity measurement. The procedure works as well if more than one oscillation is present in the data as long the oscillatory contributions according to Eq. (4.16) can be separated for each phonon. Also note that, in general, knowledge of the phonon eigenvector is not required. In practice, relating the reflectivity R to ε requires the use of a Kramers-Kronig (KK) transform or a Drude-Lorentz model, as discussed in chapters 2 and 3.5. However, the aim of this discussion is to test the reliability of extracting matrix elements using CLFS. Therefore, the elements are determined using a dielectric model function based on interacting polarons, similar to the one introduced by the group of Kastner [Falck et al., 1992]. The model dielectric function describes the in-plane CT peak of LCO seen in ε_2 in Fig. 4.8 as being caused by interacting polaron pairs. This is supported by photoconductivity measurements [Falck et al., 1992]. Notice that the rather large peak width of more than 200 meV does not support a description as a completely bound excitonic state, but the description in terms of short-range Frenkel type excitons is a good approximation.

The absorption edge is modeled in terms of transitions between a valence and a conduction

band modified by Coulomb interactions; the short-range interaction potential is approximated as $V(r) = U_{eh}\delta(r)$. For simplicity, the electron-hole interaction strength U_{eh} is taken to be momentum-independent. The permittivity can be written as

$$\varepsilon(\omega) = \varepsilon_\infty + s \cdot \frac{G(\omega)}{1 - U_{eh}G(\omega)}, \tag{4.20}$$

where the denominator contains the enhancement factor due to electron-hole interactions [Mahan, 1990, ch. 4.5]. The oscillator s strength is parametrized as $s = 4\pi e^2 x_{eh}^2 / v_{Cu}$, where x_{eh} is a dipole matrix element between the Wannier orbitals of the two bands and v_{Cu} is the volume per Cu atom. The electron-hole Green's function is defined as

$$G(\omega) \equiv \frac{2}{W} \int\limits_{E_g}^{E_g+W} d\omega' \left(\frac{1}{\omega + \omega' + i\gamma/2} - \frac{1}{\omega - \omega' + i\gamma/2} \right), \tag{4.21}$$

where the two terms ensure the correct symmetry of ε_1 and ε_2. Due to the two-dimensionality of the system, a flat joint density of states $D = 2/W$ confined to a band of width W above the gap energy E_g is assumed. The factor of two in D considers spin degeneracy. The bandwidth W of the absorption band is the sum of the electronic (single-particle) electron and hole bandwidths. The linewidth of the transition is given by half the (two-particle) phenomenological damping γ, which is assumed to have a simple linear dependence on the frequency, $\gamma = a + b \cdot \omega$. Notice that rigorously speaking the model is for a stoichiometric compound, while the LCO sample used in the experiment has a small oxygen surplus. As discussed by Li *et al.* [Li et al., 2013], the small opacity caused by the excess oxygen will introduce an imaginary component into the Raman tensor for the generation of the phonon. However, the doping is so small that its effect can be phenomenologically absorbed in small changes of the damping and other parameters. According to the Born-Oppenheimer approximation (cf. chapter 3.4), it is assumed that the electronic parameters of the model, like the density of states D and gap E_g, depend parametrically on the coherent ionic motion excited by the pump.

The model can be used to simultaneously fit the equilibrium optical response in Fig. 4.8 and the differential reflectivity profile at the maximum of the oscillation at time t_M in Fig. 4.14 (a) with only two parameter changes, $\delta E_g = 6.4$ meV, $\delta D = 4.6 \cdot 10^{-3}$ eV^{-1}. Physically, these are also the parameters expected to be most sensitive to the motion of the La ions. Fig. 4.14 (b) shows the differential dielectric function $\Delta\varepsilon_1$ corresponding to the oscillation amplitude at t_M. Neglecting the absorption part, its value at the pump energy can be represented as $\Delta\varepsilon(E_L) = \frac{\partial\varepsilon}{\partial z}(E_L)z_M = 1.8 \times 10^{-3}$. This equation together with Eq. (4.18) (using for M the mass of one La atom moving in the volume $v_i = v_c/4$, v_c being the orthorhombic unit cell volume) yields a maximum amplitude $z_M = 1.0 \times 10^{-3}$ Å. This value can be used to calculate the absolute Raman profile $\frac{\partial\varepsilon}{\partial z} \equiv \Delta\varepsilon(E)/z_M$, shown in the right scale in Fig. 4.14 (b). The resulting electron-phonon matrix elements are given as $\partial E_g/\partial z \equiv \delta E_g/z_M = 6.4$ eV Å^{-1}, describing the change of the CT gap with the La motion, and $\partial D/\partial z = \delta D/z_M = 4.6$ eV^{-1} Å^{-1}, describing the change in density of states. It is noteworthy that the time-resolved data at 10 K are fitted together

with static data at 300 K. In spite of this discrepancy, the curves in Fig. 4.8 imply that the fit tends to an even lower energy for the CT peak, corresponding to an even higher temperature. A likely explanation for this is given by the very high electronic temperatures that are reached upon laser excitation. This interesting feature deserves further examination. It is theoretically possible to perform a time-dependent version of the matrix element fit, corresponding to a fit at different electronic temperatures. The resonance profile of the oscillation indeed shows a slight time dependence, but the relaxation time is shorter than a phonon period, making such an analysis unfeasible on the current data set. However, this phenomenon could be studied in a system where the damping is smaller than the phonon frequency.

To check if the model estimates are reasonable, they are compared to an estimate from an ionic model in point charge approximation. It is assumed that $\partial E_g/\partial z$ is approximately given by the change of the difference in Madelung energy among planar Cu and O atoms when the La is moved in the z direction. The ionic displacement induced by the coherent phonon along the c-axis will affect the Madelung energies ε_{Cu} and ε_O of the copper and oxygen atoms in the ab-plane, changing the CT energy $\Delta = \varepsilon_{Cu} - \varepsilon_O \equiv E_g$ (cf. Eq. (2.19) and [Carbone et al., 2010]), as well as the density of states $D(\omega)$ in the polaron band W. Considering the effect of the displacement δz of the La atoms closest to the CuO$_4$ plaque on the in-plane CT energy Δ. The atoms in question are the ones sitting above and below the plaque on the positions indicated in Fig. 4.13 (b). The shortest distances to the in-plane atoms are indicated by the dashed lines. The energy Δ is given as a function of the shortest La distance z from the Cu-O plane by

$$\Delta(z) = \frac{Ze^2}{4\pi\varepsilon_0\varepsilon_R} \cdot \left(\frac{+4}{d_{La-Cu}} + \frac{-8}{d_{La-O}} \right) = \frac{Ze^2}{4\pi\varepsilon_0\varepsilon_R} \cdot \left(\frac{4}{\sqrt{\frac{a^2}{2} + z^2}} - \frac{8}{\sqrt{\frac{a^2}{4} + z^2}} \right), \quad (4.22)$$

with the La charge $Z = 3$ and the unit cell length $a = 3.8$ Å, which is equivalent to twice the in-plane Cu-O distance. Note that there are two La atoms closest to each CuO$_4$ plaque which are nearest neighbors to two Cu atoms and four O atoms each and that the Cu and O atoms carry a single charge, yielding the factors four and eight in Eq. (4.22). For the relative dielectric constant ε_R the value $\varepsilon_1(E_{CT}) = 5.3$ at the CT energy (see Fig. 4.8 (a)) is used to account for screening effects. Using the equilibrium distance $z_0 = 1.79$ Å, an el-ph matrix element of $\frac{\partial E_g}{\partial z} \equiv \frac{\partial \Delta}{\partial z} = 4.3$ eV Å^{-1} is obtained, in reasonable agreement with the experimental value. Given the crudeness of the model and the approximations used to determine the matrix element this is quite a good agreement. Notice that in Eq. (4.22) the zero-momentum dielectric function is used, which is certainly an upper limit for the screening at short distances. A more realistic screening will improve the agreement with the experiment.

In conclusion, the experiments show that coherent fluctuation spectroscopy can be used to determine absolute Raman profiles in correlated systems much easier than static Raman scattering. For the specific case of LCO it was also shown that the Raman profile can be described via changes in few electronic key parameters describing the equilibrium optical properties, CT energy and density of states. This allows the microscopic electron-phonon

matrix elements to be estimated in a correlated system, finding agreement with a simple ionic model. As a bonus, it is confirmed that ISRS is the mechanism at work on generating the ionic motions. While similar studies have been performed before [Roeser et al., 2003, Kudryashov et al., 2007], those dealt with semiconductors only. There, the situation is much simpler, because (i) no strong correlations are present, (ii) the materials are well studied, and theoretical models are readily available for comparison, and (iii) the phonon life times are by far longer, simplifying the extraction. No previous works using ultrafast optics exist where it was checked for a strongly correlated system that the amplitude of the oscillations is correctly given by this mechanism, as the analysis of LCO implies. In correlated systems, one potential application of the Raman profile is the manipulation of the electronic ground state by direct excitation of specific phonons, similar to what has been done in recent control experiments [Fausti et al., 2011, Cavalleri et al., 2001, Hilton et al., 2007, Stojchevska et al., 2014, Yusupov et al., 2010]. In the case of Raman excitation, the Raman profile allows to find the excitation energy at which the applied force is maximum, thus allowing to reduce fluence and unwanted heating. For example, Fig. 4.14 (b) together with Eq. (4.17) suggests that by increasing the pump excitation energy the oscillations can be enhanced, although at some point absorption will become important and other mechanisms, not considered here, may enter into play. As discussed in chapter 2.3, the transition from a dominantly impulsive mechanism to a displacive one should show up in the data as a change of the phonon's sine form to a cosine form. The variation of the coherent oscillation's amplitude with pump energy has recently been studied in a similar experiment on an underdoped cuprate for the enhancement of the Josephson plasma resonance [Casandruc et al., 2015]. This is important given that mechanisms other than ISRS have been proposed in the past [Stevens et al., 2002]. Finally, the LCO results pave the way to a systematic investigation of the interplay between charge and/or structural fluctuations and electronic excitations in complex oxides, facilitating research on the topic of competing order in cuprates. For example, an interesting experiment would be a study of the resonant behavior of the oscillation of the superconducting gap observed by CCFS described in chapter 4.2. Such a study would greatly benefit from comparison to numerical values for the electron-phonon coupling, e.g. [Spitaler et al., 2013].

4.4   Slightly underdoped Neodymium Barium Cuprate

The last experiment presented in this chapter is a thorough study of the dynamics of Bogoliubov quasiparticles in an optical experiment. The material of choice is slightly underdoped (UD) neodymium barium cuprate ($NdBa_2Cu_3O_{7-\delta}$, or NBCO). NBCO is a good choice of material to study the slightly underdoped region of the cuprate phase diagram, because it tends to stabilize below optimal doping. In contrast, the structurally identical, widely studied YBCO is more stable at optimal doping. The main advantage of being below optimal doping is the large separation between the superconducting and pseudogap (PG) transition temperatures $T_C = 93$ K and $T^* = 170$ K, as indicated in Fig. 4.1. This allows spectroscopic signatures from the superconducting and pseudogap regions to be separated. This separation occurs although

the doping is still close to optimal, allowing for direct comparison to the optimally-doped (OP) case. As mentioned in chapter 3.3, one of the advantages of broadband time-resolved studies is the abundance of information that is obtained in contrast to single-wavelength experiments. This is underlined by the discussion of the experiments on NBCO, where all important features observed in time-resolved optical measurements on cuprates performed in the last decade can be observed in one single experiment. The most intriguing result, however, is the behavior of the Bogoliubov quasiparticles created by breaking Cooper pairs (cf. chapter 2.4), which are clearly observed well above T_C, far in the PG phase. This is of interest for the discussion of the nature of the latter, and the results strongly favor the scenario of preformed pairs existing in the PG phase. These pairs do not possess phase coherence, and thus cannot condense into a macroscopic state (cf. chapter 2.4). Note, however, that the superconducting fluctuations observed as Bogoliubov quasiparticles are not strictly correlated with the pseudogap transition, so there does not seem to be a direct correlation to the pseudogap. In accordance to the interpretation in terms of preformed pairs, the phonon anomaly of the Ba mode is observed at temperatures much higher than T_C, but below T^*, and the spectroscopic features of the Bogoliubov QPs can be traced in the pseudogap phase. To this end, the temperature dependence of the sample's transient response is studied in detail.

The experiments were performed on a high-quality NBCO single crystal that was grown following the procedure outlined in chapter 3.1. The crystal was flux-grown in an Y-stabilized zirconium crucible under reduced oxygen atmosphere to avoid spurious substitution of the Nd ion onto the Ba site [Schlachter et al., 2000]. The resulting crystal is a parallelepiped with dimensions 5.5 mm × 4 mm × 1 mm along the *a*-, *b*- and *c*-axes, respectively. The sample was annealed in oxygen for ten days at 370° C, resulting in a superconducting transition temperature of $T_c = 93.5$ K, as measured by dc magnetization, and a sharp transition width of 1.5 K. The whole crystal was polished to optical grade on two surfaces, containing the *ab*- and *ac* planes, respectively, using diamond powder paste. For both polished surfaces, static optical data were obtained from the far infrared (FIR) to ultraviolet (UV) regime, 12.5 meV to 6 eV, using broadband ellipsometry. The data were used to calculate the complex optical conductivity of the sample. Anisotropy corrections were performed using standard numerical procedures [Bernhard et al., 2004, Azzam and Bashara, 1977] and diffraction effects were accounted for using an established procedure [Humlíček and Bernhard, 2004]. The FIR data were taken at the infrared beam line of the ANKA synchrotron at the Karlsruhe Institute for Technology in the range from 12.5 meV to 85 meV [Bernhard et al., 2004], using a home-built ellipsometer attached to a Bruker fast-Fourier spectrometer. Overlapping data in the IR to UV range (0.5 eV to 6 eV) were taken at the University of Fribourg using a Woollam VASE ellipsometer. These latter measurements were performed in a vacuum better than 10^{-8} mbar when at cryogenic temperatures, to prevent measurable ice condensation onto the sample. Time-resolved reflectivity data were obtained for the *a-b* surface as described in chapter 3.3. The pump and probe beam were polarized along the crystallographic [110] direction, giving access to the in-plane optical response of the sample, and selecting the $A_{1g} + B_{2g}$ symmetry configuration for Raman processes (cf. Eq. (4.6)).
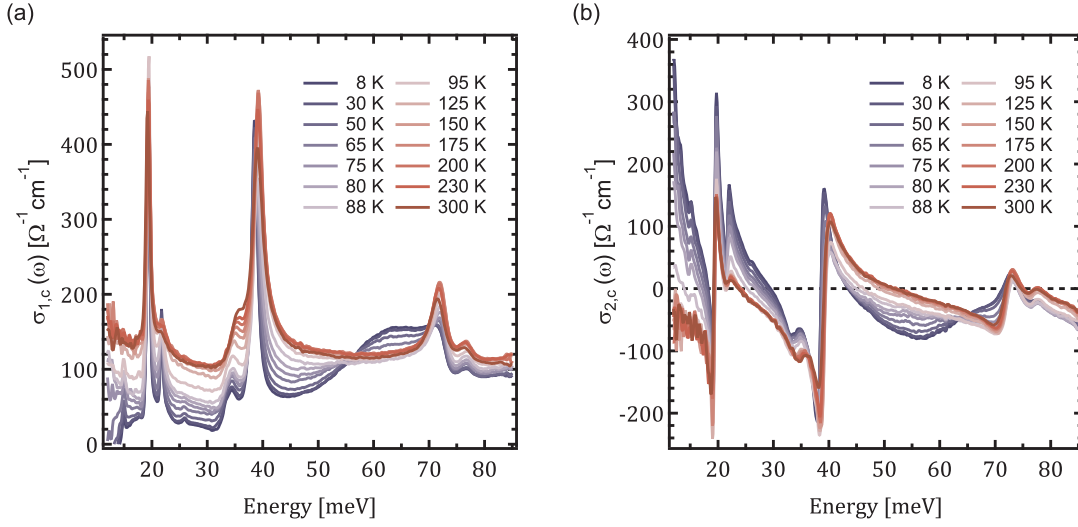
Figure 4.15 – (a) Real and (b) imaginary part of the c-axis optical conductivity $\sigma(\omega) = \sigma_1(\omega) + i\sigma_2(\omega)$ of slightly underdoped NBCO as a function of temperature. Data were taken by B. Mallett of the Universtiy of Fribourg.

In the following, the results of the static ellipsometry measurements that were used to characterize the sample are discussed. The PG and SC gap energy scales can be revealed by temperature-dependent optical spectroscopy. Eq. (2.5) suggests that, in general, the conductivity is sensitive to the opening of the SC gap, and possibly the pseudogap. In cuprates, the c-axis transport is dominated by carriers from the antinodal region of the Fermi surface [Andersen et al., 1995], making the c-axis conductivity particularly sensitive to the opening of the two gaps. Therefore, the pseudogap and superconducting transition temperatures T^* and T_C can be estimated from the temperature dependence of the electronic background in the far-infrared c-axis conductivity [Yu et al., 2008]. Fig. 4.15 shows the real and imaginary parts of the c-axis FIR conductivity σ_c as measured by steady-state ellipsometry. The data were taken by B. Mallett of the University of Fribourg. Following Eq. (2.4), its real part $\sigma_{1,c}$ is integrated in the range from 12.5 meV to 85 meV and traced as a function of temperature. The results are shown in Fig. 4.16. As expected from Eq. (2.5), the SW starts to increase significantly when approaching T_C, roughly following the order parameter. However, its maximum value is not recovered immediately when crossing T_c, but instead a gradual increase develops. This 'missing' SW is a characteristic feature of the presence of the pseudogap in the two-particle excitation spectrum. A detailed study shows that the opening of the pseudogap shifts a portion of the SW above the fixed point present around 55 meV in the temperature dependence of $\sigma_{1,c}$ [Yu et al., 2008]. This can be seen in the data in Fig. 4.15 (a). The point where the SW reaches its saturation value provides an estimate of T^*. According to the data, values of $T_C \approx 94$ K and $T^* \approx 170$ K can be determined for the slightly UD NBCO crystal, as indicated in Fig. 4.16.

The real part $\sigma_{1,ab}$ of the in-plane conductivity of the sample is shown in Fig. 4.17 (a) as a function of temperature. The energy of the pump (dashed line) and of the broadband
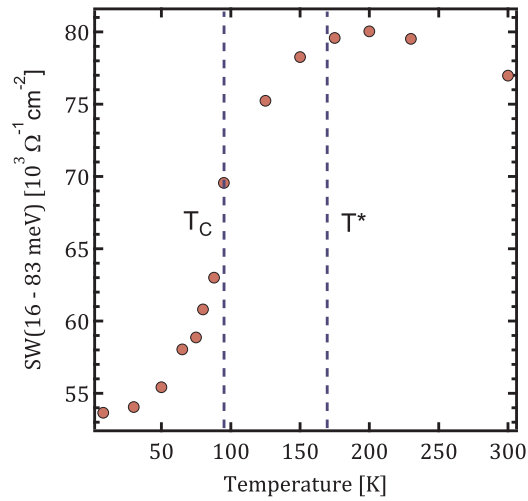
Figure 4.16 – Temperature dependence of the c-axis spectral weight, calculated over the measured FIR spectral range (12.5 - 85 meV). The dashed vertical lines indicate the estimated T_C and T^*.

probe (shaded area) used in the time-resolved experiment are highlighted. The measured response agrees well with previously reported data for the 123 family of cuprates [Cooper et al., 1993, Bäckström et al., 2004]. The low-frequency (< 1 eV) contribution lowers its weight with decreasing temperature, and a first peak is observed around 1.4 eV, closely followed by a weaker satellite at 1.77 eV. The spectral range below 1 eV has been modeled in the past using a Drude-like contribution and a mid-infrared component [Cooper et al., 1993]. The feature at 1.4 eV sharpens when temperature decreases. It has been ascribed to the CT excitation in the CuO_2 planes, since it represents a reminiscence of the fundamental absorption gap visible in the same region of the conductivity in the undoped parent compound, equivalent to the 2.15 eV feature of LCO discussed in chapter 4.3. However, such an attribution of a CT feature should be taken with caution in a strongly doped material, where the notion of an electron transfer between separated p and d orbitals breaks down. A second prominent peak can be observed around 2.6 eV, which progressively loses weight with decreasing temperature. Linear Muffin-Tin Orbital (LMTO) calculations assigned this peak to an interband transition into the antibonding Cu(2)-O(2)-O(3) band, with the initial state being found in a manifold of strongly dispersive bands [Kircher et al., 1991]. This interpretation has been recently refined by *Dynamical Mean Field Theory* (DMFT) calculations, which described it as a charge excitation from the Lower Hubbard Band (LHB) to E_F in OP YBCO [Fausti et al., 2014]. Figure 4.17 (b) shows the partial SW integrated over the region covered by the shaded area (1.72 - 2.88 eV) in panel (a) as a function of temperature. The SW is almost linear as a function of temperature, showing no strong features around T_C and T^* when integrated over the whole probing range, except for a small kink around T_c. Nevertheless, the observation of peculiar effects at T_C taking place in the equilibrium optical spectra at high-energies has been provided by several studies in the past [Bäckström et al., 2004, Rübhausen et al., 2001, Molegraaf et al., 2002, Boris et al.,
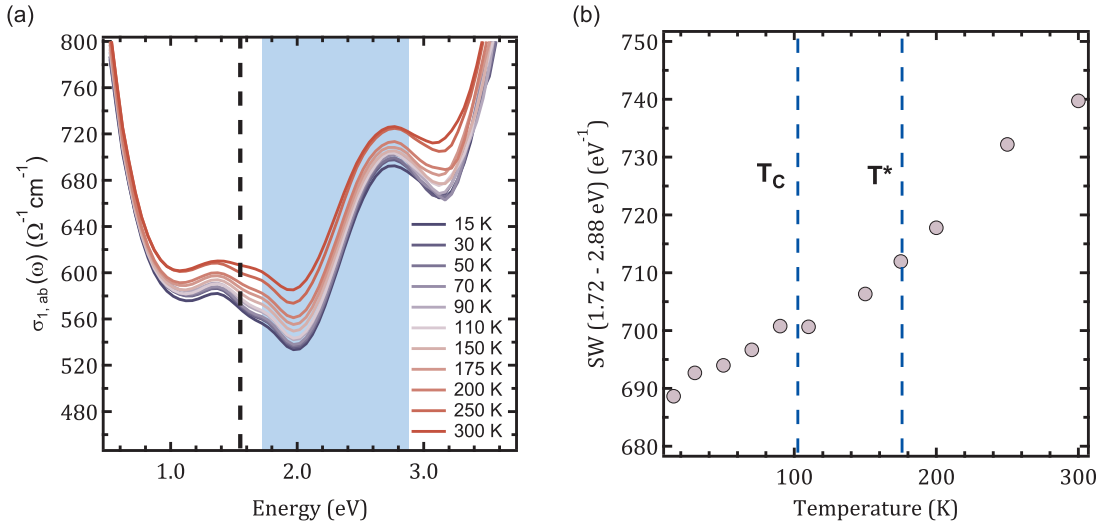
Figure 4.17 – (a) Real part of the in-plane optical conductivity at selected temperatures. The dashed line marks the energy of the pump pulse used in the time-resolved experiment, while the shaded area refers to the spectral range of the probe pulse. (b) Temperature evolution of the spectral weight calculated over the region highlighted by the shaded area (1.72 – 2.88 eV). T_C and T^* are indicated by dashed vertical lines.

2004] and interpreted as a fingerprint of Mottness [Stanescu and Phillips, 2003, Carbone et al., 2006]. It can be estimated from Fig. 4.17 (a) that such features may be traceable when the SW is calculated around the peaks in the optical conductivity, none of which is fully contained in the probed spectrum.

Fig. 4.18 (a) displays the transient reflectivity $\Delta R/R(\tau, E)$ as a function of the probe energy and time delay between pump and probe for a few significant temperature values (10 K, 80 K, 95 K, 110 K, 250 K, 300 K). As mentioned, both pump and probe beams are polarized along the [110] crystallographic direction. The absorbed pump fluence is set around 300 $\mu J/cm^2$, which is still below the threshold for the complete vaporization of the SC condensate, as detailed in the discussion of the fluence dependence towards the end of this chapter. The temporal dynamics of $\Delta R/R$ at selected probe energies (1.73 eV, 2.0 eV and 2.48 eV) are displayed as gray traces in the color maps. The complete temperature dependence for all nineteen measured temperatures is provided for reference in Fig. 4.19. The temperatures are indicated in the labels; the response is shown up to 1 ps. The temporal evolution of the photoexcited sample and its spectral shape in the high-energy region are similar to those of other cuprates [Giannetti et al., 2011, Mansart et al., 2013], with two distinct regions of negative and positive photoinduced changes separated by an isosbestic point whose energy is found to depend on temperature, fluence and material composition.

Figure 4.18 (b) presents the time traces for the 10 K map. The signal around 2.0 eV comprises a small resolution-limited rise, followed by a second, delayed negative contribution that shows the maximum change of the response around 200 fs. Subsequently, a fast (sub-ps) decay of
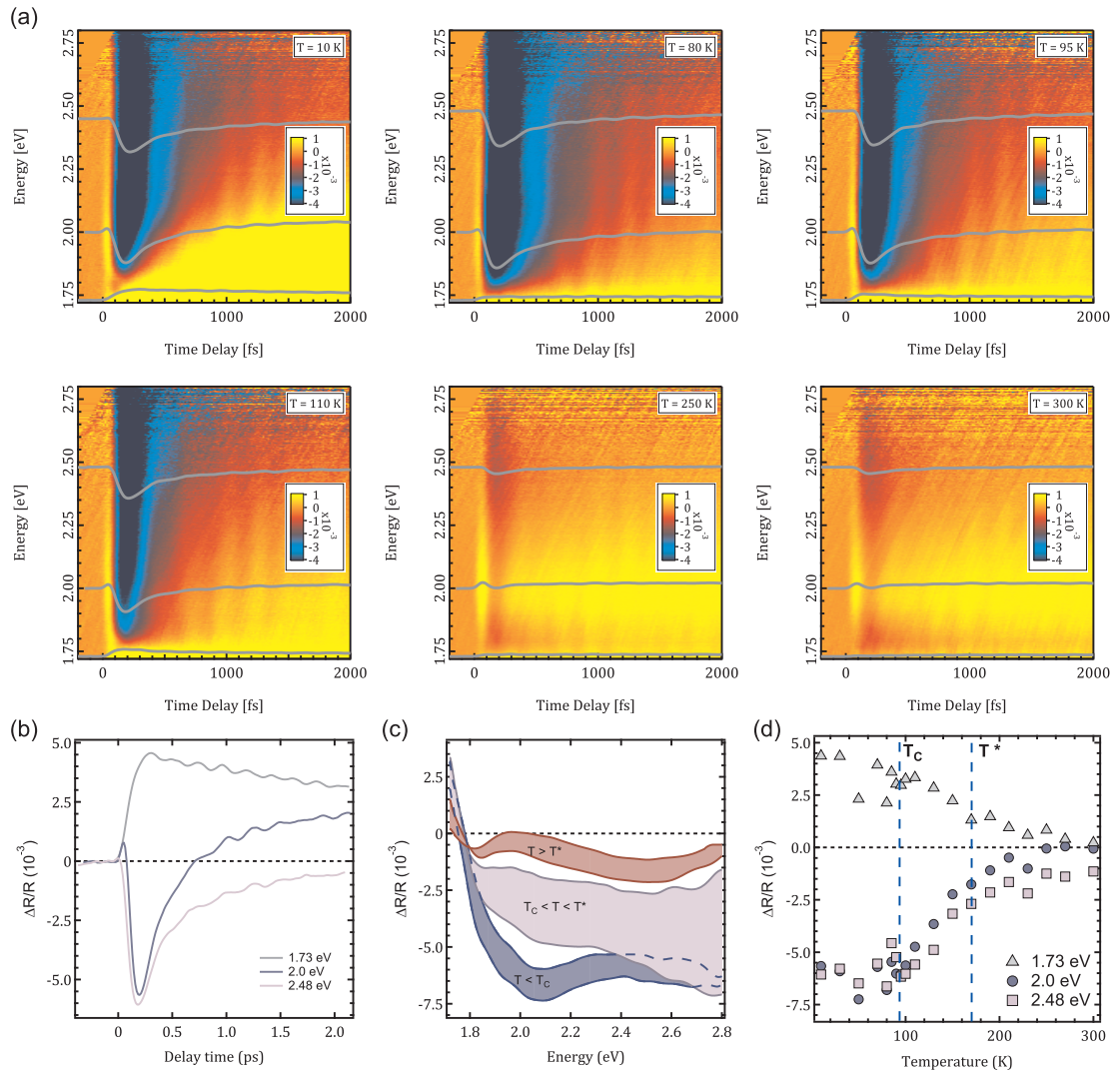
Figure 4.18 – (a) Transient reflectivity $\Delta R/R(\tau, E)$ as a function of probe energy and time delay between pump and probe at various temperatures. The temperatures are indicated in the labels. (b) Temporal traces at 10 K for fixed probe energies of 1.73, 2.0 and 2.48 eV. (c) Transient reflectivity spectrum at a fixed time delay of $t = 200$ fs for the temperatures in panel (a). (d) Temperature evolution of $\Delta R/R$ at $t = 200$ fs for fixed probe energies. T_c and T^* are indicated for reference.

the negative contribution takes place and the signal becomes positive at larger time delays. This pattern characterizes the signal across the whole spectrum, but the weight of the positive component with respect to the negative one is strongly dependent on the probe energy. On the low-energy side of the spectrum (cf. the trace at 1.73 eV), only a positive contribution is visible and the signal approaches a positive constant value as a function of time. On the high-energy side (cf. the trace at 2.48 eV), the positive contribution is hardly present, producing a decrease in the first resolution-limited peak and keeping the signal negative. On top of this incoherent response an oscillation can be seen in the whole spectrum, and can be ascribed to the coherent
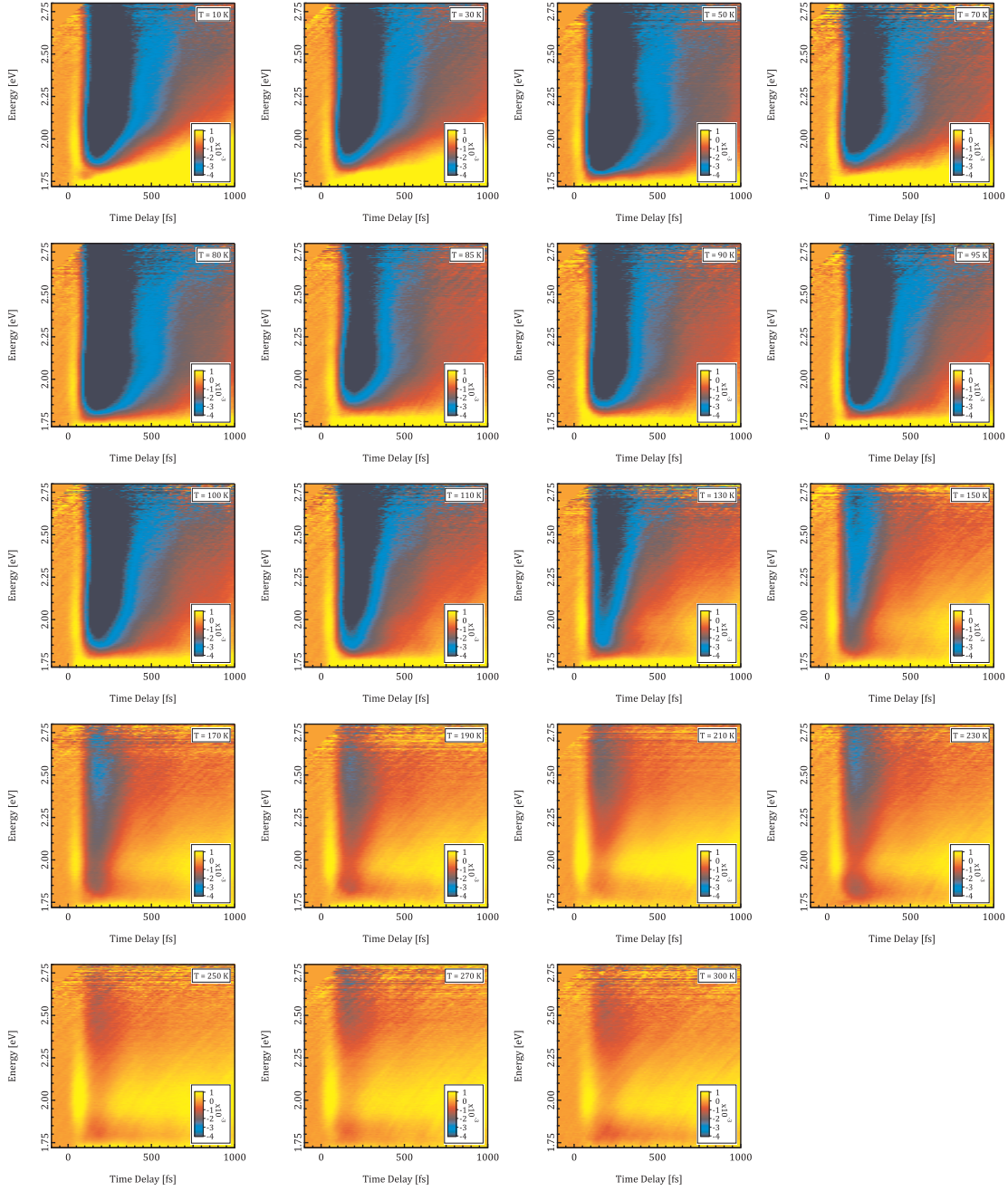
Figure 4.19 – Full temperature dependence of the time-resolved reflectivity data $\Delta R/R(\tau, E)$ for NBCO as a function of probe energy and of time delay. The temperatures are indicated in the label; the color scale is identical for all temperatures.

excitation of phonons via ISRS as discussed in chapter 2.3. A detailed analysis of the described temporal response using a global fit is given below. Figure 4.18 (c) shows the reflectivity spectra $\Delta R/R(\tau = 200\,\text{fs}, E)$ close to the maximum reflectivity change as a function of temperature. For clarity, the regimes below T_C, between T_C and T^* and above T^* are summed up as areas
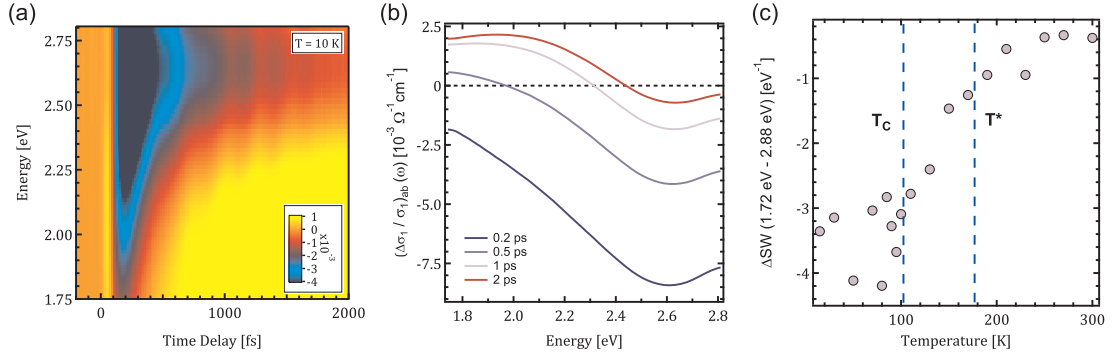
Figure 4.20 – (a) Calculated in-plane transient optical conductivity $\Delta\sigma_1/\sigma_1$ at 10 K as a function of the probe energy and of the time delay between pump and probe. (b) Temporal evolution of the $\Delta\sigma_1/\sigma_1$ spectrum at different time delays. (c) Temperature evolution of the non-equilibrium spectral weight, ΔSW, integrated over the whole probed spectrum at 200 fs.

of different shadings. The complete temperature dependence of the transient reflectivity at selected energies at the same time delay from the photo-excitation is displayed in Fig. 4.18 (d). From this plot, three temperature ranges with different spectral responses can be identified: At low temperature the signal amplitude is strong and remains almost constant up to values slightly above $T_C = 93.5$ K. As the temperature increases further, $\Delta R/R$ varies significantly and reduces its absolute intensity. Finally, as the temperature approaches room temperature, $\Delta R/R$ stabilizes around a small constant value. The overall temperature evolution can be described by two constant regimes that are separated by a crossover region. Interestingly, the crossover does not start immediately at T_c, but at slightly higher temperatures, and there is no sharp transition associated with the pseudogap temperature T^*.

To gain direct insight into the role played by the probe pulse in the different spectral regions, the transient optical conductivity $\Delta\sigma_1/\sigma_1$ is calculated for all measured temperatures, following the procedure described in chapter 3.5. Note that it is obtained directly from the combination of the static and time-resolved data, without the need for a Kramers-Kronig transform. Figure 4.20 (a) displays $\Delta\sigma_1/\sigma_1$ at 10 K as a function of time delay and probe energy, while Fig. 4.20 (b) shows the temporal evolution of its transient spectrum. A prominent drop in conductivity is found in a wide energy range between 1.9 and 2.8 eV at early time delays; on the contrary, for energies below 1.8 eV, a positive contribution emerges and progressively dominates the higher energy range as soon as the negative contribution undergoes relaxation. This response strongly differs from the one expected for a simple transient heating of the crystal, which would not display sign inversions across the measured spectrum. Therefore it can be assumed that at short time scales the pump excitation at 1.55 eV predominantly acts non-thermally. In this regard, a decreased optical conductivity is typically retrieved when a non-equilibrium distribution of carriers fills the states involved in the transitions monitored by the probe pulse (similar to the scenario discussed for LCO in chapter 4.3); an increased optical conductivity instead represents the manifestation of transient carriers absorbing the photons of the probe pulse. The calculation of $\Delta\sigma_1/\sigma_1$ for all measured temperatures provides

valuable information on the temperature evolution of the transient SW in the probed range, which is displayed in Fig. 4.20 (c) for a time delay of $t = 200$ fs. At this time delay the excited carriers have thermalized among themselves and the SW is well-defined in a physical sense. Remarkably, the calculated SW under non-equilibrium conditions is affected by the opening of the SC gap at T_C and the crossover around T^*, closely following the temperature dependence of the $\Delta R/R$ spectrum at $t = 200$ fs, but not the one of the equilibrium conductivity of Fig. 4.17 (b).

In order to determine the relative strength of the pump excitation, it is helpful to study the fluence dependence of the in-plane transient reflectivity. Fig. 4.21 displays $\Delta R/R(\tau,\mathrm{E})$ at 10 K and 300 K for different values of the absorbed fluence, indicated in the labels. At an absorbed fluence of 0.5 mJ/cm^2, the low-temperature response resembles the one presented in Fig. 4.19, displaying the typical features for the Bogoliubov QP response. As expected, the QP response is suppressed at 300 K. As the fluence is increased, the spectral response of NBCO at 10 K starts displaying a positive contribution around 2.1 eV and the negative response ascribed to the QP excitations vanishes. The rise of this spectroscopic feature represents the signature of a highly thermal non-equilibrium state driven by the pump pulse. At high fluence, the spectra are very similar at 10 K and 300 K. This indicates that the SC state response dominates the signal at the fluence used in the time-resolved experiments, while a suppression of superconductivity can only be achieved by pumping significantly harder, in agreement with typical fluence dependences reported in literature [Giannetti et al., 2009]. Note also that the signal seems to saturate at 300 K for the highest fluence values.

The analysis of the contributions to the time-resolved reflectivity signal described in Fig. 4.18 (b) is performed using a global fit procedure, as explained in chapter 3.4. Ten temporal traces are selected from each map of the full temperature dependence (Fig. 4.19) and fitted simultaneously by imposing the same time constants for all decays. A satisfactory fit of the incoherent signal can only be obtained by using at least three exponential functions convolved with a Gaussian response accounting for the temporal shape of the pump pulse. The first, positive exponential term is resolution-limited and its decay time is between 100 ps and 1 ns, far beyond the probed range. A delayed exponential has to be used for the other two components to correctly reproduce the early dynamics. The results of the fit of the temporal trace cut around 2 eV in the map at 10 K are reported in Fig. 4.22 (a), together with all the separate components of the incoherent background. The first, positive contribution that promptly emerges after the arrival of the pump pulse and decays with a long time constant τ_1 larger than hundreds of ps is effectively a step-like function. The spectral dependence of its amplitude A_1, shown in Fig. 4.22 (d), is strongly peaked around 2 eV. The other two exponential terms are instead characterized by a negative amplitude and display very different time constants. The former second, fastest contribution decays with a time constant τ_2 of hundreds of fs, while the third term has a relaxation time τ_3 of several ps. The spectral dependences of these two components A_2 and A_3 in Fig. 4.22 (e,f) show peaks around 2 eV as well, and their relative weights can be disentangled from A_1 only by means of the global fit analysis. Note that due to the short time window of the data as compared to τ_1 and τ_3, it is not possible to completely separate the

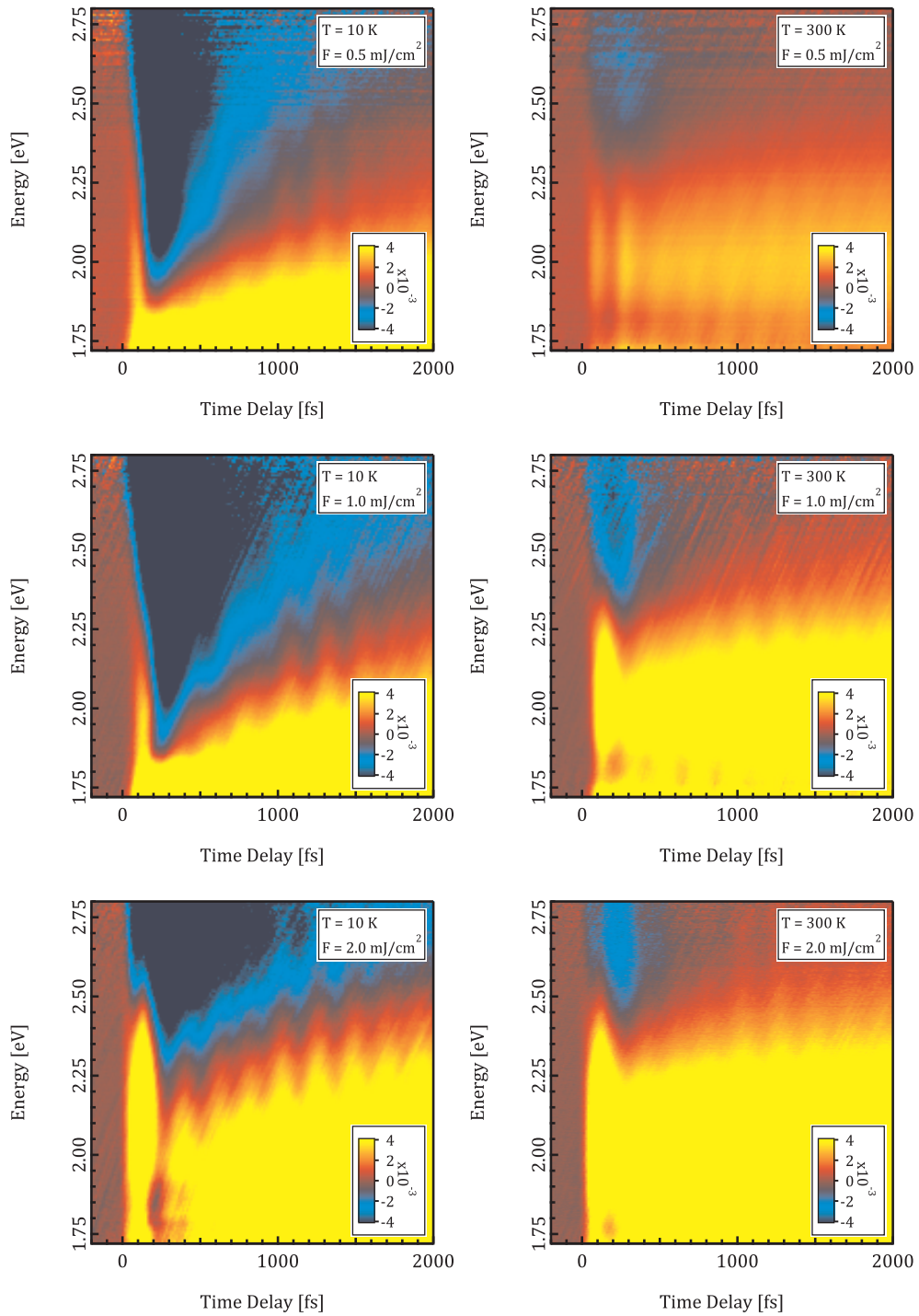Figure 4.21 – Transient reflectivity $\Delta R/R$ as a function of the probe energy and of the time delay between pump and probe at high and low temperatures for various fluences. The temperatures of 10 K and 300 K and the values of the absorbed fluence of $0.5\,\mathrm{mJ/cm^2}$, $1\,\mathrm{mJ/cm^2}$ and $2\,\mathrm{mJ/cm^2}$ are indicated in the labels. The color scale is identical for all graphs.
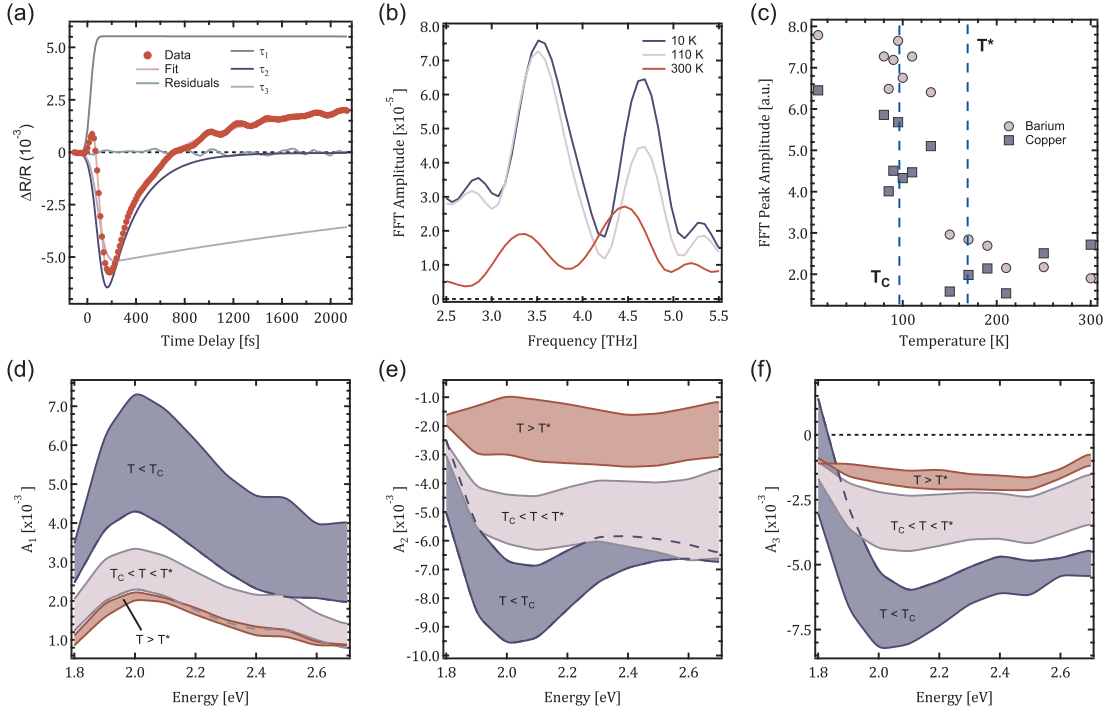
Figure 4.22 – (a) Results of the global fit analysis for the temporal trace at 2 eV from Fig. 4.18 (b): The original data are displayed as red dots, the curve obtained from the global fit is drawn in pink, the long (hundreds of ps decay) component in grey, the fast (hundreds of fs decay) component in blue and the intermediate (several ps decay) component in violet. The residuals are depicted in green, displaying an oscillatory pattern. (b,c) Fourier Transform analysis of the residuals at selected temperatures, and full temperature dependence, respectively. The two modes at 3.6 THz and 4.6 THz correspond to the Raman-active phonons involving c-axis vibrations of the Ba and Cu ions. (d-f) Spectral dependence of the amplitude for the long (A_1), the fast (A_2) and the intermediate (A_3) components as obtained from the global fit analysis.

contributions of these two exponentials. However, the important features of the dynamics are captured regardless of any cross-talk in the fit parameters A_1 and A_3. Alternatively, a good fit is achieved as well if the first exponential is replaced by a slow-rising exponential with a time constant similar to τ_2 and an additional Gaussian peak whose width is related to the pump pulse duration. Such a fit component has been used in the description of the dynamics of cuprates at low fluences [Giannetti et al., 2009]. The implications of the different contributions to the fit function are discussed further below.

Before interpreting the global fit results and the microscopic origin of the time-resolved reflectivity signal in detail, it is time to review some important results of single-wavelength pump-probe spectroscopy on the isostructural compound YBCO mentioned in chapter 4.1. The central finding of these studies was the observation of three distinct timescales in the pump-probe traces:

1. a very long relaxation lasting for several ns [Stevens et al., 1997, Thomas et al., 1996]

2. a fast decay of several hundreds of fs appearing below T^* and persisting in the SC phase [Kaindl et al., 2000]

3. an intermediate timescale of several ps, manifesting itself only in the SC phase and promptly disappearing above T_C [Kaindl et al., 2000]

Some controversy has existed regarding the assignment of the longest component, being previously ascribed to a pump-induced heating effect [Han et al., 1990] and subsequently reinterpreted as a the signature of a photoinduced absorption from localized carriers [Stevens et al., 1997, Thomas et al., 1996, Mihailovic et al., 2000]. The heating effect has been excluded as a possible origin for this component from the peculiar temperature dependence followed by its amplitude, which does not increase monotonically with increasing the sample temperature and shows instead a thermally activated behavior below T_C. The present analysis does not focus on the long-lived component, but it should be noted that the possible separation of the long-lived component into a Gaussian peak and a slow-rising exponential actually favors a heating scenario, where the heating effects are represented by the latter exponential. The Gaussian peak is instead caused by the presence of a transient population of highly non-equilibrium QPs immediately after the pump pulse arrival, similar to observations made in experiments on underdoped BiSCCO [Giannetti et al., 2009]. Since the long-lived component is not in the focus of the current experiments, the model function for the global fit is limited to the more simple version presented above, without compromising the fit quality. The characteristic temperature dependence exhibited by the other two components has led to their respective association with PG correlations and QP recombination in the SC condensate [Demsar et al., 1999]. These assignments have also been confirmed in a separate experiment with the use of a broadband probe covering the mid-IR range [Kaindl et al., 2000]. Another remarkable observation by single-wavelength pump-probe studies concerns the amplitude of the signal associated with the QP recombination across the phase diagram [Mihailovic et al., 1998]. In OD samples this component vanishes at T_C, while in UD samples the amplitude of the signal is almost unaffected across T_C and drops to zero close to T^*, i.e. in direct proximity to the establishment of the PG phase. This scenario has been explained by suggesting the existence of pre-formed CPs in the PG phase of UD YBCO [Mihailovic et al., 1998].

All three features can be observed in the present data, and in one and the same measurement. In addition, using the broadband probe covering the visible spectral range, additional insights into these microscopic mechanisms can be obtained. The positive signal of the longest component τ_1 and its increased strength at T_C finds agreement with the explanation by contributions from thermal heating combined with excited state absorption from the highly non-equilibrium transient QP population. The fast and intermediate components τ_2 and τ_3, however, need a separate discussion. Indeed, the coexistence of both components is observed far into the pseudogap phase, which implies that the signal associated with the QP response does not vanish at T_C. The spectral analysis in Fig. 4.22 (d-f) highlights that the

carriers involved into the two processes display the strongest response around 2 eV and follow distinct temperature dependences. Remarkably, A_2 exhibits its maximum amplitude at low temperature, whereas A_3 has higher weight around T_C in the probed spectral range. The global fit analysis also provides valuable information on the temperature dependence of the collective bosonic modes which are coherently generated through the ISRS mechanism. The residuals obtained from the fit of the temporal trace at 2 eV containing the oscillatory part of the signal are displayed in Fig. 4.22 (a). By means of a Fourier transform, reported in Fig. 4.22 (b), two separate modes with frequencies of ~ 3.6 THz and ~ 4.6 THz are identified. These correspond to the A_{1g} Raman-active c-axis breathing modes respectively involving the Ba and Cu ions and have been extensively discussed in spontaneous Raman scattering and time-resolved pump-probe spectroscopy of OP YBCO and NBCO [Fausti et al., 2014, Albrecht et al., 1992, Misochko et al., 2000; 2002; 2004]. In these studies, the phonon frequencies were found to undergo a blueshift when the temperature is lowered. As mentioned in chapter 4.1, an anomalous increase in the intensity of the Ba mode below T_C was demonstrated to be strictly correlated with the number of optically broken CPs, suggesting that the driving force behind the coherent excitation is provided by the change in QP density [Albrecht et al., 1992]. Hence, the Ba mode in OP YBCO was found to vanish as soon as T_C was crossed, together with the QP signal. In the present results on slightly UD NBCO, the hardening of the modes with decreasing temperature is observed as well. However, the intensity of the Ba mode still persists well above T_C, being strongly quenched well within the PG phase, as visible in Fig. 4.22 (c). This result is a second indication of the existence of a QP response, and thus, superconducting fluctuations, above T_C. The observation of the peculiar temperature dependence in the time-resolved spectra is a striking example of how low-energy phenomena (as the opening of the SC gap and of the PG) profoundly influence the high-energy electronic properties of a strongly correlated system. The identification of the in-plane interband transitions involved in the non-equilibrium dynamics is therefore crucial for the comprehension of the microscopic origin of the pump-probe signal. The pump excitation at 1.55 eV is resonant with the high-energy tail of the peak at 1.4 eV in the equilibrium σ_1 shown in Fig. 4.17 (a) that was argued to be a CT remnant. This transition has been demonstrated by a number of experiments to promote charge excitations from E_F to high-energy states [Yu et al., 1993, Holcomb et al., 1996, Mihailovic et al., 1998]. The dynamics of particle-hole excitations is subsequently monitored by the broadband probe pulse, which covers the in-plane excitations at higher energy, including the peak around 2.6 eV in the σ_1 seen in the ellipsometry data in Fig. 4.17 (a). This interband transition involves occupied states in the LHB and unoccupied states close to E_F. The calculated $\Delta\sigma_1/\sigma_1$ in Fig. 4.20 (b) shows the occurrence of a pronounced negative contribution, as the probed high-energy charge excitations become less allowed after photo-excitation.

The global-fit analysis serves as the basis for a model interpretation of the observed non-equilibrium dynamics: The arrival of the pump pulse at 1.55 eV creates a distribution of hot carriers across the Fermi energy. The resolution-limited rise and long-lived dynamics of the first exponential component with amplitude A_1 and timescale τ_1 of hundreds of ps are explained by the fact that this component includes contributions from the hot transient carrier population

and heating effects. Simultaneously, two other phenomena occur: a relaxation with a time constant τ_2 of hundreds of fs and another one with τ_3 of several ps. Both these signals exhibit their maximum amplitude around 200 fs, suggesting the occurrence of a delayed response with respect to the first contribution. This indicates that the remaining highly excited carriers decay within 200 fs to the proximity of E_F. The energy released in this fast relaxation triggers a cascade of pair-breaking phenomena, in accordance with an avalanche multiplication process proposed for YBCO [Han et al., 1990]. The effect is the breaking of a large number of CPs into Bogoliubov QPs. Since these excited QPs accumulate close to E_F, the final states associated with the high-energy interband transitions are occupied as a result of the cascade process. Thus, the broadband probe experiences a reduced absorption in the visible due to this Pauli blocking mechanism. This induced transparency is in accordance with the negative peak in $\Delta\sigma_1$ seen in Fig. 4.20 (a). The non-equilibrium SW in Fig. 4.20 (c) is a measure of the efficiency of blocking the high-energy excitations from the LHB to E_F at 200 fs. This quantity is therefore proportional to the density of Bogoliubov QPs arising from the breaking of CPs. The temperature evolution of ΔSW displays a maximum absolute value below T_C, where an increased number of QPs can be produced following the interaction with the pump pulse. A minimum plateau is instead reached around 190 K, when the density of QPs is vanishingly small. Such a behavior is not only found in the spectra at 200 fs, but can also be observed at subsequent time delays, until the QPs have completed their recombination. The pronounced effects observed at T_C and T^* in the experiment indicate that the distribution of Bogoliubov QPs created by the near-infrared pump pulse lies at the antinodes of the Fermi surface. This hypothesis was first advanced by single-wavelength transient reflectivity measurements [Gedik et al., 2004, Mihailovic et al., 2000] and later confirmed by transient angle-resolved photoemission spectroscopy [Cortés et al., 2011], which revealed that the scattering channel of the antinodal carriers towards the nodes is blocked.

The change in the antinodal QP density close to E_F triggers the coherent excitation of the Ba phonon mode. In OP YBCO this mode was found to display an amplitude anomaly at T_C [Albrecht et al., 1992], and its amplitude was shown to be in close correlation with the number of excited Bogoliubov QPs, which is negligibly small above T_C in the OP system. Recent broadband spectroscopic studies on the same material, corroborated by DMFT calculations, examined in details the interplay between the Ba mode and the in-plane interband transitions, demonstrating that a displacement of the Ba ion strongly perturbs the low-energy density of states close to E_F [Fausti et al., 2014]. However, the data in Fig. 4.22 (b,c) do not show any anomaly of the Ba phonon at T_C in the whole spectral region, consistent with a scenario in which this low-energy collective mode can be still efficiently excited above T_C. This result indicates the presence of Bogoliubov QPs far above T_C, in perfect agreement with the following interpretation of the incoherent response: The relaxation of the QPs generated by the avalanche process causes the negative reflectivity signal to decay within several ps. The decay occurs on two distinct timescales, in accordance to the established description of pump-probe optical spectra in YBCO [Kaindl et al., 2000, Mihailovic et al., 2000]. The fast timescale τ_2 embodies the recombination dynamics of the carriers which are not part of the

condensate and are thus subjected to PG correlations. Recently, the Mott-Hubbard origin of these correlations has been suggested for explaining the dynamics that follow the emergence of a highly conducting state in UD BiSCCO [Cilento et al., 2014]. The intermediate timescale τ_3 is typically associated with the recondensation of QPs into CPs. Interestingly, in the present experiments, no anomaly in the value of τ_3 is detected at T_C, as is the case in OP and OD YBCO [Kaindl et al., 2000, Mihailovic et al., 2000]. Instead, the negative signal produced by the QP relaxation persists to unexpectedly high temperatures, but does not quite persist up to T^*. This observation radically changes the interpretation of the intermediate (several ps) timescale occurring in pump-probe measurements towards a recombination mechanism into uncorrelated CPs, not accounting for their condensation. Only below T_C the CPs acquire phase coherence and condense into a macroscopic quantum state.

To summarize, the information extracted from the time-resolved reflectivity spectra as a function of temperature finds a natural explanation in the existence of a QP response in a crossover region located within the pseudogap phase, albeit not directly correlated to the PG temperature T^*. This picture confirms the strong difference in the non-equilibrium response between the UD and the OP phase of the cuprates, as already pointed out by several authors [Mihailovic et al., 2000, Gedik et al., 2005]. This finding provides strong evidence in favor of the existence of a precursor SC state comprising paired electrons lacking macroscopic phase coherence, in accordance with recent conclusions drawn from IR spectroscopy [Dubroka et al., 2011]. The present scenario also helps clarifying a body of recent works devoted to the optical control of the SC state in several UD cuprates [Fausti et al., 2011, Hu et al., 2014, Kaiser et al., 2014, Först et al., 2014]. Core to these experiments is the observation that an underlying charge density wave (CDW) instability exists in the UD region of the phase diagram, and that charge ordering competes with superconductivity [Chang et al., 2012, Torchinsky et al., 2013]. The charge-ordered state can be selectively destabilized or suppressed when a large-amplitude excitation in the mid-infrared is resonant with a CDW-related lattice mode. In the case of YBCO, the CDW suppression leads to the emergence of strongly coherent transport far above T_C, characterized by heightened interlayer mobility and carrier density similarly to the equilibrium SC state. The ultrafast timescale involved in this process was interpreted as a sign that the SC state is already present in the system before photo-excitation. An important observation is that the light-induced coherent state exists at temperatures below T^*, within the PG phase. The existence of pre-formed CPs within the PG phase of 123-family compounds represents a crucial ingredient for understanding this effect. The competition between superconductivity and charge ordering at equilibrium results in a strong suppression of CP coherence above T_C. The destabilization of the CDW by photo-excitation of a coherent THz phonon allows the pre-formed CPs to attain coherence, promoting a transient state that cannot be explored under equilibrium conditions.[6] It should be noted that a transient SC state has so far not

---

[6] Considering the great deal of attention that experiments of this type have attracted in regard to the perspective of transient SC at room temperature, it should be noted that the optical enforcement of coherence is equivalent to reducing the temperature of a subset of carriers in the material [Denny et al., 2015]. This method is conceptually identical to the well-known method of laser-cooling in the domain of ultracold atom physics, and rather different from actual room temperature SC. Still, there are many intriguing possible applications of this technique in the

been observed explicitly, but only in the form of an augmentation of the Josephson plasmon peak and a transient carrier density resembling the steady state SC electronic distribution. In this regard, definite evidence may come in the future from the real-time observation of an incomplete Meissner effect through magnetic-sensitive imaging measurements in the form of ultrafast transmission electron microscopy.

study of correlated systems.

5 Experiments on Tantalum Disulfide

In this chapter, I will report the results of experiments I performed on the charge-density wave *material* tantalum disulfide*.*

Tantalum disulfide (TaS_2) is an interesting subject in many ways. It is a prime example of a quasi-two-dimensional, strongly correlated system, very much like the cuprates discussed in chapter 4. However, it displays a number of phenomena that are very different from those previously discussed for cuprates. A variety of diverse electronic and phononic configurations can be realized in TaS_2 as a result of the interplay of Coulomb repulsion and electron-phonon dynamics. Most intriguingly, it was shown that a superconducting phase is stabilized by high hydrostatic pressures, which is interesting in view of the discussion of competition between charge ordering and superconductivity in cuprates. The properties of TaS_2 and its material class are reviewed in chapter 5.1. TaS_2 has been the subject of intense scrutiny, and only the core findings are presented. Several detailed reviews exist for further reading [Rossnagel, 2011, Sipos et al., 2008, Dean, 2010, Devereaux and Hackl, 2007]. The results of the time-resolved reflectivity experiments are presented and discussed in chapter 5.2. The large amount of acquired data makes it necessary to restrict this presentation to the core results regarding several aspects of the reported or proposed behavior of TaS_2. For the data that are shown, a full global fit analysis is performed. The analysis is of preliminary nature since the data are currently being reevaluated and prepared for publication.

5.1 Transition metal dichalcogenides

TaS_2 belongs to the class of *transition metal dichalcogenides* (TMDCs). The general formula of these materials is TX_2, where T is a transition metal atom and X is an element from the VI. main group, a "chalcogen". They possess a number of interesting properties that arise from their structure. In general, all TMDCs are layered, quasi-two-dimensional materials. The transition metal atoms are arranged in planes with a trigonal structure. Each of the planes containing T atoms is sandwiched by planes containing the X atoms that have the same trigonal structure. TMDCs come in different polytypes; the major ones are designated 1T and
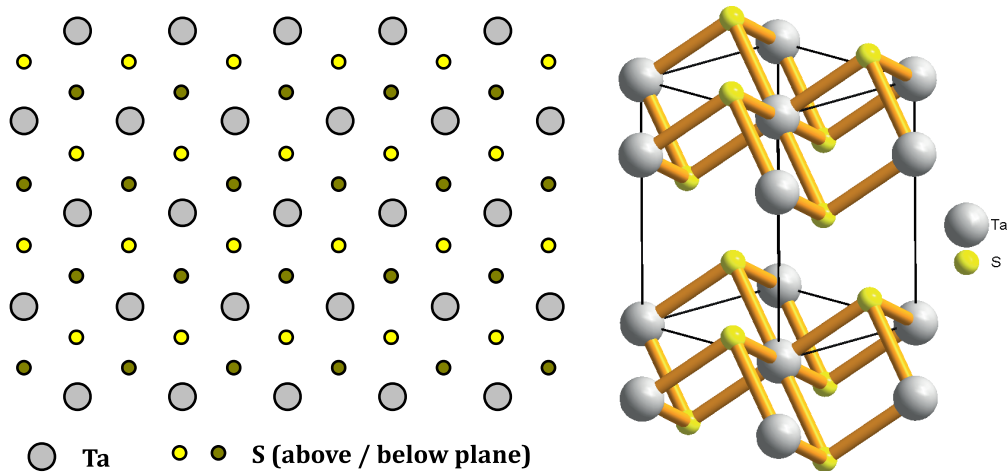
Figure 5.1 – Left: The layered structure of 1T-TaS$_2$ in the high-temperature metallic phase. The Ta plane has a trigonal symmetry and is sandwiched by S layers of the same structure. The layers above and below the Ta plane are offset horizontally, resulting in an ABC-stacking. Right: Three-dimensional arrangement of Ta and S layers in the space group P$\bar{3}$m1. The unit cell borders are indicated by dark lines.

2H, respectively. The difference between the two polytypes is the coordination of the T atom. For the 1T polytype it is octahedral, while for the 2H polytype it is prismatic. The sample studied in this thesis belongs to the 1T-polytype. For the 1T polytype, the layers containing the X atoms are offset with respect to each other, resulting in an ABC-type of stacking, as opposed to the ABA-stacking seen in the 2H -polytype. The planar structure of 1T-TaS$_2$ is indicated in Fig. 5.1. The structure can be described by the trigonal space group is $P\bar{3}m1$, with lattice constants $a = 3.365$ Å and $c = 5.853$ Å [Sugai et al., 1981, Bovet et al., 2003].

Interestingly, the layer structure of TMDCs shows parallels to that present in high-T_C cuprates, with the T layer being the equivalent of the Cu-O plane, albeit with a different symmetry. As expected form this analogy, TMDCs are strongly correlated materials that exhibit interesting properties. The physics of the transition metal layer is dominated by the competition between the on-site Coulomb repulsion U and hopping described by the transfer integral t. Therefore, just like cuprates, TMDCs can be adequately described by the Hubbard model from Eq. (2.16). While cuprates are CT insulators (cf. Fig. 2.3 (c)), TMDCs are *charge-density wave* (CDW) materials [Fazekas and Tosatti, 1979]. The physics leading to the emergence of the CDW seem to be closer to Mott insulating behavior than CT insulating behavior, and TaS$_2$ explicitly shows a Mott phase. In general, TMDCs exhibit instabilities towards various different phases, and those orders compete throughout their phase diagram [Devereaux and Hackl, 2007]. This is illustrated by the behavior of TaS$_2$, that is easily tracked as a function of temperature in static resistivity measurements [Thompson et al., 1971]: At high temperatures ($T > 550$ K), TaS$_2$ exhibits a metallic phase, as is expected from its electronic configuration. However, the metallic state has a strong instability towards a CDW state that ultimately leads to Mott insulating behavior [Fazekas and Tosatti, 1980]. Cooling below 550 K, a CDW modulation
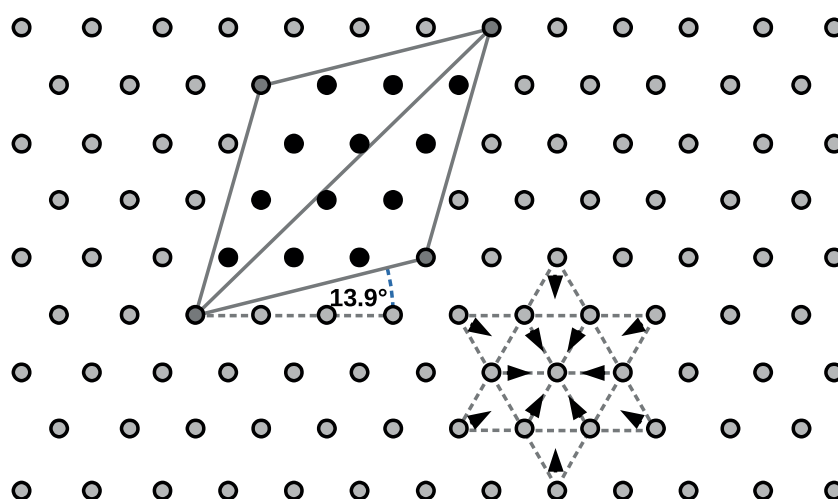
Figure 5.2 – The star-shaped cluster comprising 13 Ta atoms ("David's star cluster") appearing below the n-CDW transition temperature, and the unit cell of the superlattice formed by the commensurate CDW below the c-CDW transition temperature in TaS$_2$.

is formed in TaS$_2$. This phase is called *incommensurate* CDW (i-CDW) phase, because the wave vector associated with the CDW has no rational relation to any conceivable lattice or superlattice vector. The formation of the CDW inevitably goes hand in hand with a *periodic lattice distortion* (PLD) [Rossnagel, 2011], which displaces the Ta atoms by a small distance, roughly 0.03 Å. Upon further cooling, the character of the CDW changes below 350 K, where the CDW wave vector rotates to an angle of 11° with respect to the lattice *a* vector that gradually increases to 13° upon further cooling, and the amplitude of the PLD increases to 0.1 Å. This phase, called the *nearly commensurate* CDW (n-CDW) phase, exhibits a slight thermal hysteresis; the transition temperature is 5 K higher for heating up as compared to cooling down. It is marked by the fact that the Ta layer develops a superlattice structure composed of a regular pattern of star-shaped clusters of 13 Ta atoms (often called *David's star pattern*), as sketched in Fig. 5.2. Within each cluster, the outlying atoms shift towards the central atom. In the n-CDW phase, the ordering of the Ta layer into these clusters is incomplete, and phase separation into hexagonal regions comprising stars and intermittent triangular regions separating them occurs [Thomson et al., 1994, Spijkerman et al., 1997]. The latter also show deformation, but with a reduced amplitude. It should be noted that the formation of the star-pattern leads to a buckling of the TaS$_2$ layers [Bovet et al., 2003]. The lowest-temperature phase is entered upon cooling below 180 K, and is named *commensurate* CDW (c-CDW) phase. Its formation is accompanied by some interesting changes in the material's properties: In this phase, the star pattern of the n-CDW phase fills out the whole Ta-layer, leading to a complete CDW order. The CDW wave vector becomes commensurate with this superlattice structure, which results in a tilt angle of 13.9° with respect to the lattice vector *a*. The CDW superlattice structure is characterized by the corresponding unit cell sketched in Fig. 5.2, that has a width of $\sqrt{13}$ a ≈ 3.6 a. The c-CDW state exhibits a strong thermal hysteresis, the transition temperature to the n-CDW phase being 220 K when warming up. Also, there is a notable increase in the
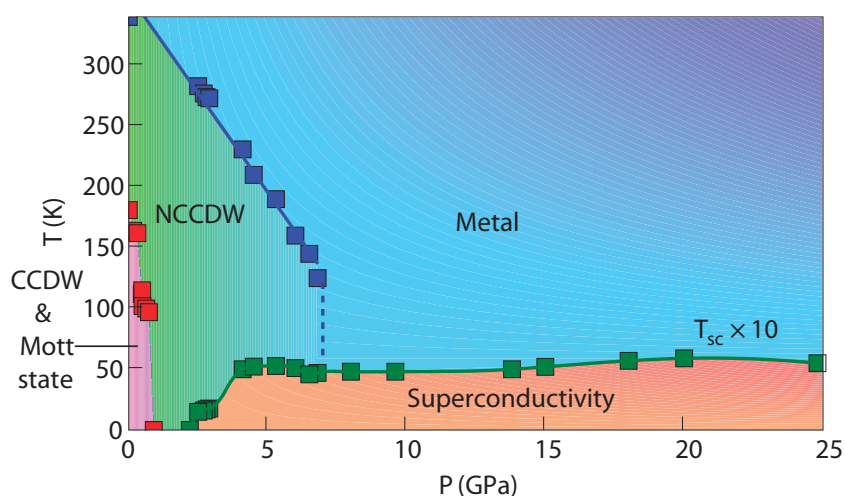
Figure 5.3 – *Adapted from [Sipos et al., 2008].* Temperature-pressure phase diagram of TaS$_2$. Upon applying large hydrostatic pressures, the charge ordering is suppressed, and a superconducting phase develops for low temperatures. Note that the superconducting transition temperature has been scaled by a factor of ten.

number of Raman-active phonons in the lowest-temperature phase caused by the change in symmetry [Duffey et al., 1976]. The most notable modes are the fully symmetric *amplitude mode* of the commensurate CDW at 2.4 THz, which will be discussed in more detail below, and the *phase mode* [McMillan, 1975]. The amplitude mode is charge neutral, and thus Raman active, while the phase mode carries a dipole moment, and is therefore infrared-active [Dean, 2010].

The structural changes are accompanied by strong changes of the band structure due to the reconstruction of the Brillouin zone [Smith et al., 1985, Rossnagel and Smith, 2006, Dean, 2010]: The twelve Ta 5d electrons from the outer atoms of the star split evenly into two separate bands below the Fermi energy. The remaining electron from the central atom of the star is located in a narrow band around the Fermi level, separated from the other bands due to spin-orbit coupling [Rossnagel and Smith, 2006]. This band would usually be half-filled, indicating a metallic state. Instead, it experiences Mott localization, and the material enters an insulating state [Fazekas and Tosatti, 1979]. The localization of the central cluster atom's electron was observed using scanning tunneling spectroscopy [Kim et al., 1994]. Naturally, the structural modification by the formation of the CDW and the accompanying changes in the electronic structure lead to a very strong electron-phonon coupling.

An intriguing feature of TaS$_2$ is the possibility to radically alter its electronic structure by applying hydrostatic pressure. The temperature-pressure phase diagram reported in literature [Sipos et al., 2008] is shown in Fig. 5.3. In general, the application of large (~ GPa) pressures suppresses the charge-ordering in the Ta planes. For pressures above 2.5 GPa, a superconducting state is induced in the material. This property is particularly remarkable in light of the discussion of a competition between charge order and superconductivity in
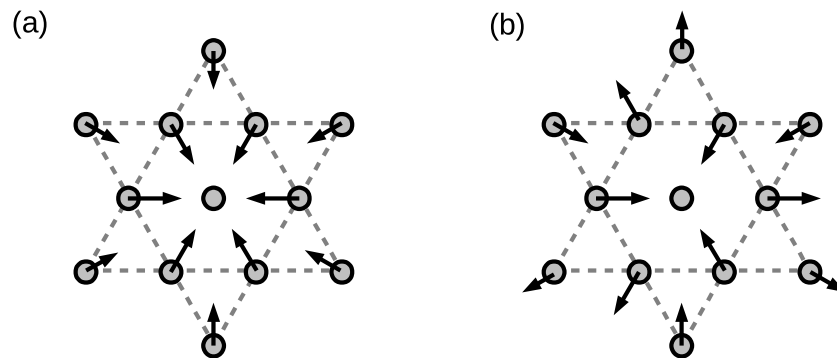
Figure 5.4 – Examples for (a) symmetric A_g and (b) asymmetric E_g modes within the star-shaped clusters of the c-CDW phase. (a) corresponds to the amplitude mode at 2.4 THz in TaS$_2$.

underdoped cuprates, and especially the results on underdoped NBCO in chapter 4.4. While superconductivity and charge-ordering are mutually exclusive, just as is the case in cuprates, the two states can coexist in separate domains in the material. In TaS$_2$, the superconducting state starts developing locally at pressures about 1 GPa, out of the metallic domains. This was used as an explanation why the superconducting state is unaffected by changes in the n-CDW domains, whereas the metallic state above the superconducting transition temperature is sensitive to the scattering by the charge-ordered domains [Sipos et al., 2008].

A number of time-resolved studies have already been performed on TaS$_2$. Single-wavelength pump-probe reflectivity measurements at 1.55 eV showed that the CDW amplitude mode at 2.4 THz is readily excited with fs laser pulses, and the gap associated with the charge-ordering can be detected [Demsar et al., 2002]. The amplitude mode experiences thermal hysteresis of its intensity and width, as was observed in static Raman measurements [Uchida and Sugai, 1981, Sugai et al., 1981]. Interestingly, the phonon coherence time is very high in the c-CDW phase, on the order of 10 ps. The coherence is strongly reduced upon transition to the n-CDW phase, showing the importance of CDW commensurability for the amplitude mode. Excitation at 1.55 eV in the c-CDW phase was also reported to trigger an E_g mode around 2.1 THz [Toda et al., 2004], which shows a curious behavior: Its intensity increases with time, correlated with the decay of the amplitude mode, reaching a maximum around 15 ps, and a beating between the two modes is observed in their subsequent decay. It has been argued that the phonon is triggered by the DECP mechanism (see chapter 2.3). However, the excitation of the amplitude mode was shown to be independent of the incoherent charge excitations by means of a control experiment using a pump-pump-probe scheme [Onozaki et al., 2007]: With this technique, it is possible to coherently generate and then amplify or suppress the amplitude mode with the first and second pump pulse. This effect is independent of the decay of the excited carriers that occurs on the timescale of about 0.5 ps. Experiments probing in the THz regime show that the photoexcitation at 1.55 eV creates a transient metallic state that differs from the steady-state metallic phase at high temperatures, because the Mott gap is melted while the PLD remains [Dean et al., 2011].

The melting of the gap and establishing of metallicity was previously observed in greater detail in femtosecond Angle Resolved PhotoEmission Spectroscopy (ARPES) measurements [Perfetti et al., 2008]. There, the prompt closing of the gap and the persistence of the PLD were used as arguments that the insulating phase of TaS_2 is caused by Mott localization, as opposed to a phonon-driven Peierls mechanism. Also, the presence of a mid-gap resonance was identified, distinguishing the transient metallic state from the high-temperature phase. The persistence of the PLD upon destruction of the insulating state was more clearly observed by time-resolved electron diffraction experiments [Eichberger et al., 2010]. It was observed that the PLD amplitude is only partially reduced, and quickly recovers on a timescale of few ps due to strong el-ph coupling. Recent ultrafast reflectivity measurements spanning a wide energy range from IR to visible showed several interesting features [Dean, 2010]: Exciting in the near IR and probing close to the gap energy $\Delta = 100$ meV, large changes in reflectivity are observed due to the shift of spectral weight into the gap upon establishing metallicity, as was previously observed by ultrafast ARPES [Perfetti et al., 2006]. However, the coherent excitation of the amplitude mode is strongest in the near-IR, around 1 eV, and seems to be unconnected to the low-energy dynamics. Also, the transient metallic state was conjectured to be of polaronic nature because of three features: A reduced IR conductivity compared to the high-temperature metallic phase, an asymmetric phonon lineshape indicating strong el-ph coupling, and the presence of the mid-IR feature around 155 meV [Dean et al., 2011].

5.2 Time-resolved experiments on Tantalum Disulfide

The TaS_2 samples were grown in the LPMC at EPFL, following an established procedure [Dardel et al., 1992]: Single crystalline samples were prepared by *chemical vapor transport* (CVT) from pure elements with iodine as a transport agent, with the growth temperature varying between 950°C in the hot zone and 900°C in the cold zone. The 1T-polytype was stabilized by the addition of SnS_2 (less than 0.5% weight) and by rapid cooling from the growth temperature. The material grows in flakes with a diameter of few mm and a thickness of some 100 μm. The surface of the flakes is perpendicular to the *c*-axis of the material.

For the experiments, flakes of appropriate dimensions were chosen and oriented by Laue diffraction. The flakes were not polished. Instead, they were glued to a mount using fast-drying silver paint, and a clean surface was produced by scotch-taping (see chapter 3.1). The surface under study is thus parallel to the Ta layers. Time-resolved reflectivity measurements as described in chapter 3.3 were performed for various experimental parameters: The response to a pump energy of 1.55 eV was studied at three distinct temperatures (10 K, 230 K and 300 K) in the c-CDW and n-CDW phases. For all three temperatures, spectra were taken at different combinations of pump and probe polarizations. The fluence dependence of the response was measured at 10 K and 300 K for 1.55 eV pump energy, and at 300 K for excitation at 3.1 eV. Finally, the pump energy was tuned in the NIR between 1.05 eV and 0.54 eV (1200 nm and 2300 nm) at 300 K.
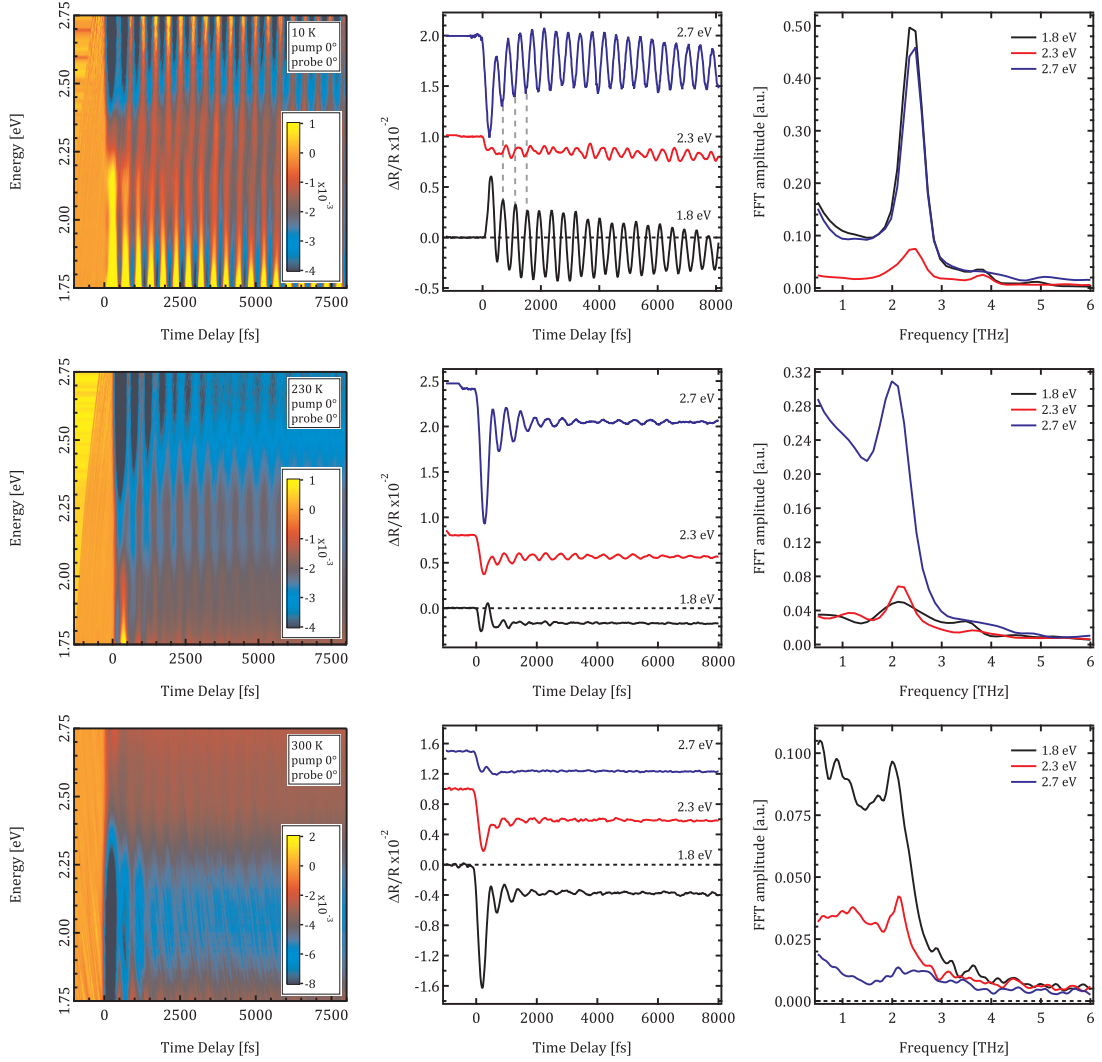
Figure 5.5 – Left column: Time-resolved reflectivity spectra of TaS$_2$ in the c-CDW (10 K) and n-CDW (230 K, 300 K) phases. Middle column: Time traces for select energies, representing three distinct regions in the spectra. Traces are offset vertically for clarity. Right column: Fourier transform of the selected traces, revealing the frequency of the coherent oscillations.

The time-resolved reflectivity data for an excitation energy of 1.55 eV at the three different measurement temperatures are shown in Fig. 5.5. The incident fluence is approximately 2 mJ/cm^2. The left column shows the color-coded reflectivity change as a function of time delay and probe energy for the c-CDW phase (10 K) and the n-CDW phase (230 K, 300 K). Most notably, all spectra are dominated by strong coherent oscillations present over the whole probing range. The differences between the three regimes can be seen in the time traces at three fixed energies (1.8 eV, 2.3 eV, 2.7 eV) displayed in the middle column: At 10 K, the response is completely dominated by the coherent oscillations that are very long-lived, having a coherence time far greater than the probe window of 8 ps. For higher temperatures, the
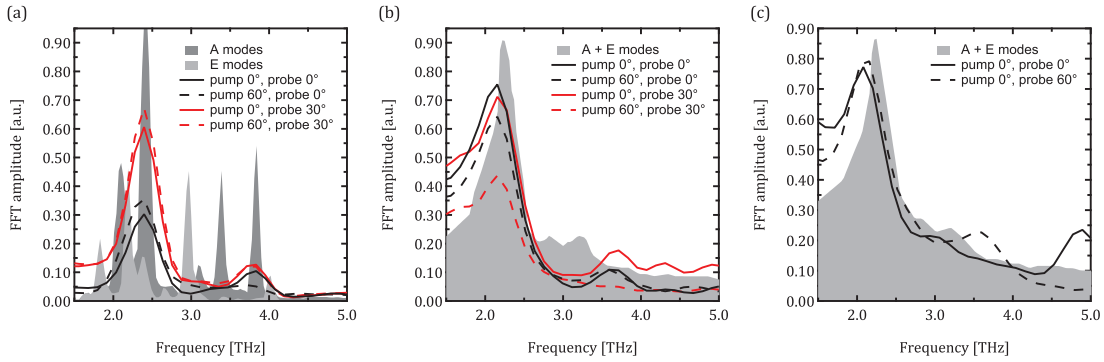
Figure 5.6 – Fourier transforms of the transient reflectivity of TaS$_2$ at 2.4 eV probe energy for various combinations of pump and probe polarizations, at (a) 10 K, (b) 230 K and (c) 300 K. The shaded area shows Raman data reported in literature recorded at the same energy [Sugai et al., 1981] for (a) 23 K, (b) 205 K, but above the n-CDW-to-c-CDW transition, and (c) 273 K.

coherence time is significantly lower, around 1 ps. The oscillations are overlaid by a negative incoherent background that reaches a plateau for times greater than 2 ps. A beating is visible in some of the traces, revealing the presence of a second coherent oscillation. This effect is most obvious in the trace at 2.3 eV, where the two oscillations seem to have a roughly equal amplitudes. Notice that at 10 K the oscillation clearly inverts its phase across the spectrum, as indicated by the broken lines in the traces. This trend is less pronounced at higher temperatures. The right column of Fig. 5.5 shows the Fourier transform of the traces displayed in the middle column, allowing to identify the modes present in the spectra. As expected, the long-lived oscillation in the c-CDW phase is the CDW amplitude mode at 2.4 THz. The second oscillation responsible for the beating is located around 3.8 THz. Instead, the slow-rising 2.1 THz mode observed in single-wavelength experiments in the c-CDW phase [Toda et al., 2004] cannot be identified directly, although it should be visible in the time window covered by the scans. The 3.8 THz mode is shifted to 3.6 THz in the n-CDW phase at 230 K, while the stronger oscillation in that phase is peaked around 2.1 THz. The same situation is found at 300 K, although the shortened coherence time makes the modes less visible in the Fourier spectra. While there is consensus in literature that all three oscillations are associated with CDW oscillations, the modes at 2.1 THz and 3.8 THz are unfortunately not well characterized. Early Raman data showed a strong softening of the amplitude mode with increasing temperature [Sai-Halasz and Perry, 1977], leading to the conclusion that the 2.1 THz mode prominent in the n-CDW phase is the equivalent of the amplitude mode in the c-CDW phase. However, the above-mentioned 2.1 THz mode in the c-CDW phase was identified as asymmetric by polarized Raman scattering, and above the transition from the c-CDW phase to the n-CDW phase the strongly softened amplitude mode that started at 2.4 THz merges with the asymmetric 2.1 THz mode [Sugai et al., 1981]. It is likely that the 2.1 THz mode seen in the time-resolved spectra at higher temperatures is the amplitude mode, as discussed further below.

Figure 5.6 compares the Fourier transforms of the transient reflectivity at 2.4 eV probe energy

Figure 5.7 – Fluence dependence of the transient reflectivity change of TaS_2 at 10 K for 1.55 eV pump energy. The fluence is indicated in the labels. The overlaid traces show the time evolution of the signal at 2.7 eV probe energy. The last panel shows the Fourier transform of the overlaid traces.

for a few representative combinations of pump and probe polarizations at the three temperatures from Fig. 5.5 to Raman data reported in literature taken at the same energy [Sugai et al., 1981]. The polarizations that are indicated are given as the in-plane angle from the *a*-axis. All three phonons that are excited have been characterized as symmetric modes. No clear dependence of the oscillations on the polarizations is discernible, in accordance with previous reports [Dean, 2010]. The same is true for the all other measured polarization combinations, not shown in Fig. 5.6. As illustrated in Fig. 5.4, it should be possible to identify asymmetric modes by taking the difference between a Fourier transform for parallel polarization and one where either pump or probe are rotated by 60°. However, no unique trend can be observed, and any small differences are likely to be numerical artifacts caused by the FFT algorithm. The most probable conclusion is that no asymmetric modes are excited.

Figure 5.7 shows the fluence dependence of the transient reflectivity at 10 K, in the c-CDW phase, for excitation at 1.55 eV. The spectral features remain virtually identical over a fluence range of an order of magnitude. The time traces at a probe energy of 2.7 eV, close to the maximum signal strength, are overlaid in the spectra, and are representative of the general trend: Both the oscillation amplitude and the intensity of the incoherent background scale almost perfectly linear in fluence, as reported in literature [Dean, 2010]. In the last panel of the figure, the Fourier transforms of the traces at 2.7 eV are shown. The peak of the CDW
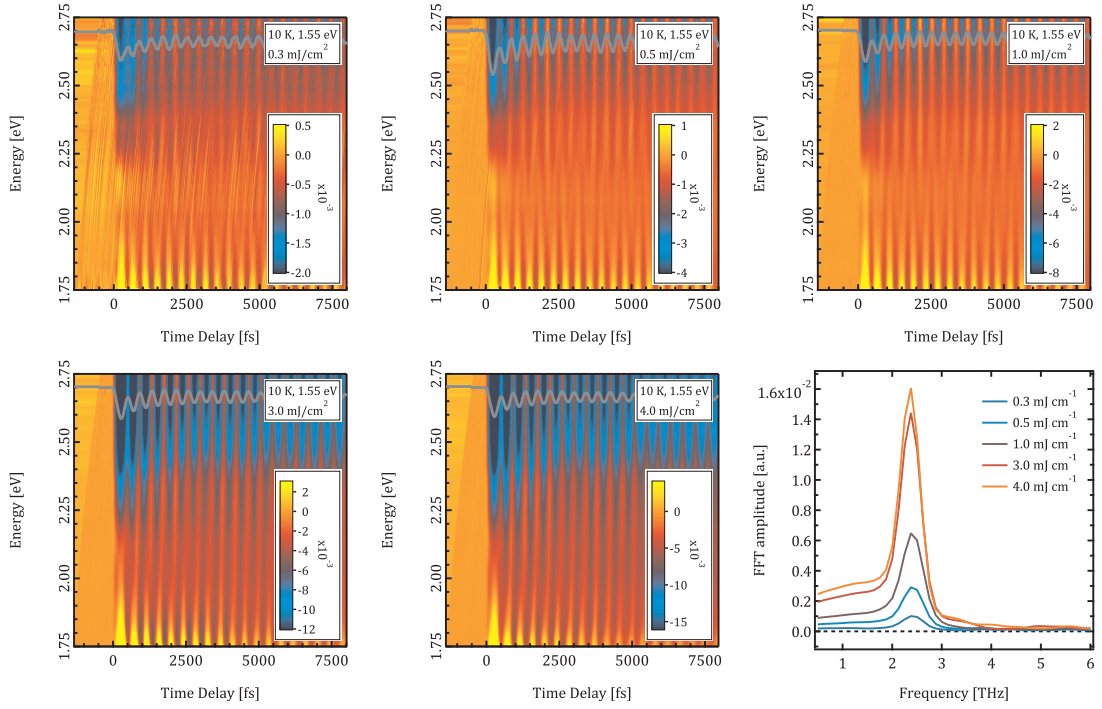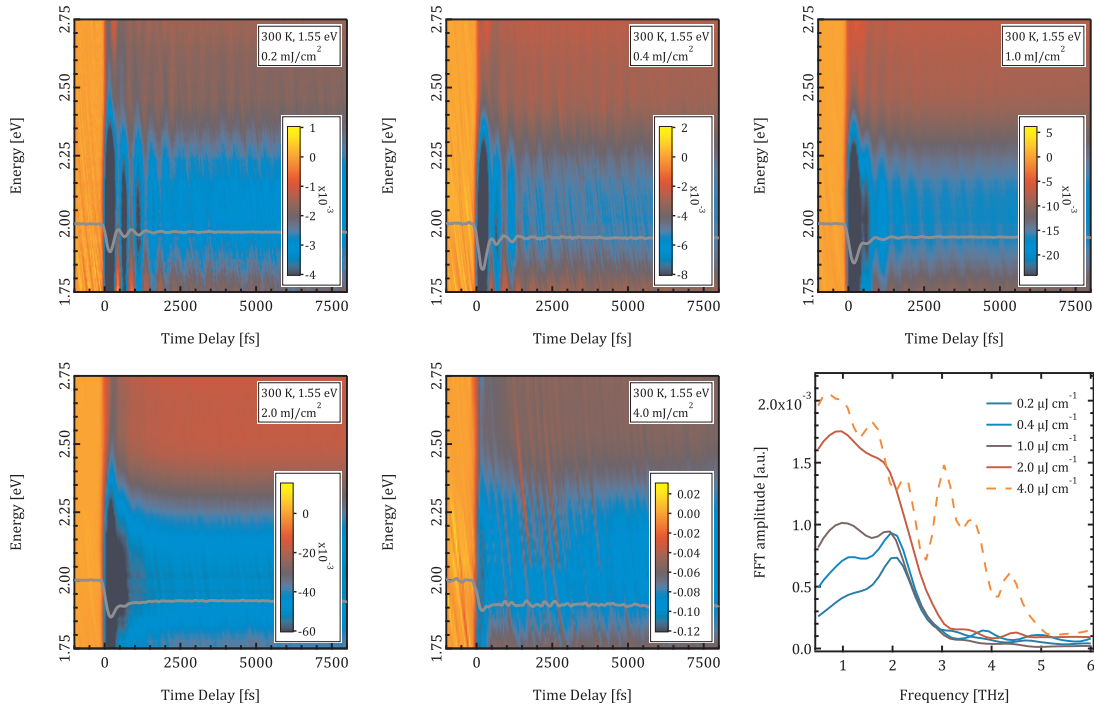
83

Figure 5.8 – Fluence dependence of the transient reflectivity change of TaS$_2$ at 300 K for 1.55 eV pump energy. The fluence is indicated in the labels. The overlaid traces show the time evolution of the signal at 2 eV probe energy. The last panel shows the Fourier transform of the overlaid traces.

amplitude mode retains its shape for all fluences. Note that the 3.8 THz mode is barely visible at 2.7 eV probe energy. An equivalent fluence dependence measured at 300 K is shown in Fig. 5.8. As mentioned above, the coherence time of the oscillation is significantly shorter, and the signal peaks around 2 eV probe energy. At this energy, the time traces are overlaid to the spectra. Here, in contrast to the fluence dependence in the c-CDW phase in Fig. 5.7, only the level of the incoherent background scales linear with fluence, while the oscillation amplitude seems rather unaffected by the increase in pump power. In addition, the incoherent part of the signal goes into saturation for the highest fluence value, which was not the case in the c-CDW phase. This difference cannot be explained by the optical properties of the material. While the optical constants show differences in the visible range between the two phases (see e.g. [Barker et al., 1975]), the changes are not large enough to explain the observed discrepancy in the fluence dependences. Instead, the likely explanation for the lower saturation threshold at room temperature is the strongly reduced coherent phonon activity, which is able to efficiently disperse the deposited pump energy at lower temperatures. The Fourier transforms in the last panel of Fig. 5.8 show the peak of the amplitude mode, around 2.1 eV in the n-CDW phase. Again, as was the case in the c-CDW phase, its shape is rather unaffected by the increase in pump fluence, even though its amplitude does no longer scale linearly with fluence and it gradually becomes superimposed by the incoherent background. The results of the fluence
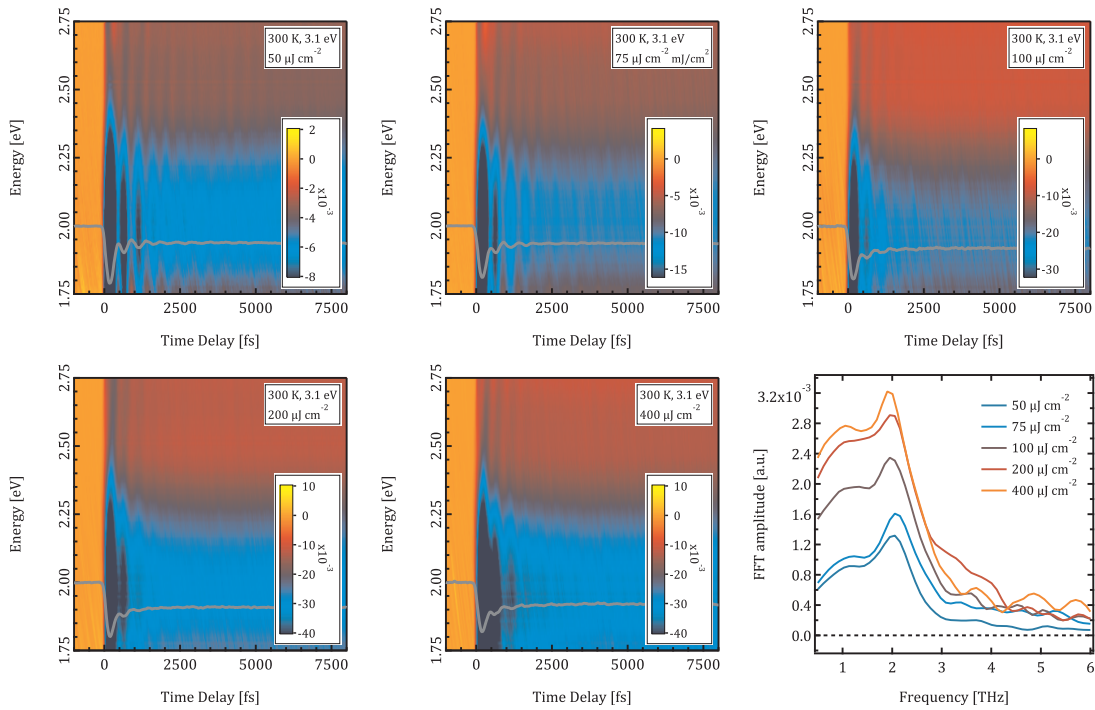
Figure 5.9 – Fluence dependence of the transient reflectivity change of TaS$_2$ at 300 K for 3.1 eV pump energy. The fluence is indicated in the labels. The overlaid traces show the time evolution of the signal at 2 eV probe energy. The last panel shows the Fourier transform of the overlaid traces.

dependence at 300 K for the frequency-doubled excitation at 3.1 eV are shown in Fig. 5.9. At first glance, the spectra are similar to excitation at 1.55 eV. The coherence time of the oscillation is comparable, as are the spectral dependence and decay time of the incoherent background. However, exciting at 3.1 eV, the fluence necessary to achieve the same level of signal as for excitation at 1.55 eV is far lower, roughly by an order of magnitude. The overlaid time traces at 2 eV are very similar to those in Fig. 5.8, but no saturation is reached for the used fluences. These effects are most likely the result of two factors, an increase in absorbed energy due to a resonance effect when changing the pump energy, and a more efficient excitation of the CDW amplitude mode at 2.1 THz for excitation in the UV, in accordance with the amplitude mode resonance profile obtained from the global fit analysis below.

Figure 5.10 reports the transient reflectivity spectra in the n-CDW phase at 300 K for various pump energies in the near-IR using the TOPAS (cf. chapter 3.3). Note that polarization of the TOPAS output is rotated for lower pump energies, when using the "idler" part of the output. Nonetheless, all the data can be compared directly, since the sample's in-plane response is isotropic. Again, the spectra follow the general trend observed in the fluence dependences for excitation at 1.55 eV and 3.1 eV. The signal peaks around 2 eV, where the time traces are overlaid to the spectra, and is dominated by the incoherent background. A coherent oscillation is present and decays with a time constant of approximately 1 ps. The Fourier
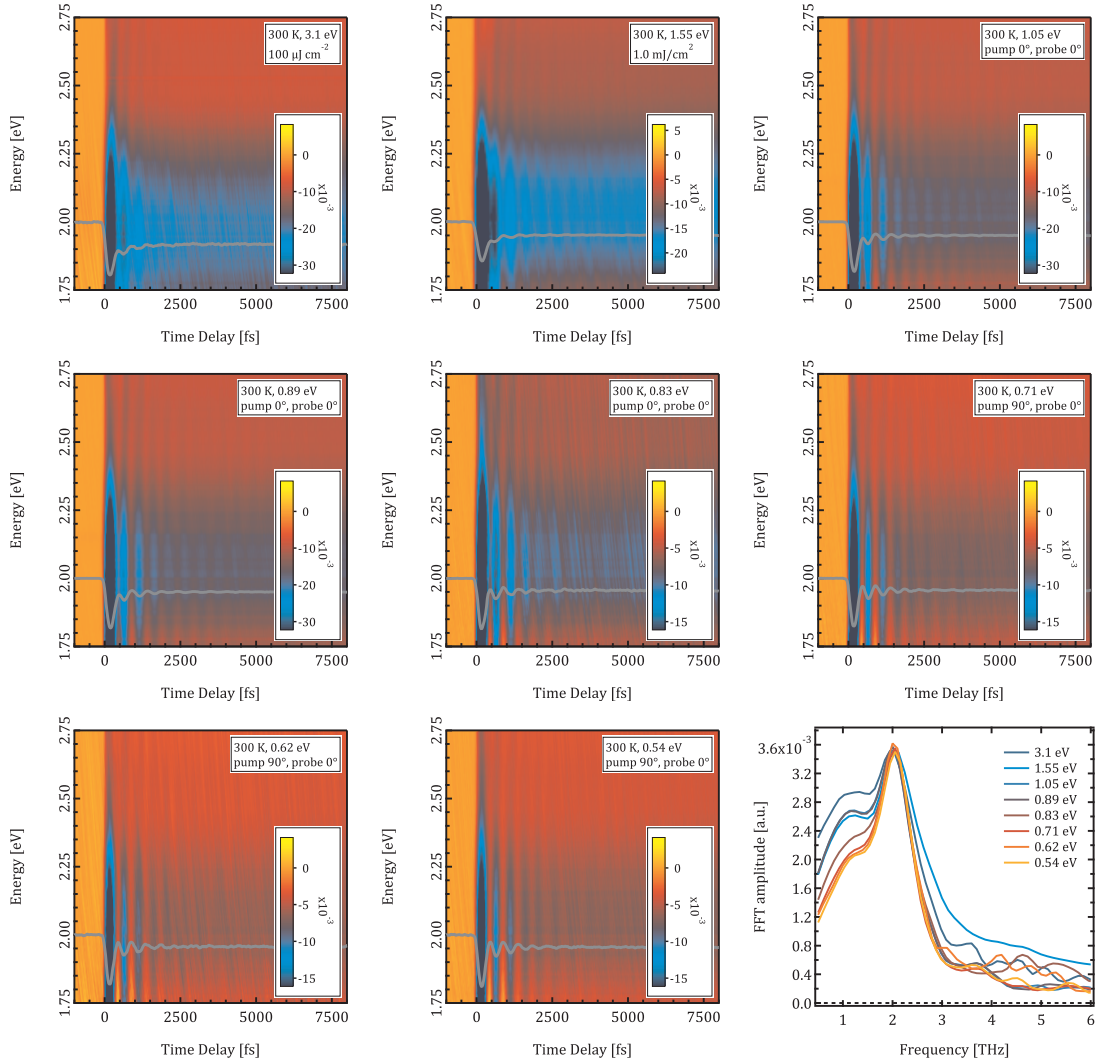
Figure 5.10 – Pump energy dependence of the transient reflectivity change of TaS$_2$ at 300 K from the UV to the NIR. The pump energy is indicated in the labels. The overlaid traces show the time evolution of the signal at 2 eV probe energy. The last panel shows the Fourier transform of the overlaid traces, normalized to the peak at 2.1 THz.

transform spectra are shown in the last panel; curves for 1.55 eV and 3.1 eV at comparable signal level have been added for reference. All transforms have been normalized to the value of the 2.1 THz peak. The spectra reveal that the shape of the CDW amplitude mode is again largely independent of the pump energy. However, the peak width seems slightly reduced for excitation in the IR. The mode at 3.8 THz is present as well, but again is rather weak. From the traces at 2 eV it can also be seen that the strength of the amplitude increases slightly when reducing the pump energy. This can be explained as a resonance effect, in accordance with the spectral response of the mode discussed in the global fit analysis that follows.

All spectra have been analyzed using a global fit, as detailed in chapter 3.4. The spectra have

Figure 5.11 – (a-c) Global fit traces (broken lines) for the time traces at various probe energies from Fig. 5.5 for (a) 10 K, (b) 230 K and (c) 300 K. Traces have been offset vertically, and some traces have been scaled for clarity. (d-f) Decomposition of the global fit traces from panel (a) into the three oscillations and the exponential background for probe energies of (d) 1.8 eV, (e) 2.3 eV and (f) 2.7 eV.
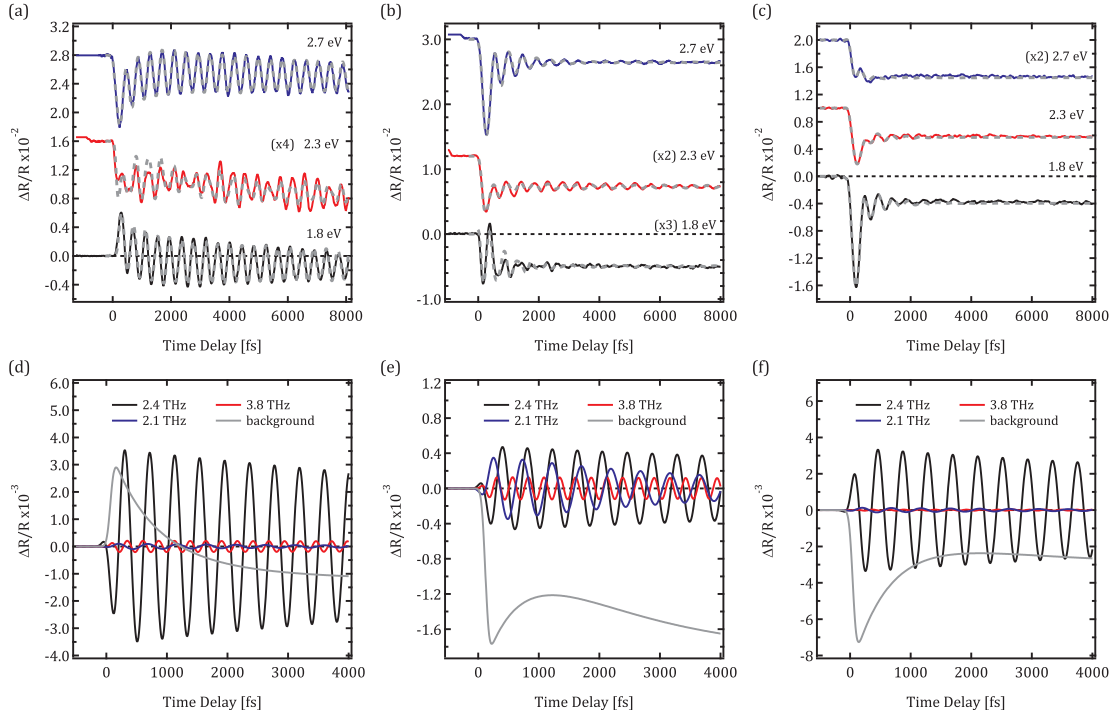
been divided into time traces by integrating over energy windows of 100 meV width. A single fit function can be used to fit *all* measured reflectivity spectra over their whole probe spectrum with very good accuracy. It comprises two exponentials, a rise and a decay, modeling the incoherent background, and three damped oscillations to account for the three observed phonons. Figure 5.11 (a-c) shows a few select global fit traces, corresponding to the reflectivity spectra at different temperatures shown in Fig. 5.5. For each dataset, the global fit function uses shared rise and decay times and oscillation frequencies across the probe spectrum. The oscillation frequencies of the three phonons take on values of 2.1 THz, 2.4 THz and 3.8 THz (in the c-CDW phase) resp. 3.6 THz (in the n-CDW phase). The overall fit quality is very good. The components of the global fit traces for 10 K are shown in Fig. 5.11 (d-f). They offer some insight into the behavior of the reflectivity spectra. First, comparing the amplitude mode to the exponential background, it becomes obvious that the former has a cosine shape. This agrees with reports in literature that it is triggered by a DECP mechanism. Second, it becomes clear that the 2.1 THz mode known from Raman that was reported in earlier time-resolved experiments in the c-CDW phase [Toda et al., 2004, Dean, 2010] is present in the 10 K spectra as well, although its contribution is very small compared to the dominating amplitude mode. This was not apparent from the FFT spectra in Fig. 5.5, because there its peak was hidden by the broad amplitude mode peak. Third, the 3.8 THz mode has a rather small amplitude, but a
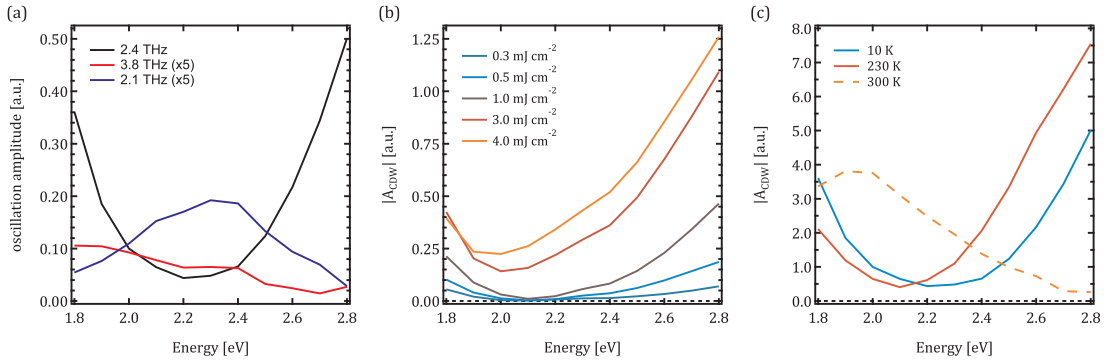
Figure 5.12 – (a) Spectral dependence of the coherent phonon amplitudes for all three excited modes in the c-CDW phase at 10 K. (b) Fluence dependence of the CDW amplitude mode at 10 K. (c) Temperature dependence of the CDW amplitude mode, i.e. the 2.4 THz mode at 10 K and the 2.1 THz mode at 230 K and 300 K. For clarity, absolute values are shown in all panels; the 2.4 THz mode has a negative amplitude on the low-energy side of the minimum.

very long coherence time, explaining its visibility in the FFT spectra. Lastly, the short-lived component of the exponential background inverts its sign over the probe spectrum, while the long-lived component remains negative. It should also be noted that the short-lived component of the background is instead negative over the whole probe range in the n-CDW phase, and gains in intensity.

The global fit analysis allows to study the energy dependence of the coherent phonons that are excited in the time-resolved spectra. Figure 5.12 shows the main results of this analysis. Panel (a) displays the resonance profiles in the c-CDW phase at 10 K, in terms of absolute values of the oscillation amplitude. The amplitude mode at 2.4 THz has a negative amplitude on the low-energy side of the minimum in panel (a). Its intensity increases steeply on both sides of the probe spectrum, which is in accordance with the observation that it is excited more efficiently when tuning the excitation energy either towards the UV or towards the near-IR. The 2.1 THz mode shows a maximum in the center of the spectrum; close to the minimum of the amplitude mode, in accordance with the observations from the time traces in Fig. 5.5. The 3.8 THz mode does not show a clear probe energy dependence. A fluence dependence of the CDW amplitude mode at 10 K is shown in panel (b). As mentioned before, the mode largely scales linear with fluence. Its overall profile shape remains the same, but the minimum of the absolute value (i.e., the zero-crossing of the amplitude) changes to lower energies for higher fluences. Lastly, the temperature dependence of the amplitude mode is shown in panel (c). Note that the mode in question is the 2.4 THz one for 10 K, but the one at 2.1 THz for 230 K and 300 K. The dependence is nearly identical for 10 K and 230 K, but for the latter the minimum is shifted towards lower energies. Comparing to the fluence dependence in panel (b), this shift can be explained by the increased incoherent background, and thus higher electronic temperature of the sample in the n-CDW phase. Instead, the profile is drastically altered at 300 K. It no longer corresponds to the lower temperature profiles, but resembles the shape of the incoherent peak visible in the spectra in Fig. 5.5, indicating that at this temperature the

phonon dynamics is dominated by the behavior of said background.

It is now time to review the results presented in this chapter. Most of them are in agreement with literature, but still they offer some new insights. The temperature dependence in Fig. 5.5 shows the general features reported in earlier experiments, namely the large amplitude and long coherence time of the CDW amplitude mode in the c-CDW phase, and the decrease of both upon entering the n-CDW phase. However, the amplitude mode spectrum turns out to be strongly dependent on the probe energy, as confirmed by the global fit analysis in Figs. 5.11 and 5.12. This is particularly important considering that previous works rely heavily on single-wavelength optical experiments. The resonant profile of the CDW amplitude mode extracted from the global fit is in agreement with the fact that the oscillation strength increases when changing the excitation energy towards the UV or the near-IR, as seen in Figs. 5.9 and 5.10. Note that the latter data are taken in the n-CDW phase; it would be interesting to repeat these experiments in the c-CDW phase in the future. A particularly intriguing experiment would be a study of the changes in the visible spectrum upon direct excitation of the phonon modes in the sub-200 meV range, close to the reported transient peak that occurs upon the melting of the Mott gap. The global fit analysis also reveals that the 2.1 THz mode is present in the c-CDW phase, as reported before, but has a very low intensity. Notably, most static Raman data available in literature have been taken at 2.4 eV, the standard output energy of an argon ion laser system, close to the minimum of the amplitude mode intensity, which explains why the 2.1 THz mode is far more prominent in those data. As mentioned in the discussion of the resonance profiles in the c-CDW phase in Fig. 5.12 (a), the 2.1 THz mode shows a peak when the CDW amplitude mode intensity is minimal. This can be seen as a manifestation of the apparent competition between the two modes reported in single-wavelengths experiments [Toda et al., 2004], in which it was proposed that strength of the asymmetric 2.1 THz mode is correlated to the decay of the amplitude mode. It was also speculated that the 2.1 THz mode is launched simultaneously with the amplitude mode, but cannot affect the reflectivity while the latter is present. The broadband data in the visible confirm that the asymmetric mode is indeed present from the beginning of the measurements, and that it is visible in the reflectivity data outside the spectral region dominated by the amplitude mode. An explanation of this behavior would require an analysis of the band structure of TaS_2, which is currently worked on. More information could also be gained through a broadband study for a longer time window. Moreover, as shown in Fig. 5.6, no dependence of the reflectivity data on the polarizations was observable. However, given the fact that the 2.1 THz mode in the c-CDW phase was determined to be asymmetric, a careful study of spectra allowing the launching of asymmetric modes using a global fit might show a dependence nonetheless, especially if the experiment is performed for an excitation energy around 2.4 eV, where the amplitude mode contribution is minimal. Finally, the observed cosine shape of the oscillations agrees with a triggering of the coherent modes by the DECP mechanism, requiring a driving force that lasts significantly longer than the phonon period. The present results agree with conclusions drawn from time-resolved ARPES [Perfetti et al., 2008]: The quasi-instantaneous melting of the CDW Mott gap destabilizes the star-shaped CDW clusters, which release stored elastic energy that in turn can drive the

phonons. Looking at the incoherent background, it was established electronic relaxations occur on the timescale of 150 fs, while the observed relaxation on the ps scale was attributed to lattice relaxation [Eichberger et al., 2010]. This explains the long coherence time of the modes in the c-CDW phase. In the n-CDW phase, instead, the non-commensurability of the clusters leads to strong scattering, drastically shortening the amplitude mode life time. Altogether, the broadband experiments reveal several interesting features of the dynamics of TaS_2, while confirming previous results. A logical next step would be an experiment exciting the material in the mid-IR, which requires some modification of the experimental setup to circumvent the problem that air strongly absorbs IR radiation in this regime. These experiments might reveal features of the proposed polaronic conductivity in the transient metallic state, which is not detectable in the present data taken at 300 K, and the global fit analysis should be able to reliably isolate the reflectivity change due to the melting of the Mott gap from the incoherent background.

6 Concluding Remarks

I will give a quick summary of the main results of my thesis, and discuss possible next steps.

This thesis deals with femtosecond broadband spectroscopy of correlated materials. It demonstrates that a "simple" optical experiment offers a vast amount of information on the physics of a solid state system. The advantages of an all-optical pump-probe experiment lie in its ability to study virtually any sample in a contact-free, non-destructive manner, the high time and energy resolution that allow interaction with the electronic and bosonic degrees of freedom on their inherent time and energy scales, and the great amount of control over the light pulses that can be tailored to the needs of the experiment. Altogether, these aspects offer the possibility for well-defined excitation and study of materials. The data presented in this work are all taken on materials belonging to the class of strongly correlated electron systems. These materials exhibit a wide range of physical phenomena, most notably superconductivity and charge and magnetic ordering. The inherent many-body nature of correlated systems leads to the breakdown of simple model approaches, making the understanding of the physics of these systems extremely challenging. One central effect of the correlations is that low-energy bosonic excitations are strongly coupled to high-energy electronic excitations. This is the point where time-resolved optical experiments become most useful: The optical excitation allows to access high-energy electron-hole pairs via dipole-allowed transitions as well as low-energy bosonic excitations using Raman-type processes. Therefore, these experiments are ideally suited to study the interplay between the two energy scales, and the possibility to coherently excite bosons can be exploited in control experiments or for investigating transient material states.

The experiments on cuprates presented in chapter 4 demonstrate the different aspects of the usefulness of time-resolved broadband spectroscopy in studying correlated systems. The experiments on the optimally doped superconductor in chapter 4.2 combine the evaluation of spectroscopic data with the ability to coherently trigger phonons as well as a superconducting charge fluctuation. The resonant behavior of the latter clearly shows a coupling of the superconducting condensate to electronic excitations on a high-energy scale. The generalization of this Coherent Fluctuation Spectroscopy approach into a more general tool discussed

in the treatment of the undoped parent compound in chapter 4.3 proves that it is possible to extract reliable values for matrix elements from the broadband data. This will be useful to quantify the interplay between high- and low-energy degrees of freedom in correlated systems. A very interesting future experiment would be the application of this method to the superconducting fluctuations in an optimally doped cuprate. A good example for the study of incoherent excitations using broadband experiments is provided by the discussion of slightly underdoped NBCO in chapter 4.4. The wide probe range of the experiment revealed many aspects of the quasiparticle dynamics in a single experiment, and allowed to observe preformed electron pairs existing within the pseudogap phase. Moreover, these experiments are part of a larger project motivated by the ability to study correlated systems using the technique of Coherent Fluctuation Spectroscopy introduced in chapters 4.2 and 4.3. It has become evident that the rich phase diagram of cuprates is the result of a complex interplay of several coexisting or competing phases that originate from the interaction of the in-plane carriers with the surrounding electronic and bosonic degrees of freedom. A step forward in the task of understanding high-temperature superconductivity will be provided by identifying what degrees of freedom are important in the vicinity of the superconducting phase, and tracing them throughout the phase diagram using broadband spectroscopy. To this end, data for more doping values are being taken. The study of TaS_2 in chapter 5 is an interesting addition to this discussion, because its physics are in some way a counterpart to the results presented for cuprates. The general features of TaS_2 are similar to cuprates, in particular the quasi-two-dimensional structure with in-plane dynamics that are marked by the interplay of Coulomb repulsion and strong electron-phonon coupling. Because of this, the material exhibits charge-ordered and superconducting phases, very much like cuprates. However, the material is of Mott-insulating nature and prone to forming a superlattice caused by the manifestation of the charge density wave. As demonstrated, ultrafast pump-probe experiments allow to melt the Mott state and excite and study the coherent motion of phonons associated with the charge ordering. A global fit analysis allows to obtain the resonant behavior of those phonons. These resonant matrix element data can be used to further refine the model of the CDW, in particular its coupling to the periodic lattice distortion. Also, experiments close to the commensurate / nearly commensurate phase transition might yield interesting results due to the observed hysteretic behavior. Time-resolved experiments can be used to determine whether the hysteresis is driven by the charge order or the lattice configuration. Another interesting future experiment would be tuning the excitation energy in the commensurate charge density wave phase. In particular, the proposed polaronic conductivity in that phase should be visible in the transient reflectivity data when pumping close to the center of the band's peak in the mid-IR around 155 meV.

Finally, the setup used in this work offers a few interesting possibilities that were not exploited in this thesis. The first one is a combined time-resolved broadband reflectivity and magneto-optic Kerr effect study. A project along this line is currently underway on magnetite, with the aim of studying its properties across the Verwey transition, a combined charge / orbital ordering phase transition that results in an insulating state. The combined approach is

particularly powerful, because it yields information on the electronic, phononic and magnetic degrees of freedom of a sample, allowing to establish a comprehensive picture of the interplay between the three. Second, the matrix elements and resonance profiles that are extracted from the broadband experiment can be followed by a single-wavelength reflectivity experiment using the existing hardware in combination with a TOPAS producing pulses in the visible spectrum. This is useful to fine-tune the excitation in a control-type experiment using the knowledge gained from the broadband data. Such an approach will greatly facilitate the further study of correlated systems, which will undoubtedly continue to occupy physicists for quite some time.

Bibliography

[Acocella et al., 2010] A. Acocella, F. Carbone, and F. Zerbetto. Quantum Study of Laser-Induced Initial Activation of Graphite-to-Diamond Conversion. *Journal of the American Chemical Society*, 132(35):12166–12167, Sept. 2010. ISSN 0002-7863. doi: 10.1021/ja102497z. URL http://dx.doi.org/10.1021/ja102497z.

[Albrecht et al., 1992] W. Albrecht, T. Kruse, and H. Kurz. Time-resolved observation of coherent phonons in superconducting $YBa_2Cu_3O_{7-\delta}$ thin films. *Physical Review Letters*, 69(9):1451–1454, Aug. 1992. doi: 10.1103/PhysRevLett.69.1451. URL http://link.aps.org/doi/10.1103/PhysRevLett.69.1451.

[Allen, 1987] P. B. Allen. Theory of thermal relaxation of electrons in metals. *Physical Review Letters*, 59(13):1460–1463, Sept. 1987. doi: 10.1103/PhysRevLett.59.1460. URL http://link.aps.org/doi/10.1103/PhysRevLett.59.1460.

[Andersen et al., 1995] O. K. Andersen, A. I. Liechtenstein, O. Jepsen, and F. Paulsen. LDA energy bands, low-energy hamiltonians, t', t'', $t^\perp$ (k), and $J^\perp$. *Journal of Physics and Chemistry of Solids*, 56(12):1573–1591, Dec. 1995. ISSN 0022-3697. doi: 10.1016/0022-3697(95)00269-3. URL http://www.sciencedirect.com/science/article/pii/0022369795002693.

[Anderson et al., 2004] P. Anderson, P. Lee, M. Randeria, T. Rice, N. Trivedi, and F. Zhang. The physics behind high-temperature superconducting cuprates: the 'plain vanilla' version of RVB. *Journal of Physics: Condensed Matter*, 16(24):R755, 2004.

[Anderson, 1958] P. W. Anderson. Random-phase approximation in the theory of superconductivity. *Physical Review*, 112(6):1900–1916, Dec. 1958. doi: 10.1103/PhysRev.112.1900. URL http://link.aps.org/doi/10.1103/PhysRev.112.1900.

[Anderson, 1987] P. W. Anderson. The Resonating Valence Bond State in La_2CuO_4 and Superconductivity. *Science*, 235(4793):1196–1198, June 1987. ISSN 0036-8075, 1095-9203. doi: 10.1126/science.235.4793.1196. URL http://www.sciencemag.org/content/235/4793/1196.

[Anderson, 2007] P. W. Anderson. Is there glue in cuprate superconductors? *Science*, 316(5832):1705–1707, June 2007. ISSN 0036-8075, 1095-9203. doi: 10.1126/science.1140970. URL http://www.sciencemag.org/content/316/5832/1705.

Bibliography

[Armitage, 2014] N. P. Armitage. Cuprate superconductors: Dynamic stabilization? *Nature Materials*, 13(7):665–666, July 2014. ISSN 1476-1122. doi: 10.1038/nmat3995. URL http://www.nature.com/nmat/journal/v13/n7/full/nmat3995.html.

[Azzam and Bashara, 1977] R. M. A. Azzam and N. M. Bashara. *Ellipsometry and Polarized Light*. North Holland, 1977.

[Bäckström et al., 2004] J. Bäckström, D. Budelmann, R. Rauer, M. Rübhausen, H. Rodriguez, and H. Adrian. Optical properties of YBa$_2$Cu$_3$O$_{7-\delta}$ and PrBa$_2$Cu$_3$O$_{7-\delta}$ films: High-energy correlations and metallicity. *Physical Review B*, 70(17):174502, 2004.

[Bardeen et al., 1957] J. Bardeen, L. N. Cooper, and J. R. Schrieffer. Theory of Superconductivity. *Physical Review*, 108(5):1175–1204, Dec. 1957. doi: 10.1103/PhysRev.108.1175. URL http://link.aps.org/doi/10.1103/PhysRev.108.1175.

[Barker et al., 1975] A. S. Barker, J. A. Ditzenberger, and F. J. DiSalvo. Infrared study of the electronic instabilities in tantalum disulfide and tantalum diselenide. *Physical Review B*, 12(6):2049–2054, Sept. 1975. doi: 10.1103/PhysRevB.12.2049. URL http://link.aps.org/doi/10.1103/PhysRevB.12.2049.

[Beck et al., 2011] M. Beck, M. Klammer, S. Lang, P. Leiderer, V. V. Kabanov, G. N. Gol'tsman, and J. Demsar. Energy-Gap Dynamics of Superconducting NbN Thin Films Studied by Time-Resolved Terahertz Spectroscopy. *Physical Review Letters*, 107(17):177007, Oct. 2011. doi: 10.1103/PhysRevLett.107.177007. URL http://link.aps.org/doi/10.1103/PhysRevLett.107.177007.

[Bednorz and Müller, 1986] J. G. Bednorz and K. A. Müller. Possible high T_c superconductivity in the Ba-La-Cu-O system. *Zeitschrift für Physik B Condensed Matter*, 64(2):189–193, June 1986. ISSN 0722-3277, 1431-584X. doi: 10.1007/BF01303701. URL http://link.springer.com/article/10.1007/BF01303701.

[Bernhard et al., 2004] C. Bernhard, J. Humlıćek, and B. Keimer. Far-infrared ellipsometry using a synchrotron light source–the dielectric response of the cuprate high T_c superconductors. *Thin Solid Films*, 455–456:143–149, May 2004. ISSN 0040-6090. doi: 10.1016/j.tsf.2004.01.002. URL http://www.sciencedirect.com/science/article/pii/S0040609004000033.

[Bogoliubov et al., 1959] N. Bogoliubov, V. Tolmachev, and D. Shirkov. *A New Method in the Theory of Superconductivity*, pages 34–44. Consultants Bureau, Inc., 1959.

[Boris et al., 2004] A. Boris, N. Kovaleva, O. Dolgov, T. Holden, C. Lin, B. Keimer, and C. Bernhard. In-plane spectral weight shift of charge carriers in YBa$_2$Cu$_3$O$_{6.9}$. *Science*, 304(5671):708–710, 2004.

[Bovet et al., 2003] M. Bovet, S. van Smaalen, H. Berger, R. Gaal, L. Forró, L. Schlapbach, and P. Aebi. Interplane coupling in the quasi-two-dimensional 1T-TaS$_2$. *Physical Review B*, 67(12):125105, Mar. 2003. doi: 10.1103/PhysRevB.67.125105. URL http://link.aps.org/doi/10.1103/PhysRevB.67.125105.

[Carbone, 2007] F. Carbone. *Spectroscopic signatures of electronic correlations in superconductors and magnets*. PhD thesis, University of Geneva, 2007.

[Carbone et al., 2006] F. Carbone, A. Kuzmenko, H. J. Molegraaf, E. Van Heumen, V. Lukovac, F. Marsiglio, D. Van Der Marel, K. Haule, G. Kotliar, H. Berger, et al. Doping dependence of the redistribution of optical spectral weight in $Bi_2Sr_2CaCu_2O_{8+\delta}$. *Physical Review B*, 74(6): 064510, 2006.

[Carbone et al., 2008] F. Carbone, D.-S. Yang, E. Giannini, and A. H. Zewail. Direct role of structural dynamics in electron-lattice coupling of superconducting cuprates. *Proceedings of the National Academy of Sciences*, 105(51):20161–20166, Dec. 2008. ISSN 0027-8424, 1091-6490. doi: 10.1073/pnas.0811335106. URL http://www.pnas.org/content/105/51/20161.

[Carbone et al., 2010] F. Carbone, N. Gedik, J. Lorenzana, and A. H. Zewail. Real-time observation of cuprates structural dynamics by ultrafast electron crystallography. *Advances in Condensed Matter Physics*, 2010:e958618, Mar. 2010. ISSN 1687-8108. doi: 10.1155/2010/958618. URL http://www.hindawi.com/journals/acmp/2010/958618/abs/.

[Cardona and Güntherodt, 1982] M. Cardona and G. Güntherodt, editors. *Light Scattering in Solids II*, volume 50 of *Topics in Applied Physics*. Springer, 1982. ISBN 978-3-540-11380-5.

[Casandruc et al., 2015] E. Casandruc, D. Nicoletti, S. Rajasekaran, Y. Laplace, V. Khanna, G. D. Gu, J. P. Hill, and A. Cavalleri. Wavelength-dependent optical enhancement of superconducting interlayer coupling in $La_{1.885}Ba_{0.115}CuO_4$. *Physical Review B*, 91(17):174502, May 2015. doi: 10.1103/PhysRevB.91.174502. URL http://link.aps.org/doi/10.1103/PhysRevB.91.174502.

[Cavalleri et al., 2001] A. Cavalleri, C. Tóth, C. W. Siders, J. A. Squier, F. Ráksi, P. Forget, and J. C. Kieffer. Femtosecond Structural Dynamics in VO_2 during an Ultrafast Solid-Solid Phase Transition. *Physical Review Letters*, 87(23):237401, Nov. 2001. doi: 10.1103/PhysRevLett.87. 237401. URL http://link.aps.org/doi/10.1103/PhysRevLett.87.237401.

[Chang et al., 2012] J. Chang, E. Blackburn, A. Holmes, N. Christensen, J. Larsen, J. Mesot, R. Liang, D. Bonn, W. Hardy, A. Watenphul, et al. Direct observation of competition between superconductivity and charge density wave order in $YBa_2Cu_3O_{6.67}$. *Nature Physics*, 8(12):871–876, 2012.

[Chen et al., 1992] C. T. Chen, L. H. Tjeng, J. Kwo, H. L. Kao, P. Rudolf, F. Sette, and R. M. Fleming. Out-of-plane orbital characters of intrinsic and doped holes in $La_{2-x}Sr_xCuO_4$. *Physical Review Letters*, 68(16):2543–2546, Apr. 1992. doi: 10.1103/PhysRevLett.68.2543. URL http://link.aps.org/doi/10.1103/PhysRevLett.68.2543.

[Chubukov and Schmalian, 1998] A. V. Chubukov and J. Schmalian. Temperature variation of the pseudogap in underdoped cuprates. *Physical Review B*, 57(18):R11085, 1998.

[Cilento et al., 2014] F. Cilento, S. Dal Conte, G. Coslovich, S. Peli, N. Nembrini, S. Mor, F. Banfi, G. Ferrini, H. Eisaki, M. K. Chan, et al. Photo-enhanced antinodal conductivity in the pseudogap state of high-T_c cuprates. *Nature communications*, 5, 2014.

Bibliography

[Cooper et al., 1993] S. Cooper, D. Reznik, A. Kotz, M. Karlow, R. Liu, M. Klein, W. Lee, J. Giapintzakis, D. Ginsberg, B. Veal, et al. Optical studies of the *a*-, *b*-, and *c*-axis charge dynamics in $YBa_2Cu_3O_{6+x}$. *Physical Review B*, 47(13):8233, 1993.

[Cortés et al., 2011] R. Cortés, L. Rettig, Y. Yoshida, H. Eisaki, M. Wolf, and U. Bovensiepen. Momentum-resolved ultrafast electron dynamics in superconducting $Bi_2Sr_2CaCu_2O_{8+\delta}$. *Physical Review Letters*, 107(9):097002, Aug. 2011. doi: 10.1103/PhysRevLett.107.097002. URL http://link.aps.org/doi/10.1103/PhysRevLett.107.097002.

[Damascelli et al., 2003] A. Damascelli, Z. Hussain, and Z.-X. Shen. Angle-resolved photoemission studies of the cuprate superconductors. *Reviews of Modern Physics*, 75(2):473–541, Apr. 2003. doi: 10.1103/RevModPhys.75.473. URL http://link.aps.org/doi/10.1103/RevModPhys.75. 473.

[Dardel et al., 1992] B. Dardel, M. Grioni, D. Malterre, P. Weibel, Y. Baer, and F. Lévy. Temperature-dependent pseudogap and electron localization in $1T$-TaS_2. *Physical Review B*, 45(3): 1462–1465, Jan. 1992. doi: 10.1103/PhysRevB.45.1462. URL http://link.aps.org/doi/10.1103/ PhysRevB.45.1462.

[Dean, 2010] N. Dean. *Electronic and Structural Dynamics of Complex Materials*. PhD thesis, University of Oxford, 2010.

[Dean et al., 2011] N. Dean, J. C. Petersen, D. Fausti, R. I. Tobey, S. Kaiser, L. V. Gasparov, H. Berger, and A. Cavalleri. Polaronic Conductivity in the Photoinduced Phase of $1T$-TaS_2. *Physical Review Letters*, 106(1):016401, Jan. 2011. doi: 10.1103/PhysRevLett.106.016401. URL http: //link.aps.org/doi/10.1103/PhysRevLett.106.016401.

[Demsar et al., 1999] J. Demsar, B. Podobnik, V. Kabanov, T. Wolf, and D. Mihailovic. Super-conducting Gap Δ_c, the Pseudogap Δ_p, and Pair Fluctuations above T_c in Overdoped $Y_{1-x}Ca_xBa_2Cu_3O_{7-\delta}$ from Femtosecond Time-Domain Spectroscopy. *Physical Review Letters*, 82(24):4918, 1999.

[Demsar et al., 2002] J. Demsar, L. Forró, H. Berger, and D. Mihailovic. Femtosecond snapshots of gap-forming charge-density-wave correlations in quasi-two-dimensional dichalcogenides $1T$-TaS_2 and $1H$-$TaSe_2$. *Physical Review B*, 66(4):041101, June 2002. doi: 10.1103/PhysRevB. 66.041101. URL http://link.aps.org/doi/10.1103/PhysRevB.66.041101.

[Denny et al., 2015] S. J. Denny, S. R. Clark, Y. Laplace, A. Cavalleri, and D. Jaksch. Proposed Parametric Cooling of Bilayer Cuprate Superconductors by Terahertz Excitation. *Physical Review Letters*, 114(13):137001, Mar. 2015. doi: 10.1103/PhysRevLett.114.137001. URL http://link.aps.org/doi/10.1103/PhysRevLett.114.137001.

[Devereaux and Hackl, 2007] T. P. Devereaux and R. Hackl. Inelastic light scattering from correlated electrons. *Reviews of Modern Physics*, 79(1):175–233, Jan. 2007. doi: 10.1103/RevModPhys. 79.175. URL http://link.aps.org/doi/10.1103/RevModPhys.79.175.

[Dressel and Grüner, 2002] M. Dressel and G. Grüner. *Electrodynamics of Solids: Optical Properties of Electrons in Matter*. Cambridge University Press, 2002. ISBN 9780521597265.

[Dubroka et al., 2011] A. Dubroka, M. Rössle, K. W. Kim, V. K. Malik, D. Munzar, D. N. Basov, A. A. Schafgans, S. J. Moon, C. T. Lin, D. Haug, V. Hinkov, B. Keimer, T. Wolf, J. G. Storey, J. L. Tallon, and C. Bernhard. Evidence of a Precursor Superconducting Phase at Temperatures as High as 180 K in RBa$_2$Cu$_3$O$_{7-\delta}$ (R = Y, Gd, Eu) Superconducting Crystals from Infrared Spectroscopy. *Physical Review Letters*, 106(4):047006, Jan. 2011. doi: 10.1103/PhysRevLett.106.047006. URL http://link.aps.org/doi/10.1103/PhysRevLett.106.047006.

[Duffey et al., 1976] J. R. Duffey, R. D. Kirby, and R. V. Coleman. Raman scattering from 1T-TaS$_2$. *Solid State Communications*, 20(6):617–621, Nov. 1976. ISSN 0038-1098. doi: 10.1016/0038-1098(76)91073-5. URL http://www.sciencedirect.com/science/article/pii/0038109876910735.

[Ebrahimnejad et al., 2014] H. Ebrahimnejad, G. A. Sawatzky, and M. Berciu. The dynamics of a doped hole in a cuprate is not controlled by spin fluctuations. *Nature Physics*, 10(12):951–955, Dec. 2014. ISSN 1745-2473. doi: 10.1038/nphys3130. URL http://www.nature.com/nphys/journal/v10/n12/abs/nphys3130.html.

[Eichberger et al., 2010] M. Eichberger, H. Schäfer, M. Krumova, M. Beyer, J. Demsar, H. Berger, G. Moriena, G. Sciaini, and R. J. D. Miller. Snapshots of cooperative atomic motions in the optical suppression of charge density waves. *Nature*, 468(7325):799–802, Dec. 2010. ISSN 0028-0836. doi: 10.1038/nature09539. URL http://www.nature.com/nature/journal/v468/n7325/full/nature09539.html.

[Eliashberg, 1960] G. M. Eliashberg. Interactions between electrons and lattice vibrations in a superconductor. *Sov. Phys. - JETP (Engl. Transl.); (United States)*, 11:3, Sept. 1960. URL http://www.osti.gov/scitech/biblio/7354388.

[Ellis et al., 2008] D. S. Ellis, J. P. Hill, S. Wakimoto, R. J. Birgeneau, D. Casa, T. Gog, and Y.-J. Kim. Charge-transfer exciton in La$_2$CuO$_4$ probed with resonant inelastic x-ray scattering. *Physical Review B*, 77(6):060501, Feb. 2008. doi: 10.1103/PhysRevB.77.060501. URL http://link.aps.org/doi/10.1103/PhysRevB.77.060501.

[Emery and Kivelson, 1995] V. Emery and S. Kivelson. Importance of phase fluctuations in super-conductors with small superfluid density. *Nature*, 374(6521):434–437, 1995.

[Emery, 1987] V. J. Emery. Theory of high-T$_c$ superconductivity in oxides. *Physical Review Letters*, 58(26):2794–2797, June 1987. doi: 10.1103/PhysRevLett.58.2794. URL http://link.aps.org/doi/10.1103/PhysRevLett.58.2794.

[Eskes and Sawatzky, 1988] H. Eskes and G. A. Sawatzky. Tendency towards Local Spin Compensation of Holes in the High-T_c Copper Compounds. *Physical Review Letters*, 61(12):1415–1418, Sept. 1988. doi: 10.1103/PhysRevLett.61.1415. URL http://link.aps.org/doi/10.1103/PhysRevLett.61.1415.

Bibliography

[Falck et al., 1992] J. P. Falck, A. Levy, M. A. Kastner, and R. J. Birgeneau. Charge-transfer spectrum and its temperature dependence in La_2CuO_4. *Physical Review Letters*, 69(7):1109–1112, Aug. 1992. doi: 10.1103/PhysRevLett.69.1109. URL http://link.aps.org/doi/10.1103/PhysRevLett. 69.1109.

[Falter and Schnetgöke, 2002] C. Falter and F. Schnetgöke. Influence of ionic charge and dipole fluctuations on the lattice dynamics, dielectric properties, and infrared response of La_2CuO_4. *Physical Review B*, 65(5):054510, Jan. 2002. doi: 10.1103/PhysRevB.65.054510. URL http: //link.aps.org/doi/10.1103/PhysRevB.65.054510.

[Fausti et al., 2011] D. Fausti, R. Tobey, N. Dean, S. Kaiser, A. Dienst, M. Hoffmann, S. Pyon, T. Takayama, H. Takagi, and A. Cavalleri. Light-induced superconductivity in a stripe-ordered cuprate. *Science*, 331(6014):189–191, 2011.

[Fausti et al., 2014] D. Fausti, F. Novelli, G. Giovannetti, A. Avella, F. Cilento, L. Patthey, M. Radovic, M. Capone, and F. Parmigiani. Dynamical coupling between off-plane phonons and in-plane electronic excitations in superconducting YBCO. *arXiv:1408.0888 [cond-mat]*, Aug. 2014. URL http://arxiv.org/abs/1408.0888.

[Fazekas and Tosatti, 1979] P. Fazekas and E. Tosatti. Electrical, structural and magnetic properties of pure and doped $1T$-TaS_2. *Philosophical Magazine Part B*, 39(3):229–244, Mar. 1979. ISSN 1364-2812. doi: 10.1080/13642817908245359. URL http://dx.doi.org/10.1080/ 13642817908245359.

[Fazekas and Tosatti, 1980] P. Fazekas and E. Tosatti. Charge carrier localization in pure and doped $1T$-TaS_2. *Physica B+C*, 99(1–4):183–187, Jan. 1980. ISSN 0378-4363. doi: 10.1016/0378-4363(80)90229-6. URL http://www.sciencedirect.com/science/article/pii/ 0378436380902296.

[Ferrell and Glover, 1958] R. A. Ferrell and R. E. Glover. Conductivity of Superconducting Films: A Sum Rule. *Physical Review*, 109(4):1398–1399, Feb. 1958. doi: 10.1103/PhysRev.109.1398. URL http://link.aps.org/doi/10.1103/PhysRev.109.1398.

[Först et al., 2014] M. Först, A. Frano, S. Kaiser, R. Mankowsky, C. Hunt, J. Turner, G. Dakovski, M. Minitti, J. Robinson, T. Loew, et al. Femtosecond x rays link melting of charge-density wave correlations and light-enhanced coherent transport in $YBa_2Cu_3O_{6.6}$. *Physical Review B*, 90(18):184514, 2014. doi: 10.1103/PhysRevB.90.184514.

[Garrett et al., 1996] G. A. Garrett, T. F. Albrecht, J. F. Whitaker, and R. Merlin. Coherent THz Phonons Driven by Light Pulses and the Sb Problem: What is the Mechanism? *Physical Review Letters*, 77(17):3661–3664, Oct. 1996. doi: 10.1103/PhysRevLett.77.3661. URL http://link.aps.org/ doi/10.1103/PhysRevLett.77.3661.

[Gedik et al., 2004] N. Gedik, P. Blake, R. Spitzer, J. Orenstein, R. Liang, D. Bonn, and W. Hardy. Single-quasiparticle stability and quasiparticle-pair decay in $YBa_2Cu_3O_{6.5}$. *Physical Review B*, 70(1):014504, 2004.

[Gedik et al., 2005] N. Gedik, M. Langner, J. Orenstein, S. Ono, Y. Abe, and Y. Ando. Abrupt Transition in Quasiparticle Dynamics at Optimal Doping in a Cuprate Superconductor System. *Physical Review Letters*, 95(11):117005, Sept. 2005. doi: 10.1103/PhysRevLett.95.117005. URL http://link.aps.org/doi/10.1103/PhysRevLett.95.117005.

[Giannetti et al., 2009] C. Giannetti, G. Coslovich, F. Cilento, G. Ferrini, H. Eisaki, N. Kaneko, M. Greven, and F. Parmigiani. Discontinuity of the ultrafast electronic response of underdoped superconducting $Bi_2Sr_2CaCu_2O_{8+\delta}$ strongly excited by ultrashort light pulses. *Physical Review B*, 79(22):224502, June 2009. doi: 10.1103/PhysRevB.79.224502. URL http://link.aps.org/doi/10.1103/PhysRevB.79.224502.

[Giannetti et al., 2011] C. Giannetti, F. Cilento, S. D. Conte, G. Coslovich, G. Ferrini, H. Molegraaf, M. Raichle, R. Liang, H. Eisaki, M. Greven, A. Damascelli, D. van der Marel, and F. Parmigiani. Revealing the high-energy electronic excitations underlying the onset of high-temperature superconductivity in cuprates. *Nature Communications*, 2:353, June 2011. doi: 10.1038/ ncomms1354. URL http://www.nature.com/ncomms/journal/v2/n6/full/ncomms1354. html.

[Grüninger, 1999] M. Grüninger. *Of spin and charge in the cuprates.* PhD thesis, University of Geneva, 1999.

[Ham, 2011] *CMOS linear image sensors, S10111 to S10114 series.* Hamamatsu Photonics K.K., Solid State Division, May 2011. Cat. No. KMPD1090E08.

[Han et al., 1990] S. Han, Z. Vardeny, K. Wong, O. Symko, and G. Koren. Femtosecond optical detection of quasiparticle dynamics in high-T_c $YBa_2Cu_3O_{7-\delta}$ superconducting thin films. *Physical Review Letters*, 65(21):2708, 1990.

[Hashimoto et al., 2015] M. Hashimoto, E. A. Nowadnick, R.-H. He, I. M. Vishik, B. Moritz, Y. He, K. Tanaka, R. G. Moore, D. Lu, Y. Yoshida, M. Ishikado, T. Sasagawa, K. Fujita, S. Ishida, S. Uchida, H. Eisaki, Z. Hussain, T. P. Devereaux, and Z.-X. Shen.   Direct spectroscopic evidence for phase competition between the pseudogap and superconductivity in $Bi_2Sr_2CaCu_2O_{8+\delta}$. *Nature Materials*, 14(1):37–42, Jan. 2015. ISSN 1476-1122. doi: 10. 1038/nmat4116. URL http://www.nature.com/nmat/journal/v14/n1/abs/nmat4116.html.

[Heyen et al., 1990] E. T. Heyen, S. N. Rashkeev, I. I. Mazin, O. K. Andersen, R. Liu, M. Cardona, and O. Jepsen. Resonant raman scattering in $YBa_2Cu_3O_7$: Band theory and experiment. *Physical Review Letters*, 65:3048–3051, Dec 1990. doi: 10.1103/PhysRevLett.65.3048. URL http://link.aps.org/doi/10.1103/PhysRevLett.65.3048.

[Hilton et al., 2007] D. J. Hilton, R. P. Prasankumar, S. Fourmaux, A. Cavalleri, D. Brassard, M. A. El Khakani, J. C. Kieffer, A. J. Taylor, and R. D. Averitt. Enhanced Photosusceptibility near T_c for the Light-Induced Insulator-to-Metal Phase Transition in Vanadium Dioxide. *Physical Review Letters*, 99(22):226401, Nov. 2007. doi: 10.1103/PhysRevLett.99.226401. URL http://link.aps.org/doi/10.1103/PhysRevLett.99.226401.

Bibliography

[Holcomb et al., 1996] M. Holcomb, C. Perry, J. Collman, and W. Little. Thermal-difference reflectance spectroscopy of the high-temperature cuprate superconductors. *Physical Review B*, 53(10):6734, 1996.

[Howell et al., 2004] P. C. Howell, A. Rosch, and P. J. Hirschfeld. Relaxation of hot quasiparticles in a *d*-wave superconductor. *Physical Review Letters*, 92(3):037003, Jan. 2004. doi: 10.1103/ PhysRevLett.92.037003. URL http://link.aps.org/doi/10.1103/PhysRevLett.92.037003.

[Hu et al., 2014] W. Hu, S. Kaiser, D. Nicoletti, C. Hunt, I. Gierz, M. Hoffmann, M. Le Tacon, T. Loew, B. Keimer, and A. Cavalleri. Optically enhanced coherent transport in $YBa_2Cu_3O_{6.5}$ by ultrafast redistribution of interlayer coupling. *Nature materials*, 13(7):705–711, 2014.

[Humlíček and Bernhard, 2004] J. Humlíček and C. Bernhard. Diffraction effects in infrared ellipsometry of conducting samples. *Thin Solid Films*, 455–456:177–182, May 2004. ISSN 0040-6090. doi: 10.1016/j.tsf.2004.01.004. URL http://www.sciencedirect.com/science/ article/pii/S0040609004000057.

[Kabanov et al., 2005] V. V. Kabanov, J. Demsar, and D. Mihailovic. Kinetics of a Superconductor Excited with a Femtosecond Optical Pulse. *Physical Review Letters*, 95(14):147002, Sept. 2005. doi: 10.1103/PhysRevLett.95.147002. URL http://link.aps.org/doi/10.1103/PhysRevLett.95. 147002.

[Kaindl et al., 2000] R. A. Kaindl, M. Woerner, T. Elsaesser, D. C. Smith, J. F. Ryan, G. A. Farnan, M. P. McCurry, and D. G. Walmsley. Ultrafast mid-infrared response of $YBa_2Cu_3O_{7-\delta}$. *Science*, 287 (5452):470–473, Jan. 2000. ISSN 0036-8075, 1095-9203. doi: 10.1126/science.287.5452.470. URL http://www.sciencemag.org/content/287/5452/470.

[Kaiser et al., 2014] S. Kaiser, C. Hunt, D. Nicoletti, W. Hu, I. Gierz, H. Liu, M. Le Tacon, T. Loew, D. Haug, B. Keimer, et al. Optically induced coherent transport far above T_c in underdoped $YBa_2Cu_3O_{6+\delta}$. *Physical Review B*, 89(18):184516, 2014.

[Kamerlingh Onnes, 1911] H. Kamerlingh Onnes. Commun. Phys. Lab. Univ. Leiden. Suppl. 29, November 1911.

[Kanigel et al., 2008] A. Kanigel, U. Chatterjee, M. Randeria, M. Norman, G. Koren, K. Kadowaki, and J. Campuzano. Evidence for pairing above the transition temperature of cuprate superconductors from the electronic dispersion in the pseudogap phase. *Physical Review Letters*, 101(13):137002, 2008.

[Kastner et al., 1998] M. A. Kastner, R. J. Birgeneau, G. Shirane, and Y. Endoh. Magnetic, transport, and optical properties of monolayer copper oxides. *Reviews of Modern Physics*, 70(3):897– 928, July 1998. doi: 10.1103/RevModPhys.70.897. URL http://link.aps.org/doi/10.1103/ RevModPhys.70.897.

[Kim et al., 1994] J.-J. Kim, W. Yamaguchi, T. Hasegawa, and K. Kitazawa. Observation of Mott Localization Gap Using Low Temperature Scanning Tunneling Spectroscopy in Commensurate

$1T$-TaS$_2$. *Physical Review Letters*, 73(15):2103–2106, Oct. 1994. doi: 10.1103/PhysRevLett.73. 2103. URL http://link.aps.org/doi/10.1103/PhysRevLett.73.2103.

[Kircher et al., 1991] J. Kircher, M. K. Kelly, S. Rashkeev, M. Alouani, D. Fuchs, and M. Cardona. Anisotropy and oxygen-stoichiometry dependence of the dielectric tensor of YBa$_2$Cu$_3$O$_{7-\delta}$ ($0 \leq \delta \leq 1$). *Physical Review B*, 44(1):217–224, July 1991. doi: 10.1103/PhysRevB.44.217. URL http://link.aps.org/doi/10.1103/PhysRevB.44.217.

[Knoll and Ambrosch-Draxl, 1995] P. Knoll and C. Ambrosch-Draxl. Raman scattering of atomic vibrations in anharmonic potentials. In D. Mihailovich, G. Ruani, E. Kaldis, and K. A. Müller, editors, *Proceedings of the International Workshop on Anharmonic Properties of High-Tc Cuprates*, page 220. World Scientific, 1995.

[Knorren et al., 2000] R. Knorren, K. H. Bennemann, R. Burgermeister, and M. Aeschlimann. Dynamics of excited electrons in copper and ferromagnetic transition metals: Theory and experiment. *Physical Review B*, 61(14):9427–9440, Apr. 2000. doi: 10.1103/PhysRevB.61.9427. URL http://link.aps.org/doi/10.1103/PhysRevB.61.9427.

[Koopmans, 2003] B. Koopmans. Laser-Induced Magnetization Dynamics. In B. Hillebrands and K. Ounadjela, editors, *Spin Dynamics in Confined Magnetic Structures I*, volume 87 of *Topics in applied physics*, pages 256–323. Springer, 2003. URL http://dx.doi.org/10.1007/ 3-540-46097-7_8.

[Koopmans et al., 2010] B. Koopmans, G. Malinowski, F. Dalla Longa, D. Steiauf, M. Fähnle, T. Roth, M. Cinchetti, and M. Aeschlimann. Explaining the paradoxical diversity of ultrafast laser-induced demagnetization. *Nature Materials*, 9(3):259–265, Mar. 2010. ISSN 1476-1122. doi: 10.1038/nmat2593. URL http://www.nature.com/nmat/journal/v9/n3/abs/nmat2593. html.

[Kosztin et al., 2000] I. Kosztin, Q. Chen, Y.-J. Kao, and K. Levin. Pair excitations, collective modes, and gauge invariance in the BCS–Bose-Einstein crossover scenario. *Physical Review B*, 61 (17):11662–11675, May 2000. doi: 10.1103/PhysRevB.61.11662. URL http://link.aps.org/doi/ 10.1103/PhysRevB.61.11662.

[Kudryashov et al., 2007] S. I. Kudryashov, M. Kandyla, C. A. D. Roeser, and E. Mazur. Intraband and interband optical deformation potentials in femtosecond-laser-excited α-Te. *Physical Review B*, 75(8):085207, Feb. 2007. doi: 10.1103/PhysRevB.75.085207. URL http://link.aps. org/doi/10.1103/PhysRevB.75.085207.

[Kuzmenko, 2014] A. Kuzmenko. *Guide to RefFIT*. University of Geneva, 1.2.89 edition, February 2014. URL http://optics.unige.ch/alexey/reffit.html.

[Landau et al., 1980] L. D. Landau, E. M. Lifshitz, and L. P. Pitaevskij. *Statistical Physics*. Butterworth-Heinemann, Jan. 1980. ISBN 9780750626361.

Bibliography

[Lau et al., 2011] B. Lau, M. Berciu, and G. A. Sawatzky. High-Spin Polaron in Lightly Doped CuO_2 Planes. *Physical Review Letters*, 106(3):036401, Jan. 2011. doi: 10.1103/PhysRevLett.106.036401. URL http://link.aps.org/doi/10.1103/PhysRevLett.106.036401.

[Li et al., 2013] J. J. Li, J. Chen, D. A. Reis, S. Fahy, and R. Merlin. Optical Probing of Ultrafast Electronic Decay in Bi and Sb with Slow Phonons. *Physical Review Letters*, 110(4):047401, Jan. 2013. doi: 10.1103/PhysRevLett.110.047401. URL http://link.aps.org/doi/10.1103/PhysRevLett.110.047401.

[Lorenzana and Seibold, 2003] J. Lorenzana and G. Seibold. Dynamics of metallic stripes in cuprates. *Physical Review Letters*, 90(6):066404, Feb. 2003. doi: 10.1103/PhysRevLett.90.066404. URL http://link.aps.org/doi/10.1103/PhysRevLett.90.066404.

[Lorenzana et al., 2013] J. Lorenzana, B. Mansart, A. Mann, A. Odeh, M. Chergui, and F. Carbone. Investigating pairing interactions with coherent charge fluctuation spectroscopy. *The European Physical Journal Special Topics*, 222(5):1223–1239, July 2013. ISSN 1951-6355, 1951-6401. doi: 10.1140/epjst/e2013-01917-9. URL http://link.springer.com/article/10.1140/epjst/e2013-01917-9.

[Mahan, 1990] G. Mahan. *Many-Particle Physics*. Physics of Solids and Liquids. Springer, 2nd edition, 1990. ISBN 9780306463389. doi: 10.1007/978-1-4613-1469-1.

[Maier et al., 2008] T. A. Maier, D. Poilblanc, and D. J. Scalapino. Dynamics of the pairing interaction in the hubbard and t-j models of high-temperature superconductors. *Physical Review Letters*, 100(23):237001, June 2008. doi: 10.1103/PhysRevLett.100.237001. URL http://link.aps.org/doi/10.1103/PhysRevLett.100.237001.

[Mann et al., 2015] A. Mann, E. Baldini, A. Tramontana, E. Pomjakushina, K. Conder, C. Arrell, F. van Mourik, J. Lorenzana, and F. Carbone. Probing the electron-phonon interaction in correlated systems with coherent lattice fluctuation spectroscopy. *Physical Review B*, 92(3):035147, July 2015. doi: 10.1103/PhysRevB.92.035147. URL http://link.aps.org/doi/10.1103/PhysRevB.92.035147.

[Mansart et al., 2012] B. Mansart, M. J. G. Cottet, T. J. Penfold, S. B. Dugdale, R. Tediosi, M. Chergui, and F. Carbone. Evidence for a peierls phase-transition in a three-dimensional multiple charge-density waves solid. *Proceedings of the National Academy of Sciences*, 109(15):5603–5608, Oct. 2012. ISSN 0027-8424, 1091-6490. doi: 10.1073/pnas.1117028109. URL http://www.pnas.org/content/109/15/5603.

[Mansart et al., 2013] B. Mansart, J. Lorenzana, A. Mann, A. Odeh, M. Scarongella, M. Chergui, and F. Carbone. Coupling of a high-energy excitation to superconducting quasiparticles in a cuprate from coherent charge fluctuation spectroscopy. *Proceedings of the National Academy of Sciences*, 110(12):4539–4544, Mar. 2013. ISSN 0027-8424, 1091-6490. doi: 10.1073/pnas.1218742110. URL http://www.pnas.org/content/110/12/4539.

[Marshall et al., 1996] D. S. Marshall, D. S. Dessau, A. G. Loeser, C.-H. Park, A. Y. Matsuura, J. N. Eckstein, I. Bozovic, P. Fournier, A. Kapitulnik, W. E. Spicer, and Z.-X. Shen. Unconventional Electronic Structure Evolution with Hole Doping in $Bi_2Sr_2CaCu_2O_{8+\delta}$: Angle-Resolved Photoemission Results. *Physical Review Letters*, 76(25):4841–4844, June 1996. doi: 10.1103/PhysRevLett.76.4841. URL http://link.aps.org/doi/10.1103/PhysRevLett.76.4841.

[Martinez et al., 1984] O. E. Martinez, R. L. Fork, and J. P. Gordon. Theory of passively mode-locked lasers including self-phase modulation and group-velocity dispersion. *Optics Letters*, 9 (5):156, May 1984. ISSN 0146-9592, 1539-4794. doi: 10.1364/OL.9.000156. URL http://www.opticsinfobase.org/abstract.cfm?URI=ol-9-5-156.

[Matsunaga et al., 2014] R. Matsunaga, N. Tsuji, H. Fujita, A. Sugioka, K. Makise, Y. Uzawa, H. Terai, Z. Wang, H. Aoki, and R. Shimano. Light-induced collective pseudospin precession resonating with Higgs mode in a superconductor. *Science*, 345(6201):1145–1149, May 2014. ISSN 0036-8075, 1095-9203. doi: 10.1126/science.1254697. URL http://www.sciencemag.org/content/345/6201/1145.

[Maxwell, 1950] E. Maxwell. Isotope Effect in the Superconductivity of Mercury. *Physical Review*, 78 (4):477–477, May 1950. doi: 10.1103/PhysRev.78.477. URL http://link.aps.org/doi/10.1103/PhysRev.78.477.

[Mazin et al., 1994] I. I. Mazin, A. I. Liechtenstein, O. Jepsen, O. K. Andersen, and C. O. Rodriguez. Displacive excitation of coherent phonons in $YBa_2Cu_3O_7$. *Physical Review B*, 49(13):9210–9213, Apr. 1994. doi: 10.1103/PhysRevB.49.9210. URL http://link.aps.org/doi/10.1103/PhysRevB.49.9210.

[McMillan, 1975] W. L. McMillan. Landau theory of charge-density waves in transition-metal dichalcogenides. *Physical Review B*, 12(4):1187–1196, Aug. 1975. doi: 10.1103/PhysRevB.12.1187. URL http://link.aps.org/doi/10.1103/PhysRevB.12.1187.

[Meissner and Ochsenfeld, 1933] W. Meissner and R. Ochsenfeld. Ein neuer Effekt bei Eintritt der Supraleitfähigkeit. *Naturwissenschaften*, 21(44):787–788, Nov. 1933. ISSN 0028-1042, 1432-1904. doi: 10.1007/BF01504252. URL http://link.springer.com/article/10.1007/BF01504252.

[Merlin, 1997] R. Merlin. Generating coherent THz phonons with light pulses. *Solid State Communications*, 102(2–3):207–220, Apr. 1997. ISSN 0038-1098. doi: 10.1016/S0038-1098(96)00721-1. URL http://www.sciencedirect.com/science/article/pii/S0038109896007211.

[Mihailovic et al., 1998] D. Mihailovic, B. Podobnik, J. Demsar, G. Wagner, and J. Evetts. Divergence of the quasiparticle lifetime with doping and evidence for pre-formed pairs below T* in $YBa_2Cu_3O_{7-\delta}$: Direct measurements by femtosecond time-resolved spectroscopy. *Journal of Physics and Chemistry of Solids*, 59(10):1937–1941, 1998.

[Mihailovic et al., 2000] D. Mihailovic, J. Demsar, R. Hudej, V. V. Kabanov, T. Wolf, and J. Karpinski. Quasiparticle relaxation dynamics in cuprates and lifetimes of low-energy states: Femtosecond data from underdoped to overdoped YBCO and mercury compounds. *Physica C: Superconductivity*, 341:1731–1734, 2000.

[Misochko et al., 2000] O. V. Misochko, K. Kisoda, K. Sakai, and S. Nakashima. Dynamics of low-frequency phonons in the $YBa_2Cu_3O_{7-x}$ superconductor studied by time- and frequency-domain spectroscopies. *Physical Review B*, 61(6):4305–4313, Feb. 2000. doi: 10.1103/PhysRevB.61.4305. URL http://link.aps.org/doi/10.1103/PhysRevB.61.4305.

[Misochko et al., 2002] O. V. Misochko, N. Georgiev, T. Dekorsy, and M. Helm. Two Crossovers in the Pseudogap Regime of $YBa_2Cu_3O_{7-\delta}$ Superconductors Observed by Ultrafast Spectroscopy. *Physical review letters*, 89(6):067002, 2002.

[Misochko et al., 2004] O. V. Misochko, M. Lebedev, N. Georgiev, and T. Dekorsy. Coherent phonons in $NdBa_2Cu_3O_{7-x}$ single crystals: Optical-response anisotropy and hysteretic behavior. *Journal of Experimental and Theoretical Physics*, 98(2):341–347, 2004.

[Molegraaf et al., 2002] H. Molegraaf, C. Presura, D. Van Der Marel, P. Kes, and M. Li. Superconductivity-induced transfer of in-plane spectral weight in $Bi_2Sr_2CaCu_2O_{8+\delta}$. *Science*, 295(5563):2239–2241, 2002.

[Mostoller et al., 1990] M. Mostoller, J. Zhang, A. M. Rao, and P. C. Eklund. Lattice vibrations in La_2CuO_4. *Physical Review B*, 41(10):6488–6499, Apr. 1990. doi: 10.1103/PhysRevB.41.6488. URL http://link.aps.org/doi/10.1103/PhysRevB.41.6488.

[Mott, 1968] N. F. Mott. Metal-Insulator Transition. *Reviews of Modern Physics*, 40(4):677–683, Oct. 1968. doi: 10.1103/RevModPhys.40.677. URL http://link.aps.org/doi/10.1103/RevModPhys.40.677.

[Novelli et al., 2014] F. Novelli, G. De Filippis, V. Cataudella, M. Esposito, I. Vergara, F. Cilento, E. Sindici, A. Amaricci, C. Giannetti, D. Prabhakaran, S. Wall, A. Perucchi, S. Dal Conte, G. Cerullo, M. Capone, A. Mishchenko, M. Grüninger, N. Nagaosa, F. Parmigiani, and D. Fausti. Witnessing the formation and relaxation of dressed quasi-particles in a strongly correlated electron system. *Nature Communications*, 5, Oct. 2014. doi: 10.1038/ncomms6112. URL http://www.nature.com/ncomms/2014/141007/ncomms6112/abs/ncomms6112.html.

[Onozaki et al., 2007] T. Onozaki, Y. Toda, S. Tanda, and R. Morita. Coherent Double-Pulse Excitation of Charge-Density-Wave Oscillation. *Japanese Journal of Applied Physics*, 46(2R):870, Feb. 2007. ISSN 1347-4065. doi: 10.1143/JJAP.46.870. URL http://iopscience.iop.org/1347-4065/46/2R/870.

[Orenstein, 2006] J. Orenstein. Josephson plasmons: The new wave. *Nature Physics*, 2(8):503–504, Aug. 2006. ISSN 1745-2473. doi: 10.1038/nphys376. URL http://www.nature.com/nphys/journal/v2/n8/full/nphys376.html.

[Orenstein, 2012] J. Orenstein. ultrafast spectroscopy of quantum materials. *Physics Today*, 65(9): 44–50, Sept. 2012. ISSN 0031-9228. WOS:000308622100010.

[Parmenter, 1965] R. H. Parmenter. Time- and position-dependent superconductivity. *Physical Review*, 137(1A):A161–A163, Jan. 1965. doi: 10.1103/PhysRev.137.A161. URL http://link.aps.org/doi/10.1103/PhysRev.137.A161.

[Pashkin et al., 2010] A. Pashkin, M. Porer, M. Beyer, K. W. Kim, A. Dubroka, C. Bernhard, X. Yao, Y. Dagan, R. Hackl, A. Erb, J. Demsar, R. Huber, and A. Leitenstorfer. Femtosecond response of quasiparticles and phonons in superconducting $YBa_2Cu_3O_{7-\delta}$ studied by wideband terahertz spectroscopy. *Physical Review Letters*, 105(6):067001, Aug. 2010. doi: 10.1103/PhysRevLett.105.067001. URL http://link.aps.org/doi/10.1103/PhysRevLett.105.067001.

[Perfetti et al., 2006] L. Perfetti, P. A. Loukakos, M. Lisowski, U. Bovensiepen, H. Berger, S. Biermann, P. S. Cornaglia, A. Georges, and M. Wolf. Time Evolution of the Electronic Structure of $1T$-TaS_2 through the Insulator-Metal Transition. *Physical Review Letters*, 97(6):067402, Aug. 2006. doi: 10.1103/PhysRevLett.97.067402. URL http://link.aps.org/doi/10.1103/PhysRevLett.97.067402.

[Perfetti et al., 2007] L. Perfetti, P. A. Loukakos, M. Lisowski, U. Bovensiepen, H. Eisaki, and M. Wolf. Ultrafast electron relaxation in superconducting $Bi_2Sr_2CaCu_2O_{8+\delta}$ by Time-Resolved photoelectron Spectroscopy. *Physical Review Letters*, 99(19):197001, Nov. 2007. doi: 10.1103/PhysRevLett.99.197001. URL http://link.aps.org/doi/10.1103/PhysRevLett.99.197001.

[Perfetti et al., 2008] L. Perfetti, P. A. Loukakos, M. Lisowski, U. Bovensiepen, M. Wolf, H. Berger, S. Biermann, and A. Georges. Femtosecond dynamics of electronic states in the Mott insulator 1T-TaS_2 by time resolved photoelectron spectroscopy. *New Journal of Physics*, 10(5):053019, May 2008. ISSN 1367-2630. doi: 10.1088/1367-2630/10/5/053019. URL http://iopscience.iop.org/1367-2630/10/5/053019.

[Pines, 1997] D. Pines. Nearly antiferromagnetic fermi liquids: a progress report. *Zeitschrift für Physik B Condensed Matter*, 103(2):129–135, Feb. 1997. ISSN 0722-3277, 1431-584X. doi: 10.1007/s002570050346. URL http://link.springer.com/article/10.1007/s002570050346.

[Pintschovius and Braden, 1999] L. Pintschovius and M. Braden. Anomalous dispersion of LO phonons in $La_{1.85}Sr_{0.15}CuO_4$. *Physical Review B*, 60(22):R15039–R15042, Dec. 1999. doi: 10.1103/PhysRevB.60.R15039. URL http://link.aps.org/doi/10.1103/PhysRevB.60.R15039.

[Poole Jr et al., 2007] C. P. Poole Jr, H. A. Farach, R. J. Creswick, and R. Prozorov. *Superconductivity, Second Edition*. Academic Press, Amsterdam, 2 edition edition, Aug. 2007. ISBN 9780120887613.

[Qin et al., 2010] H. Qin, J. Shi, Y. Cao, K. Wu, J. Zhang, E. W. Plummer, J. Wen, Z. J. Xu, G. D. Gu, and J. Guo. Direct Determination of the Electron-Phonon Coupling Matrix Element in a Correlated System. *Physical Review Letters*, 105(25):256402, Dec. 2010. doi: 10.1103/PhysRevLett.105.256402. URL http://link.aps.org/doi/10.1103/PhysRevLett.105.256402.

[Reedyk and Timusk, 1992] M. Reedyk and T. Timusk. Evidence for a-b-plane coupling to longitudinal c-axis phonons in high-T_c superconductors. *Physical Review Letters*, 69(18):2705–

2708, Nov. 1992. doi: 10.1103/PhysRevLett.69.2705. URL http://link.aps.org/doi/10.1103/PhysRevLett.69.2705.

[Reynolds et al., 1950] C. A. Reynolds, B. Serin, W. H. Wright, and L. B. Nesbitt. Superconductivity of Isotopes of Mercury. *Physical Review*, 78(4):487–487, May 1950. doi: 10.1103/PhysRev.78.487. URL http://link.aps.org/doi/10.1103/PhysRev.78.487.

[Riffe and Sabbah, 2007] D. M. Riffe and A. J. Sabbah. Coherent excitation of the optic phonon in Si: Transiently stimulated Raman scattering with a finite-lifetime electronic excitation. *Physical Review B*, 76(8):085207, Aug. 2007. doi: 10.1103/PhysRevB.76.085207. URL http://link.aps.org/doi/10.1103/PhysRevB.76.085207.

[Roeser et al., 2003] C. a. D. Roeser, A. M.-T. Kim, J. P. Callan, L. Huang, E. N. Glezer, Y. Siegal, and E. Mazur. Femtosecond time-resolved dielectric function measurements by dual-angle reflectometry. *Review of Scientific Instruments*, 74(7):3413–3422, July 2003. ISSN 0034-6748, 1089-7623. doi: 10.1063/1.1582383. URL http://scitation.aip.org/content/aip/journal/rsi/74/7/10.1063/1.1582383.

[Röhler, 1996] J. Röhler. On the stereochemistry of cations in the doping block of superconducting copper oxides. *Journal of Superconductivity*, 9(4):457–461, Aug. 1996. ISSN 0896-1107, 1572-9605. doi: 10.1007/BF00727296. URL http://link.springer.com/article/10.1007/BF00727296.

[Rossnagel, 2011] K. Rossnagel. On the origin of charge-density waves in select layered transition-metal dichalcogenides. *Journal of Physics: Condensed Matter*, 23(21):213001, June 2011. ISSN 0953-8984. doi: 10.1088/0953-8984/23/21/213001. URL http://iopscience.iop.org/0953-8984/23/21/213001.

[Rossnagel and Smith, 2006] K. Rossnagel and N. V. Smith. Spin-orbit coupling in the band structure of reconstructed $1T$-TaS$_2$. *Physical Review B*, 73(7):073106, Feb. 2006. doi: 10.1103/PhysRevB.73.073106. URL http://link.aps.org/doi/10.1103/PhysRevB.73.073106.

[Rübhausen et al., 2001] M. Rübhausen, A. Gozar, M. Klein, P. Guptasarma, and D. Hinks. Superconductivity-induced optical changes for energies of 100 Δ in the cuprates. *Physical Review B*, 63(22):224514, 2001.

[Sai-Halasz and Perry, 1977] G. A. Sai-Halasz and P. B. Perry. Charge density waves effects on the phonon modes of 1T-TaS$_2$. *Solid State Communications*, 21(11):995–997, Mar. 1977. ISSN 0038-1098. doi: 10.1016/0038-1098(77)90003-5. URL http://www.sciencedirect.com/science/article/pii/0038109877900035.

[Saichu et al., 2009] R. P. Saichu, I. Mahns, A. Goos, S. Binder, P. May, S. G. Singer, B. Schulz, A. Rusydi, J. Unterhinninghofen, D. Manske, P. Guptasarma, M. S. Williamsen, and M. Rübhausen. Two-Component Dynamics of the Order Parameter of High Temperature Bi$_2$Sr$_2$CaCu$_2$O$_{8+\delta}$ Superconductors Revealed by Time-Resolved Raman Scattering. *Physical Review Letters*, 102(17):177004, Apr. 2009. doi: 10.1103/PhysRevLett.102.177004. URL http://link.aps.org/doi/10.1103/PhysRevLett.102.177004.

[Scalapino, 1995] D. J. Scalapino. The case for d$_{x^2-y^2}$ pairing in the cuprate superconductors. *Physics Reports*, 250(6):329–365, Jan. 1995. ISSN 0370-1573. doi: 10.1016/0370-1573(94)00086-I. URL http://www.sciencedirect.com/science/article/pii/037015739400086I.

[Schlachter et al., 2000] S. I. Schlachter, U. Tutsch, W. H. Fietz, K.-P. Weiss, H. Leibrock, K. Grube, T. Wolf, B. Obst, P. Schweiss, and H. Wühl. Pressure Effect and Specific Heat of RBa$_2$Cu$_3$O$_x$ at Distinct Charge Carrier Concentrations: Possible Influence of Stripes. *International Journal of Modern Physics B*, 14(29n31):3673–3678, Dec. 2000. ISSN 0217-9792. doi: 10.1142/S0217979200004209. URL http://www.worldscientific.com/doi/abs/10.1142/S0217979200004209.

[Schumann, 2009] O. J. Schumann. *Clip User Manual*, March 2009. URL http://clip4.sourceforge.net/.

[Sipos et al., 2008] B. Sipos, A. F. Kusmartseva, A. Akrap, H. Berger, L. Forrò, and E. Tutiš. From Mott state to superconductivity in 1T-TaS$_2$. *Nature Materials*, 7(12):960–965, Dec. 2008. ISSN 1476-1122. doi: 10.1038/nmat2318. URL http://www.nature.com/nmat/journal/v7/n12/full/nmat2318.html.

[Slichter, 1996] C. P. Slichter. *Principles of Magnetic Resonance*. Springer Science & Business Media, Mar. 1996. ISBN 9783540501572.

[Smith et al., 1985] N. V. Smith, S. D. Kevan, and F. J. DiSalvo. Band structures of the layer compounds 1T-TaS$_2$ and 2H-TaSe$_2$ in the presence of commensurate charge-density waves. *Journal of Physics C: Solid State Physics*, 18(16):3175, June 1985. ISSN 0022-3719. doi: 10.1088/0022-3719/18/16/013. URL http://iopscience.iop.org/0022-3719/18/16/013.

[Spalek, 2007] J. Spalek. t-J model then and now: A personal perspective from the pioneering times. *arXiv:0706.4236 [cond-mat]*, June 2007. URL http://arxiv.org/abs/0706.4236. arXiv: 0706.4236.

[Spijkerman et al., 1997] A. Spijkerman, J. L. de Boer, A. Meetsma, G. A. Wiegers, and S. van Smaalen. X-ray crystal-structure refinement of the nearly commensurate phase of 1T-TaS$_2$ in (3+2)-dimensional superspace. *Physical Review B*, 56(21):13757–13767, Dec. 1997. doi: 10.1103/PhysRevB.56.13757. URL http://link.aps.org/doi/10.1103/PhysRevB.56.13757.

[Spitaler et al., 2013] J. Spitaler, E. I. Shneyder, E. E. Kokorina, I. A. Nekrasov, V. A. Gavrichkov, C. Ambrosch-Draxl, and S. G. Ovchinnikov. Density Functional Theory and Generalized Tight-Binding combined method for Hubbard fermion-phonon coupling study in strongly correlated LSCO-system. *arXiv:1310.6872 [cond-mat]*, Oct. 2013. URL http://arxiv.org/abs/1310.6872. arXiv: 1310.6872.

[Stanescu and Phillips, 2003] T. D. Stanescu and P. Phillips. Pseudogap in doped Mott insulators is the near-neighbor analogue of the Mott gap. *Physical Review Letters*, 91(1):017002, 2003.

Bibliography

[Stevens et al., 1997] C. Stevens, D. Smith, C. Chen, J. Ryan, B. Podobnik, D. Mihailovic, G. Wagner, and J. Evetts. Evidence for Two-Component High-Temperature Superconductivity in the Femtosecond Optical Response of $YBa_2Cu_3O_{7-\delta}$. *Physical Review Letters*, 78(11):2212, 1997.

[Stevens et al., 2002] T. E. Stevens, J. Kuhl, and R. Merlin. Coherent phonon generation and the two stimulated Raman tensors. *Physical Review B*, 65(14):144304, Mar. 2002. doi: 10.1103/ PhysRevB.65.144304. URL http://link.aps.org/doi/10.1103/PhysRevB.65.144304.

[Stojchevska et al., 2011] L. Stojchevska, P. Kusar, T. Mertelj, V. V. Kabanov, Y. Toda, X. Yao, and D. Mihailovic. Mechanisms of nonthermal destruction of the superconducting state and melting of the charge-density-wave state by femtosecond laser pulses. *Physical Review B*, 84 (18):180507, Nov. 2011. doi: 10.1103/PhysRevB.84.180507. URL http://link.aps.org/doi/10. 1103/PhysRevB.84.180507.

[Stojchevska et al., 2014] L. Stojchevska, I. Vaskivskyi, T. Mertelj, P. Kusar, D. Svetin, S. Brazovskii, and D. Mihailovic. Ultrafast Switching to a Stable Hidden Quantum State in an Electronic Crystal. *Science*, 344(6180):177–180, Nov. 2014. ISSN 0036-8075, 1095-9203. doi: 10.1126/ science.1241591. URL http://www.sciencemag.org/content/344/6180/177.

[Sugai, 1989] S. Sugai. Phonon raman scattering in $(La_{1-x}Sr_x)_2CuO_4$ single crystals. *Physical Review B*, 39(7):4306–4315, Mar. 1989. doi: 10.1103/PhysRevB.39.4306. URL http://link.aps.org/ doi/10.1103/PhysRevB.39.4306.

[Sugai et al., 1981] S. Sugai, K. Murase, S. Uchida, and S. Tanaka. Comparison of the soft modes in tantalum dichalcogenides. *Physica B+C*, 105(1–3):405–409, May 1981. ISSN 0378-4363. doi: 10.1016/0378-4363(81)90284-9. URL http://www.sciencedirect.com/science/article/pii/ 0378436381902849.

[Sugai et al., 2003] S. Sugai, H. Suzuki, Y. Takayanagi, T. Hosokawa, and N. Hayamizu. Carrier-density-dependent momentum shift of the coherent peak and the LO phonon mode in p-type high-T_c superconductors. *Physical Review B*, 68(18):184504, Nov. 2003. doi: 10.1103/ PhysRevB.68.184504. URL http://link.aps.org/doi/10.1103/PhysRevB.68.184504.

[Sugai et al., 2013] S. Sugai, Y. Takayanagi, N. Hayamizu, T. Muroi, R. Shiozaki, J. Nohara, K. Takenaka, and K. Okazaki. Superconducting pairing and the pseudogap in the nematic dynamical stripe phase of La_2CuO_4. *Journal of Physics: Condensed Matter*, 25(47):475701, Nov. 2013. ISSN 0953-8984. doi: 10.1088/0953-8984/25/47/475701. URL http://iopscience.iop.org/ 0953-8984/25/47/475701.

[Thomas et al., 1996] T. Thomas, C. Stevens, A. Choudhary, J. Ryan, D. Mihailovic, T. Mertelj, L. Forro, G. Wagner, and J. Evetts. Photoexcited carrier relaxation and localization in $Bi_2Sr_2Ca_{1-y}Y_yCu_2O_8$ and $YBa_2Cu_3O_{7-\delta}$: A study by femtosecond time-resolved spectroscopy. *Physical Review B*, 53(18):12436, 1996.

[Thompson et al., 1971] A. H. Thompson, R. F. Gamble, and J. F. Revelli. Transitions between semiconducting and metallic phases in $1T$-TaS_2. *Solid State Communications*, 9(13):

981–985, July 1971. ISSN 0038-1098. doi: 10.1016/0038-1098(71)90444-3. URL http://www.sciencedirect.com/science/article/pii/0038109871904443.

[Thomson et al., 1994] R. E. Thomson, B. Burk, A. Zettl, and J. Clarke. Scanning tunneling microscopy of the charge-density-wave structure in $1T$-TaS$_2$. *Physical Review B*, 49(24):16899–16916, June 1994. doi: 10.1103/PhysRevB.49.16899. URL http://link.aps.org/doi/10.1103/PhysRevB.49.16899.

[Toda et al., 2004] Y. Toda, K. Tateishi, and S. Tanda. Anomalous coherent phonon oscillations in the commensurate phase of the quasi-two-dimensional $1T$-TaS$_2$ compound. *Physical Review B*, 70(3):033106, July 2004. doi: 10.1103/PhysRevB.70.033106. URL http://link.aps.org/doi/10.1103/PhysRevB.70.033106.

[Torchinsky et al., 2013] D. H. Torchinsky, F. Mahmood, A. T. Bollinger, I. Božović, and N. Gedik. Fluctuating charge-density waves in a cuprate superconductor. *Nature materials*, 12(5): 387–391, 2013.

[Trefethen and Bau, 1997] L. N. Trefethen and D. Bau. *Numerical Linear Algebra*. Society for Industrial and Applied Mathematics, 1997. ISBN 9780898713619.

[Uchida and Sugai, 1981] S. Uchida and S. Sugai. Infrared and Raman studies on commensurate CDW states in transition metal dichalcogenides. *Physica B+C*, 105(1–3):393–399, May 1981. ISSN 0378-4363. doi: 10.1016/0378-4363(81)90282-5. URL http://www.sciencedirect.com/science/article/pii/0378436381902825.

[Uchida et al., 1991] S. Uchida, T. Ido, H. Takagi, T. Arima, Y. Tokura, and S. Tajima. Optical spectra of La$_{2-x}$Sr$_x$CuO$_4$: Effect of carrier doping on the electronic structure of the CuO$_2$ plane. *Physical Review B*, 43(10):7942–7954, Apr. 1991. doi: 10.1103/PhysRevB.43.7942. URL http://link.aps.org/doi/10.1103/PhysRevB.43.7942.

[van den Brink and Sawatzky, 2000] J. van den Brink and G. A. Sawatzky. Non-conventional screening of the Coulomb interaction in low-dimensional and finite-size systems. *EPL (Europhysics Letters)*, 50(4):447, May 2000. ISSN 0295-5075. doi: 10.1209/epl/i2000-00290-6. URL http://iopscience.iop.org/0295-5075/50/4/447.

[van den Brink et al., 1995] J. van den Brink, M. B. J. Meinders, J. Lorenzana, R. Eder, and G. A. Sawatzky. New Phases in an Extended Hubbard Model Explicitly Including Atomic Polarizabilities. *Physical Review Letters*, 75(25):4658–4661, Dec. 1995. doi: 10.1103/PhysRevLett.75.4658. URL http://link.aps.org/doi/10.1103/PhysRevLett.75.4658.

[van der Marel, 2004] D. van der Marel. Optical spectroscopy of plasmons and excitons in cuprate superconductors. *arXiv:cond-mat/0410473*, Oct. 2004. URL http://arxiv.org/abs/cond-mat/0410473.

[Varma, 2010] C. Varma. High-temperature superconductivity: Mind the pseudogap. *Nature*, 468 (7321):184–185, Nov. 2010. ISSN 0028-0836. doi: 10.1038/468184a. URL http://www.nature.com/nature/journal/v468/n7321/full/468184a.html.

[Varma, 2001] C. M. Varma. Higgs boson in superconductors. *arXiv:cond-mat/0109409*, Sept. 2001. URL http://arxiv.org/abs/cond-mat/0109409.

[Vershinin et al., 2004] M. Vershinin, S. Misra, S. Ono, Y. Abe, Y. Ando, and A. Yazdani. Local ordering in the pseudogap state of the high-T_c superconductor $Bi_2Sr_2CaCu_2O_{8+\delta}$. *Science*, 303(5666): 1995–1998, 2004.

[Warner and Leggett, 2005] G. L. Warner and A. J. Leggett. Quench dynamics of a superfluid fermi gas. *Physical Review B*, 71(13):134514, Apr. 2005. doi: 10.1103/PhysRevB.71.134514. URL http://link.aps.org/doi/10.1103/PhysRevB.71.134514.

[Wu et al., 1987] M. K. Wu, J. R. Ashburn, C. J. Torng, P. H. Hor, R. L. Meng, L. Gao, Z. J. Huang, Y. Q. Wang, and C. W. Chu. Superconductivity at 93 K in a new mixed-phase Y-Ba-Cu-O compound system at ambient pressure. *Physical Review Letters*, 58(9):908–910, Mar. 1987. doi: 10.1103/PhysRevLett.58.908. URL http://link.aps.org/doi/10.1103/PhysRevLett.58.908.

[Yang et al., 2008] H.-B. Yang, J. Rameau, P. Johnson, T. Valla, A. Tsvelik, and G. Gu. Emergence of preformed Cooper pairs from the doped Mott insulating state in $Bi_2Sr_2CaCu_2O_{8+\delta}$. *Nature*, 456(7218):77–80, 2008.

[Yoshida et al., 2006] T. Yoshida, X. J. Zhou, K. Tanaka, W. L. Yang, Z. Hussain, Z.-X. Shen, A. Fujimori, S. Sahrakorpi, M. Lindroos, R. S. Markiewicz, A. Bansil, S. Komiya, Y. Ando, H. Eisaki, T. Kakeshita, and S. Uchida. Systematic doping evolution of the underlying fermi surface of $La_{2-x}Sr_xCuO_4$. *Physical Review B*, 74(22):224510, Dec. 2006. doi: 10.1103/PhysRevB.74.224510. URL http://link.aps.org/doi/10.1103/PhysRevB.74.224510.

[Yu et al., 1993] G. Yu, C. Lee, D. Mihailovic, A. Heeger, C. Fincher, N. Herron, and E. McCarron. Photoconductivity in insulating $YBa_2Cu_3O_{6+x}$: From Mott-Hubbard insulator to Fermi glass via oxygen doping. *Physical Review B*, 48(10):7545, 1993.

[Yu et al., 2008] L. Yu, D. Munzar, A. Boris, P. Yordanov, J. Chaloupka, T. Wolf, C. Lin, B. Keimer, and C. Bernhard. Evidence for two separate energy gaps in underdoped high-temperature cuprate superconductors from broadband infrared ellipsometry. *Physical Review Letters*, 100(17):177004, 2008.

[Yusupov et al., 2010] R. Yusupov, T. Mertelj, V. V. Kabanov, S. Brazovskii, P. Kusar, J.-H. Chu, I. R. Fisher, and D. Mihailovic. Coherent dynamics of macroscopic electronic order through a symmetry breaking transition. *Nature Physics*, 6(9):681–684, Sept. 2010. ISSN 1745-2473. doi: 10.1038/nphys1738. URL http://www.nature.com/nphys/journal/v6/n9/full/nphys1738.html.

[Zaanen, 2011] J. Zaanen. A modern, but way too short history of the theory of superconductivity at a high temperature. In H. Rogalla and P. H. Kes, editors, *100 Years of Superconductivity*. Taylor & Francis, Nov. 2011. ISBN 9781439849484.

[Zaanen and Sawatzky, 1987] J. Zaanen and G. A. Sawatzky. The electronic structure and superexchange interactions in transition-metal compounds. *Canadian Journal of Physics*, 65

(10):1262–1271, Oct. 1987. ISSN 0008-4204. doi: 10.1139/p87-201. URL http://www. nrcresearchpress.com/doi/abs/10.1139/p87-201.

[Zaanen et al., 1985] J. Zaanen, G. A. Sawatzky, and J. W. Allen. Band gaps and electronic structure of transition-metal compounds. *Physical Review Letters*, 55(4):418–421, July 1985. doi: 10.1103/PhysRevLett.55.418. URL http://link.aps.org/doi/10.1103/PhysRevLett.55.418.

[Zaanen et al., 1986] J. Zaanen, G. A. Sawatzky, and J. W. Allen. The electronic structure and band gaps in transition metal compounds. *Journal of Magnetism and Magnetic Materials*, 54–57, Part 2:607–611, Feb. 1986. ISSN 0304-8853. doi: 10.1016/0304-8853(86)90188-5. URL http://www.sciencedirect.com/science/article/pii/0304885386901885.

[Zeiger et al., 1992] H. J. Zeiger, J. Vidal, T. K. Cheng, E. P. Ippen, G. Dresselhaus, and M. S. Dresselhaus. Theory for displacive excitation of coherent phonons. *Physical Review B*, 45(2): 768–778, Jan. 1992. doi: 10.1103/PhysRevB.45.768. URL http://link.aps.org/doi/10.1103/PhysRevB.45.768.

Acknowledgements

Doing a PhD in experimental physics is a labor of love, setting up and performing experiments, figuring out minute details and intrinsic (mis-)behavior of the experiments, and managing all kinds of disasters. Between fires, floodings and blackouts, it has been an interesting struggle, and this work would not have been possible without the many people supporting me in the endeavor. I want to express my thanks towards all of them, even if I prefer to keep this chapter brief and not list every single person by name. First off, the biggest thank you goes to **Fabrizio**, for "adopting" me into his group and supporting me all the way in my work as well as helping me through the "existential crises" that I had after staring at my data for too long. I learned a great deal from you, even if playing the mandolin still is not part of my repertoire. The person that I bugged the second most, after Fabrizio, is certainly Prof. **José Lorenzana** who, along with his student Antonio, kept an open ear and mustered a lot of patience in my struggle to grasp the theory behind what I have been doing. Furthermore, I would like to thank José as well as Prof. **Steven Johnson** and Prof. **Dirk van der Marel** for volunteering as members of my thesis committee. Next, I want to thank all the past and present members of the **LUMES** and **LSU** groups for the many good moments we shared. I enjoyed the time I spent with you, working or otherwise. I have to thank my dear Italian colleagues for putting up with the strange person from the far side of the Alps, and my other colleagues for teaching me how to survive without speaking a word of Italian. While many people helped me out in different ways, I would like to give special thanks to Dr. **Ahmad Odeh** and **Edoardo Baldini**, with whom I spent most of the time in the lab. Finally, I want to add that living in Switzerland has been an interesting experience, and I would like to thank **my family** for supporting me during this time and for enduring my exile here.

Lausanne, 15th June 2015   Andreas Mann

Curriculum Vitae

Personal data:
Andreas Helmut Christian MANN, born in Göttingen (Germany), on the 9th of May 1984.

Contact address:
andreas.mann@epfl.ch

Fields of interest:
correlated electron systems, high-TC superconductivity, ultrafast spectroscopy, ultrafast magnetization dynamics

Skills and experience:
Experimental:
pump-probe techniques, laser operation and maintenance, optics, sample preparation, vacuum and cryogenic equipment
Theoretical:
solid state physics, esp. superconductivity, magnetism and correlated systems, data analysis and modeling

Education:
March 2010: Diploma in Physics at the Georg August University of Göttingen. Thesis title: "Determining the Spin Polarization of Heusler Compounds via Femtosecond Magnetization Dynamics" Current Employment: PhD student in the group of Prof. Fabrizio Carbone at the École Polytechnique fédérale de Lausanne (EPFL) in Lausanne, Switzerland, since June 2010

Oral presentations:
numerous presentations and talks at international conferences, including the V. Int. Symp. on Strong Nonlinear Vibronic and Electronic Interactions in Solids 2015, SuperFox/TOBE 2014, ICSM 2014, EUCAS 2013, SPS 2011, ICM 2009.

Teaching experience:
long-time undergraduate instructor, experience in giving full lectures

Language Skills:
German (native), English (fluent), French (intermediate)

List of Publications

as of August 2015

- **A. Mann**, E. Baldini, A. Tramontana, E. Pomjakushina, K. Conder, C. Arrell, D. van der Marel, J. Lorenzana, and F. Carbone. "Probing the electron-phonon interaction in correlated systems with coherent lattice fluctuation spectroscopy". *Phys. Rev. B **92**(3), 035147 (2015)*. DOI: 10.1103/PhysRevB.92.035147.

- E. Baldini, **A. Mann**, B. P. P. Mallett, C. Arrell, F. Van Mourik, Th. Wolf, C. Bernhard, J. L. Tallon, J. Lorenzana, and F. Carbone. "Evidence for pre-formed cooper pairs in the pseudogap phase of slightly underdoped $NdBa_2Cu_3O_{7-\delta}$". *In preparation.*

- S. Borroni, **A. Mann**, E. Baldini, C. Arrell, F. van Mourik, and F. Carbone. "On the Verwey transition in magnetite: the soft modes of the Metal-Insulator transition". *Submitted.*

- L. Piazza, C. Ma, H. X. Yang, **A. Mann**, Y. Zhu, J. Q. Li and F. Carbone. "Ultrafast structural and electronic dynamics of the metallic phase in a layered manganite". *Struct. Dyn. **1**, 014501 (2014)*. DOI: 10.1063/1.4835116.

- J. Lorenzana, B. Mansart, **A. Mann**, A. Odeh, M. Chergui, F. Carbone. "Investigating pairing interactions with coherent charge fluctuation spectroscopy". *Eur. Phys. J. Spec. Top. Vol **222**, 5 (2013)*. DOI: 10.1140/epjst/e2013-01917-9.

- B. Mansart, J. Lorenzana, **A. Mann**, A. Odeh, M. Scarongella, M. Chergui, and F. Carbone. "Coupling of a high-energy excitation to superconducting quasiparticles in a cuprate from coherent charge fluctuation spectroscopy". *Proc. Nat. Acad. Sci. **110**, 12 (2013)*. DOI: 10.1073/pnas.1218742110.

- **A. Mann**, J. Walowski, M. Münzenberg, S. Maat, M. J. Carey, J. R. Childress, C. Mewes, D. Ebke, V. Drewello, G. Reiss, and A. Thomas. "Insights into ultrafast demagnetization in pseudogap half-metals". *Phys. Rev. X **2**, 041008 (2012)*. DOI: 10.1103/PhysRevX.2.041008.

- U. Atxitia, O. Chubykalo-Fesenko, J. Walowski, **A. Mann**, and M. Münzenberg. "Evidence for thermal mechanisms in laser-induced femtosecond spin dynamics". *Phys. Rev. B **81**, 174401*. DOI: 10.1103/PhysRevB.81.174401

- **A. Mann**. "Determining the Spin Polarization of Heusler Compounds via Femtosecond Magnetization Dynamics". *Diploma thesis*, University of Göttingen, 2010.